

Heavy-Element Fission Barriers*

Peter Möller^{1,†}, Arnold J. Sierk¹, Takatoshi Ichikawa², AkiraIwamoto³, Ragnar Bengtsson⁴, Henrik Uhrenholt⁴, and Sven Åberg⁴¹*Theoretical Division, Los Alamos National Laboratory, Los Alamos, New Mexico 87545, USA*²*RIKEN Nishina Center, RIKEN, Wako, Saitama 351-0198, Japan*³*Advanced Science Research Center, Japan Atomic Energy Agency (JAEA), Tokai-mura, Naka-gun, Ibaraki, 319-1195, Japan*⁴*Department of Mathematical Physics, Lund Institute of Technology, Box 118, SE - 22100 Lund, Sweden*

(Dated: Revised March 3, 2009)

We present calculations of fission properties for heavy elements. The calculations are based on the macroscopic-microscopic finite-range liquid-drop model with a 2002 parameter set. For each nucleus we have calculated the potential energy in 3 different shape parametrizations: (1) for 5009325 different shapes in a five-dimensional deformation space given by the three-quadratic-surface parametrization, (2) for 10850 different shapes in a three-dimensional deformation space spanned by ϵ_2 , ϵ_4 and γ in the Nilsson perturbed-spheroid parametrization, supplemented by a densely spaced grid in ϵ_2 , ϵ_3 , ϵ_4 , and ϵ_6 for axially symmetric deformations in the neighborhood of the ground state, and (3) an axially symmetric multipole expansion of the shape of the nuclear surface using β_2 , β_3 , β_4 , and β_6 for intermediate deformations. For a fissioning system it is always possible to define uniquely *one* saddle or fission threshold on the optimum trajectory between the ground state and separated fission fragments. We present such calculated barrier heights for 1585 nuclei from $Z = 78$ to $Z = 125$. Traditionally actinide barriers have been characterized in terms of a “double-humped” structure. Following this custom we present calculated energies of the first peak, second minimum, and second peak in the barrier for 135 actinide nuclei from Th to Es. However, for some of these nuclei which exhibit a more complex barrier structure there is no unique way to extract a double-humped structure from the calculations. We give examples of such more complex structures, in particular the structure of the outer barrier region near ^{232}Th and the occurrence of multiple fission modes. Because our complete results are too extensive to present in a paper of this type our aim here is limited: (1) to fully present our model and the methods for determining the structure of the potential-energy surface, (2) to present fission thresholds for a large number of heavy elements, (3) to compare our results with the two-humped barrier structure deduced from experiment for actinide nuclei, and (4) to compare to additional fission-related data and to other fission models.

PACS numbers: 21.10.-k, 21.10.Dr, 21.10.Hw, 21.10.Re, 21.60-n

Contents

I. INTRODUCTION	2	D. Alternative immersion strategies	14
II. MODELS	4	E. Additional saddle points	15
A. Shape parametrizations	4	F. Identifying the ground state	15
1. Nilsson perturbed spheroids	4	IV. DETAILED BARRIER STRUCTURE	16
2. Multipole expansion	5	V. FISSION-BARRIER HEIGHTS	22
3. Three quadratic surfaces	5	VI. SHAPES AND LEVEL DENSITIES	30
B. Potential energy	8	VII. COMPARISONS TO DATA AND OTHER MODELS	32
C. Level densities	9	A. Fission-barrier heights	32
III. ANALYSIS	10	B. Other models	34
A. Fallacies in finding saddle points	10	C. Heavy-element stability	37
B. Immersion method	12	D. EC-delayed fission	39
C. Computer model of immersion	13	E. Bimodal fission	40
		Acknowledgments	41
		VIII. APPENDIX	42
		References	43

*This paper is dedicated to the memory of our friend and colleague Ray Nix, who through his years of devoted research on nuclear fission, for example on the topics of the three-quadratic-surface parametrization, the folded-Yukawa single-particle model, the finite-range surface energy, and fission inertias, made possible many of the calculations discussed here.

[†]Electronic address: moller@lanl.gov

I. INTRODUCTION

In fission a nucleus evolves from a single ground-state shape to separated fission fragments. A key question is, what are the optimum trajectories and the associated shapes and energies along these trajectories? In particular, what is the maximum energy along the optimum trajectory (barrier height), what are the symmetries of the nucleus at this saddle point, and what is the level density at the saddle? The saddle-point energy will tell us if thermal-neutron-induced fission is energetically possible. The balance between the neutron separation energy and fission-barrier height is decisive for determining the behavior of different actinide isotopes in a nuclear reactor and the nature of the termination of element synthesis in the r-process. The heaviest nucleus that can be formed in the r-process is determined by where the onset of neutron-induced fission occurs. As another example, if the Q-value for electron capture (EC) is sufficiently large to allow states above or just below the fission barrier in the daughter to be populated, then electron-capture-delayed fission is possible.

Since the discovery of fission, it has been customary to begin the characterization of the process by calculating the potential energy of a nucleus as a function of shape. Soon after the discovery of fission in 1938 the potential energy was described in terms of a liquid-drop model in which the potential energy is the sum of shape-dependent surface and Coulomb energy terms. This description was first invoked by Meitner and Frisch [1] but soon put on a more quantitative basis in the seminal paper by Bohr and Wheeler [2].

Several subsequent developments led to the much more complete theoretical picture of the fission potential energy that exists today, as is schematically illustrated in Fig. 1. In the first model of the fission barrier, the liquid-drop model, Bohr and Wheeler [2] expanded the Coulomb and surface energies to fourth order in α_2 , the lowest-order coefficient in an expansion of the reflection and axially symmetric shape in Legendre polynomials. With this approximation, they could determine barrier heights and corresponding deformations for very heavy nuclei. By clever formulations they were also able to deduce the barriers of light nuclei and by interpolation span the region in between, thus obtaining estimates of fission barriers throughout the periodic system. In an important 1947 paper which foreshadowed many of the developments to emerge more than a decade later, Frankel and Metropolis [3] calculated the Coulomb and surface energies of more highly deformed nuclear shapes using numerical integration. This was one of the first basic-physics calculations done on a digital computer. For more than a decade afterwards, developments reverted to attempting to model the macroscopic energies by more complicated expansions in deformation parameters, which was never completely satisfactory due to convergence difficulties. When numerical calculations were resumed in earnest about 1960, major progress in understanding the

liquid-drop model rapidly followed. In a parallel development, in 1955 Swiatecki [4] suggested that more realistic fission barriers could be obtained by adding a “correction energy” to the minimum in the liquid-drop-model barrier. The correction was calculated as the difference between the experimentally observed nuclear ground-state mass and the mass given by the liquid-drop model. Swiatecki obtained much improved theoretical spontaneous-fission half-lives based on these modified liquid-drop-model barriers. These observations formed the basis for the shell-correction method. In the mid 1960’s Strutinsky [5, 6] presented a method to theoretically *calculate* these shell corrections. His method and parallel experimental results led to the realization that actinide fission barriers are “double-humped”: beyond the ground-state minimum there are two saddles or maxima in the fission barrier, separated by a fission-isomeric second minimum. Later, Nix [7] proposed that certain experimental data could best be explained if the outer barrier peak were split into two peaks separated by a shallow “third” minimum. In these early studies the fission potential energy was usually calculated only for a few hundred nuclear shapes. However, to obtain a realistic picture of the potential energy it is necessary to calculate the energy for several million different shapes and use special techniques for identifying relevant saddle points on the paths from the nuclear ground state to the separated fission fragments. We have explored some of the consequences of this approach in a series of papers [8–12].

The complete specification of our macroscopic-microscopic model of potential energy for a given shape has been given elsewhere [13]. Some references in [13] that give additional background information are [14–22]. Here we limit the presentation to the specific details on how we apply the model in the current calculations. Since many issues related to determining fission saddle points appear to be poorly understood, we discuss these crucial issues in some detail. In particular there is a belief that the Hartree-Fock method automatically takes all higher shape degrees of freedom into account and that this means that saddle points are well determined in this method. This was first stated in 1973 [23] and repeated in 1980 in a commonly used textbook [24], in which it is also stated that one-constraint calculations are superior to macroscopic-microscopic Strutinsky calculations which must calculate multidimensional surfaces. This is false. Deficiencies that are similar to those of constrained Hartree-Fock calculations, but not identical, are present in macroscopic-microscopic calculations that display results versus two variables, say β_2 and β_3 and minimize the energy with respect to additional multipoles rather than calculate the complete deformation space in all the variables considered. We show by specific examples that even in HFB calculations with multiple constraints, saddle-point shapes and energies frequently cannot be determined accurately and are subject to errors of fairly random magnitude. In brief, the source of the errors is that the unconstrained shape variables vary in an uncontrolled

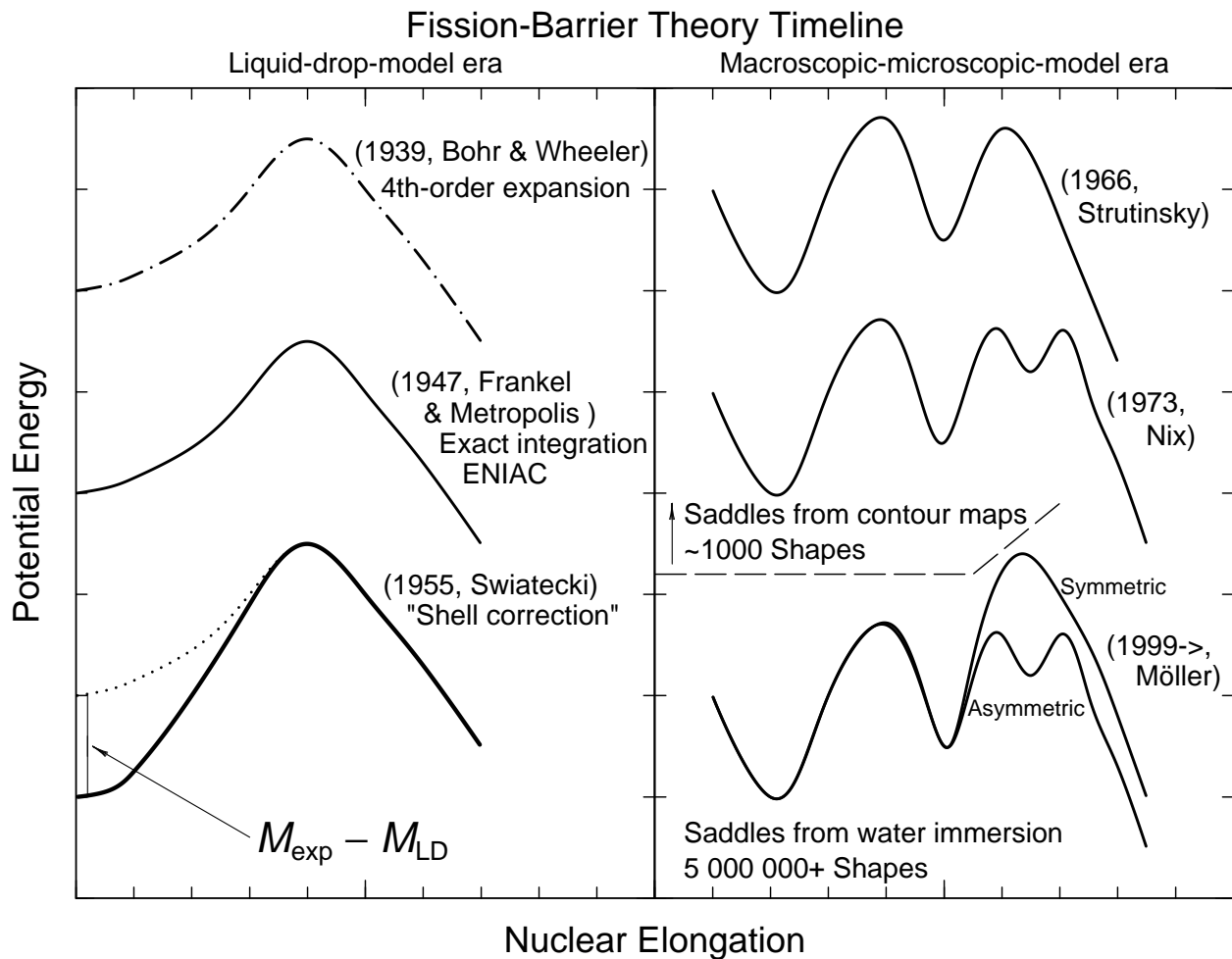


FIG. 1: Historical development of fission-barrier theory. For details, see the text.

fashion and may assume values that lead the method to converge to saddle points that lie high up on a mountain side, rather than to the optimum saddle between the ground state and separated fragments. In contrast, shape variables in our method are completely specified and are therefore totally controlled. Rather than being a weakness of our method, it is a significant strength. We provide details in Sects. II and III.

We use previously developed techniques to perform a systematic calculation of fission potential-energy surfaces for 5254 nuclei from $A = 171$ to $A = 330$ from the proton drip line to the neutron drip line in three different deformation spaces for each nucleus. We calculate potential energies in a 5-dimensional space for 5009325 different shapes, in a 3-dimensional space that includes axial asymmetry for 10850 different shapes, and in a constrained β parametrization; details are given below.

We also devote special attention to the determination of ground-state shapes and energies. The fission-barrier height is the difference between the saddle-point energy

and the ground-state energy. We considerably improve the calculations of ground-state shapes and energies compared to those on which our 1995 mass tables [13] are based. In the 1995 work, true minimizations were done in a two-dimensional coordinate space on a fairly coarse grid. Two extra degrees of freedom were separately investigated in one-dimensional studies with these two coordinates held fixed. We have improved the specification of the ground state in several ways. The determination of the ground-state energy is based on a calculation in a 4 dimensional grid in $\epsilon_2, \epsilon_3, \epsilon_4, \epsilon_6$, with a spacing of 0.01 in all 4 coordinates. In addition we study the effect of axial asymmetry in a 3D deformation space. Finally, the decision of which of several minima is the ground state is based on a consideration of the fission-barrier height with respect to the various minima.

Our complete results are too extensive to present in a paper of this type so we have elected to present here: (1) Calculated barrier heights (one number) for 1585 nuclei from $Z = 78$ to $Z = 125$ from the proton drip line

to about 5 neutrons beyond β stability. (2) Calculated “double-humped” barrier structure for 135 actinide nuclei from Th to Es. (3) How characteristic features of the saddle-point shape, features that only emerge in very detailed fission potential-energy calculations have substantial influence on saddle-point level densities. More neutron-rich nuclei are not accessible on earth and will be discussed in a subsequent paper with an astrophysical focus. It is expected that the detailed information on the structure of fission barriers that we have uncovered will go beyond “statics” and also be useful in improving and constraining nuclear reaction codes used to model cross sections and support future advances in the ENDF/B-VII cross-section data base [25]. Apart from level-density results we also give some examples of fission half-life calculations based on our calculated potential-energy surfaces.

II. MODELS

We calculate the fission potential energy as a function of shape in the macroscopic-microscopic model. Because our model of the nuclear potential energy is not an analytical expression in terms of deformation parameters, there is in a static calculation no *a priori* way to know which shapes we need to study to find the optimum path and saddle point between a single ground-state shape and separated fragments. We need to calculate the energy for all shapes that could conceivably be relevant. In the nuclear-physics community there have existed significant misconceptions about the need to calculate the energy for **all** shapes that might be of relevance. Various shortcuts have been employed, such as minimization with respect to additional shape degrees of freedom beyond, for example, the quadrupole and octupole moments in either macroscopic-microscopic calculations, or constrained Hartree-Fock models. These shortcuts are inadequate as we discuss in Sects. III and IV. The issues involved may be made more clear by use of an analogy, namely finding the optimal route and lowest saddle point (“pass”) between the US Atlantic and Pacific coasts. This problem cannot be solved by considering only local properties of the topography. The solution requires a global consideration of the entire landscape of the United States [26]. The same is true for the energy landscape relevant to fission. It is necessary to have available for analysis a “topographical map” of the entire landscape. We now define the shape coordinates we have chosen to study in order to obtain a sufficiently complete landscape.

A. Shape parametrizations

The potential-energy surfaces that serve as the starting point for finding saddle points, minima, and other structures such as fission valleys beyond the outermost saddle are calculated in three different shape

parametrizations, depending on the deformation region studied. Our aim is to use an optimal parametrization in each region of deformation. We believe our studies are unique in their capability to use more than one shape parametrization in the same physical model, and to compare them in regions where they overlap (See Sect. IV). The three parametrizations we use are the Nilsson perturbed-spheroid parametrization, the β parametrization, and the Swiatecki-Nix three-quadratic-surface (3QS) parametrization [27, 28]. The ϵ parametrization is able to describe shapes from somewhat oblate shapes through the sphere out to shapes in the vicinity of the fission-isomeric state. We use it to describe axially asymmetric shapes in the region between the prolate and oblate axes out to $\epsilon_2 = 0.75$. The β parametrization, in which the β 's are coefficients in an expansion in spherical harmonics of the nuclear surface function, restricted in this work to axial symmetry, describes shapes in the same region, but is useful to slightly larger deformations. However, because it is an expansion, many terms would be required to describe realistic saddle-point shapes with small necks. Although it is indeed trivially simple to describe shapes with small necks in this parametrization, a major difficulty is that no **independent** control can be exercised over the shapes of the emerging fragments late in the fission process. Thus, it is difficult to generate a smooth shape consisting of, for example, an exactly spherical, partially formed fragment joined by a neck region to a partially formed deformed fragment. In the 3QS parametrization, on the other hand, these exactly spherical and spheroidal partial fragments are easy to describe. The 3QS parametrization is therefore the most suitable of the three for studying shapes from the fission-isomeric minimum to scission. Shapes and energies of the fission-isomeric state can be calculated accurately in all three parametrizations and the energies and deformations obtained with the three different parametrizations agree very well as we elaborate below. This agreement constitutes an excellent test of our model and computer codes. For our tables and figures we compare the results in all three parametrizations and choose the lowest result obtained for the minima and saddle points. We now define the three parametrizations and how we choose our deformation grid in each of them.

1. Nilsson perturbed spheroids

For small to moderate deformations we use the Nilsson perturbed-spheroid (ϵ) parametrization. Because its precise definition is quite lengthy we refer to our mass paper [13] for complete details. (Some misprints are corrected in Ref. [29].) We calculate the potential energy in a three-dimensional deformation space versus ϵ_2 (elongation), ϵ_4 (neck coordinate), and γ (axial asymmetry) for the deformation space spanned by

$$\begin{aligned} \epsilon_2 &= (0.0, 0.025, \dots, 0.75), \\ \gamma &= (0.0, 2.5, \dots, 60.0), \text{ and} \end{aligned}$$

$$\epsilon_4 = (-0.12, -0.10, \dots, 0.14)$$

altogether 10850 different shapes for each nucleus. Our immersion method (see Sect. III) is used to investigate the structure of each potential-energy surface we calculate. Specifically we tabulate all minima and the saddle points between all possible pairwise combinations of minima. We use all axially symmetric minima found to calculate improved ground-state energies and deformations. We use the ϵ_2 and ϵ_4 values at these minima as starting points for a separate minimization in a four-dimensional space defined by the coordinates ϵ_2 , ϵ_3 , ϵ_4 , and ϵ_6 . Two minimizations are performed, one starting with $\epsilon_3 = 0.0$ and $\epsilon_6 = 0.0$ and a second starting with $\epsilon_3 = 0.1$ and $\epsilon_6 = 0.0$. All four coordinates are varied in steps of 0.01.

2. Multipole expansion

One commonly used parametrization of nuclear shapes is the β parametrization. It is an expansion of the radius vector in spherical harmonics:

$$r(\theta, \phi) = R_0 \left(1 + \sum_{l=1}^{\infty} \sum_{m=-l}^l \beta_{lm} Y_l^m \right) \quad (1)$$

where R_0 is deformation-dependent so as to conserve the volume inside the nuclear surface. When only axially symmetric shapes are considered the notation β_l is normally used for β_{l0} . Since the spherical harmonics Y_l^m are orthogonal, one may determine the β parameters corresponding to any shape defined by a radius vector $r(\theta, \phi)$ in any parametrization, including the ϵ parametrization, by use of

$$\beta_{lm} = \sqrt{4\pi} \frac{\int r(\theta, \phi) Y_l^m(\theta, \phi) d\Omega}{\int r(\theta, \phi) Y_0^0(\theta, \phi) d\Omega} \quad (2)$$

where r is the radius vector in the other parametrization. Higher-order β parameters corresponding to a specific shape in the ϵ parametrization are generally non-zero even if the higher-order ϵ parameters are identically zero. A shape in the ϵ parametrization for which $\epsilon_2 \neq 0$ and all higher ϵ_ν are zero is a pure spheroid, and conversely a shape with only $\beta_2 \neq 0$ is *not* a pure spheroid.

We use the axially symmetric β parametrization to calculate constrained one-dimensional ‘‘fission-barrier’’ curves that are plotted as a function of the charge quadrupole moment Q_2 . We use two different elongation constraints, namely (1) the distance r between mass centers of the two parts of the nucleus [18, 21, 30, 31] and (2) β_2 . For each of the two constraints we minimize the energy with respect to β_3 , β_4 , and β_6 , using the values at the previous elongation as starting values. During the minimization iterations using the constraint r , β_2 is varied so that the constraint is maintained. We do this mainly to illustrate that constrained methods in practice

may yield incorrect saddle points. However, minima are usually correctly given by this procedure. As mentioned earlier when we tabulate or plot a saddle-point energy or the energy of a minimum we look at the results obtained for this particular point in all three parametrizations and use the lowest value.

3. Three quadratic surfaces

From Sect. III it is clear that to determine the structure of a multidimensional fission potential-energy function it is necessary to calculate a *complete hypercube or hypervolume* in the multi-dimensional space. Because nascent-fragment shell effects strongly influence the structure of the fission potential-energy surface long before scission, often by the outer saddle region, it is crucial to include the nascent-fragment deformations as two independent shape degrees of freedom. In addition, elongation, neck diameter, and mass-asymmetry degrees of freedom are also necessary leading to a minimum of 5 shape coordinates required to adequately describe the fission potential-energy surface in the region between the fission isomer and scission.

The 3QS parametrization ideally satisfies these requirements. In this parametrization the shape of the nuclear surface is specified in terms of three smoothly joined portions of quadratic surfaces of revolution. They are completely specified [28] by

$$\rho^2 = \begin{cases} a_1^2 - \frac{a_1^2}{c_1^2}(z - l_1)^2 & , \quad l_1 - c_1 \leq z \leq z_1 \\ a_2^2 - \frac{a_2^2}{c_2^2}(z - l_2)^2 & , \quad z_2 \leq z \leq l_2 + c_2 \\ a_3^2 - \frac{a_3^2}{c_3^2}(z - l_3)^2 & , \quad z_1 \leq z \leq z_2 \end{cases} \quad (3)$$

Here the left-hand surface is denoted by the subscript 1, the right-hand one by 2 and the middle one by 3. Shapes 1 and 2 are spheroids, for which c is the semi-symmetry axis length, a is the semi-transverse axis length, and l specifies the location of the center of the spheroid. The middle body may be a spheroid or a hyperboloid of one sheet, for which c_3 is imaginary. At the left and right intersections of the middle surface with the end surfaces the value of z is z_1 and z_2 , respectively. Surfaces 1 and 2 are also referred to as end bodies and, alternatively, nascent fragments. They are indicated in red in Fig. 2.

There are eleven numbers required to specify the expressions in Eq. (2) but the conditions of constancy of the volume and continuous function and first derivative at z_1 and z_2 eliminate five numbers. The introduction of an auxiliary unit of distance u through

$$u = \left[\frac{1}{2} (a_1^2 + a_2^2) \right]^{\frac{1}{2}} \quad (4)$$

permits a natural definition of two sets of shape coordinates. We define three symmetric coordinates σ_i and

three reflection-asymmetric coordinates α_i by

$$\begin{aligned}
\sigma_1 &= \frac{(l_2 - l_1)}{u} \\
\sigma_2 &= \frac{a_3^2}{c_3^2} \\
\sigma_3 &= \frac{1}{2} \left(\frac{a_1^2}{c_1^2} + \frac{a_2^2}{c_2^2} \right) \\
\alpha_1 &= \frac{1}{2} \frac{(l_1 + l_2)}{u} \\
\alpha_2 &= \frac{(a_1^2 - a_2^2)}{u^2} \\
\alpha_3 &= \frac{a_1^2}{c_1^2} - \frac{a_2^2}{c_2^2} \quad (5)
\end{aligned}$$

The coordinate α_1 is not varied freely but is determined by the requirement that the center of mass be at the origin, which leaves us with five independent shape coordinates.

When a grid of deformation points is selected in the 3QS parametrization, a substantial practical problem is that not all values of the deformation parameters correspond to a physical shape. Another complication is that some of the shape parameters are rather indirectly related to more familiar quantities associated with nuclear shapes. To generate a reasonable deformation grid in the 3QS parametrization we therefore select the input deformations by starting from more familiar geometrical concepts.

First, it is reasonable to expect that at some stage of the fission process the shape of the emerging fragments will start to resemble the ground-state shapes of the final fragments. In terms of the Nilsson perturbed-spheroid ϵ_2 parameter [32–34] we designate the shape of surface 1 by ϵ_{f1} and the shape of the other end body by ϵ_{f2} . The deformation parameters σ_3 and α_3 are connected to ϵ_{f1} and ϵ_{f2} by the relations

$$\sigma_3 = \frac{1}{2} \left[\left(\frac{3 - 2\epsilon_{f1}}{3 + \epsilon_{f1}} \right)^2 + \left(\frac{3 - 2\epsilon_{f2}}{3 + \epsilon_{f2}} \right)^2 \right] \quad (6)$$

and

$$\alpha_3 = \left[\left(\frac{3 - 2\epsilon_{f1}}{3 + \epsilon_{f1}} \right)^2 - \left(\frac{3 - 2\epsilon_{f2}}{3 + \epsilon_{f2}} \right)^2 \right] \quad (7)$$

In our present calculation we investigate spheroidal shapes of the end bodies that in terms of ϵ_{f1} and ϵ_{f2} correspond to the set

$$\{-0.2, -0.15, -0.1, 0.00, 0.1, 0.15, 0.175, 0.2, 0.225, 0.25, 0.275, 0.3, 0.35, 0.4, 0.5\} \quad (8)$$

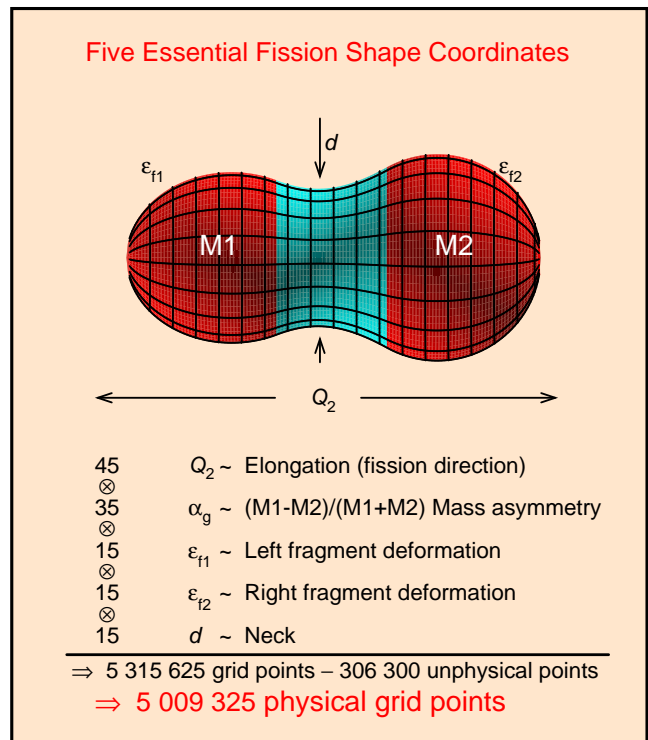


FIG. 2: (Color online) Five-dimensional shape parametrization used in the potential-energy calculations. Different colors indicate the three different quadratic surfaces defined by Eq. (3). The first derivative is continuous where the surfaces meet. Note that everywhere in this paper we give the charge quadrupole moment Q_2 in terms of ^{240}Pu with the same shape as the nucleus considered, so there is no nuclear size or charge effect in Q_2 . The end-body masses, or equivalently volumes, M_1 and M_2 , refer to the left and right nascent fragments were they completed to closed shapes. For the nascent spheroidal fragments we characterize the deformations by Nilsson’s quadrupole ϵ parameter.

This set includes most fission-fragment ground-state shapes. It is not necessary to consider higher deformation components such as ϵ_4 . For ground states of nuclei lighter than the rare earths, that is, in the fission-fragment region relevant to this study, higher shape multipoles usually lower the ground-state energies by considerably less than an MeV. Thus we have 15 left- and 15 right-fragment deformations. Each nascent-fragment deformation set includes the sphere and three oblate shapes.

A common notation used to characterize the fragment mass asymmetry of a fission event is M_H/M_L where M_H and M_L are the masses of the heavy and light fission fragments, respectively. For the purpose of grid generation for the potential-energy calculation it is convenient to relate a mass-asymmetry shape degree of freedom for the precission nucleus to the final fission-fragment mass asymmetry in some fashion, although the final mass division, strictly speaking, cannot be determined from the static shapes occurring before scission. However, the exact nature of our definition of mass asymmetry for a sin-

gle shape has no effect on the calculated saddle-point energies and shapes because our five-dimensional grid covers all of the physically relevant space available to the 3QS parametrization, regardless of how we choose to define the “mass-asymmetry” coordinate. So that we obtain equations that are reasonably simple to work with for the purpose of grid generation, we define an auxiliary grid mass-asymmetry parameter α_g

$$\alpha_g = \frac{M_1 - M_2}{M_1 + M_2} \quad (9)$$

where M_1 and M_2 are the volumes inside the end-body quadratic surfaces, were they completed to form closed-surface spheroids. Thus

$$\alpha_g = \frac{a_1^2 c_1 - a_2^2 c_2}{a_1^2 c_1 + a_2^2 c_2}. \quad (10)$$

The 3QS parameter α_2 is then completely determined by the relation

$$\alpha_2 = 2 \frac{\left(\frac{(\alpha_g + 1)^2 (2\sigma_3 + \alpha_3)}{(\alpha_g - 1)^2 (2\sigma_3 - \alpha_3)} \right)^{1/3} - 1}{\left(\frac{(\alpha_g + 1)^2 (2\sigma_3 + \alpha_3)}{(\alpha_g - 1)^2 (2\sigma_3 - \alpha_3)} \right)^{1/3} + 1} \quad (11)$$

for specific values of ε_{f1} and ε_{f2} of the end bodies, which determine σ_3 and α_3 . With this definition we select 35 grid points corresponding to

$$\alpha_g = -0.02 \dots (0.02) \dots 0.66 \quad (12)$$

We have closely spaced the asymmetry coordinate so that points on the grid close to fragment magic proton and neutron numbers will be included; in a more sparsely spaced grid they may not appear. For ^{240}Pu the values 0.00, 0.02, and 0.66 of the mass-asymmetry coordinate α_g correspond to the mass divisions 120/120, 122.4/117.6, and 199.2/40.8, respectively.

Because of the intuitive appeal of the notation M_H/M_L we use it below to characterize the “asymmetry” of a single shape. We then connect M_H and M_L to α_g through

$$M_H = A \frac{1 + \alpha_g}{2} \quad \text{and} \quad M_L = A \frac{1 - \alpha_g}{2} \quad (13)$$

for a nucleus with A nucleons for which the left fragment is heavier than the right, which is the case for all our examples below. For shapes with a well-developed neck the ratio obtained with this definition can be expected to be close to but not equal to the final fragment mass-asymmetry ratio. We cannot conveniently use M_1 and M_2 to designate the final fragment mass asymmetries because they do not sum up to the total nuclear volume or mass. Equation (13) simply represents a scaling of M_1 and M_2 so that their sum after scaling adds up to the total mass number A .

We select the deformation parameter σ_1 so that our grid consists of 45 values of the quadrupole moment Q_2 .

That is, for each combination d , α_g , ε_{f1} , and ε_{f2} we determine by a numerical procedure 45 values of σ_1 so that 45 preselected values of Q_2 are obtained.

The electric multipole moment Q_λ for a homogeneously charged, sharp-surfaced volume is defined by

$$Q_\lambda = 2 \left(\frac{3Z}{4\pi r_0^3 A} \right) \int_V r^\lambda P_\lambda(\cos\theta) d^3r \quad (14)$$

In a cylindrical coordinate system, such as the 3QS parametrization, this simplifies to

$$Q_\lambda = \left(\frac{3Z}{r_0^3 A} \right) \int_V \sqrt{\rho^2 + z^2} \lambda \rho P_\lambda\left(\frac{z}{\sqrt{\rho^2 + z^2}}\right) d\rho dz \quad (15)$$

In order to remove a trivial size and charge effect, we normalize the value of Q_λ to that possessed by a ^{240}Pu nucleus having the same shape.

In the selection of σ_2 values it is useful to observe that for small values of σ_1 there is a minimum neck diameter $d > 0$. At a certain transition point $\sigma_1 = \sigma_{1t}$ a zero-width neck $d = 0$ can form. This transition configuration, for which the middle body is absent, is the scission configuration of completely formed spheroidal fragments, or, alternatively the *polar-parallel* [35] touching configuration of colliding heavy ions. For this configuration we find in the completely general case of arbitrary mass asymmetry and end-body eccentricities:

$$\sigma_{1t} = \frac{\sqrt{\frac{\alpha_2 \alpha_3 - 2\alpha_2 \sigma_3 + 2\alpha_3 - 4\sigma_3}{\alpha_2 \alpha_3 + 2\alpha_2 \sigma_3 - 2\alpha_3 - 4\sigma_3}} + 1}{\sqrt{\frac{\alpha_3 - 2\sigma_3}{\alpha_2 - 2}}} \quad (16)$$

Because the fission saddle point occurs before scission for heavy systems we do not investigate the separated-fragment configurations requiring a two-sheet hyperboloid for the middle body that can occur in the region $\sigma_1 > \sigma_{1t}$. Thus, for $\sigma_1 < \sigma_{1t}$ the minimum value of the neck that we consider is the minimum value allowed by the parametrization. For $\sigma_1 > \sigma_{1t}$ the minimum value of the neck is zero, corresponding to a scission configuration. Based on these considerations we select 15 values of σ_2 so that we for each combination of Q_2 , ε_{f1} , ε_{f2} , and α_g obtain a suitable spacing for d in the range between the smallest and largest value possible for this highly nonlinear variable.

This choice of deformation coordinates would be expected to yield 5315625 grid points in the full 5-dimensional space of the parametrization. In fact, our study completely exhausts the physically relevant space available in this parametrization. However, shapes corresponding to certain quadrupole moments do not exist for specific combinations of the other shape parameters. For example, zero quadrupole moment cannot be realized for shapes with very prolate end fragments. In our grid there exist 306300 such “unphysical” points. Thus we are left with 5009325 shapes for which we actually calculate the potential energy.

To summarize, we consider the physically relevant part of the full 5-dimensional space of the 3QS parametrization in terms of 45 values of the renormalized charge quadrupole moment Q_2 , 15 values of the neck diameter d , 15 values of the fragment deformations ε for each of the two nascent fragments, and 35 values of the mass asymmetry $\alpha_g = (M_1 - M_2)/(M_1 + M_2)$, where M_1 and M_2 are the volumes of the left and right nascent fragments were they completed to closed shapes. The various shape coordinates are enumerated in Fig. 2 where an example of a shape is shown. We have earlier [8] emphasized that it is important to consider a *dense* grid in ε and mass asymmetry because fragment shell corrections vary rapidly in a narrow range of these deformation coordinates. For example, near ^{132}Sn the microscopic corrections vary by 1 MeV for a change of Z or N by 1 unit [13].

B. Potential energy

For a specific prescribed shape the main steps to determine the potential energy are the following:

1. The macroscopic surface, Coulomb, and additional shape-dependent energy terms, if any, are calculated and the macroscopic energy is determined.
2. A single-particle potential of the prescribed shape is generated numerically on a spatial grid of sufficient density to yield the required accuracy in numerical calculations of the matrix elements of the Hamiltonian.
3. The single-particle Hamiltonian based on the above spatial part plus a spin-orbit interaction is diagonalized and single-particle levels are obtained.
4. The single-particle levels serve as the starting point to calculate the microscopic shell corrections for protons and neutrons by use of Strutinsky's method [5, 6] and microscopic pairing corrections based on the Lipkin-Nogami method in the form implemented in Ref. [19].
5. The shell- and pairing-correction terms for neutrons and protons are added to the macroscopic energy to obtain the total potential energy. All total potential energies in this work are expressed with respect to our defined reference point, the macroscopic energy of the spherical shape.

The single-particle model used in our calculation is the folded-Yukawa model completely specified in our 1995 mass paper [13], with additional discussions and investigations in Refs. [14–22]. For the macroscopic model we use the finite-range liquid-drop model which is also specified in that paper, supplemented by the explicit inclusion of a shape-dependent Wigner energy [12, 18], which only contributes for shapes with necks. However, because the use of many more points in more general deformation spaces

systematically leads to lower saddle points than were obtained for fission barriers in the 1995 paper, which used more than 20000 times fewer points, it was necessary to redetermine the coefficients of the macroscopic finite-range liquid-drop model. This work is described in Ref. [12]. It is noteworthy that the improved barrier modeling led to a model in which calculated barriers agree with data significantly better than in the 1995 model, while the mass-model error also decreased, by more than 2%, although all the ingredients other than the macroscopic-energy coefficients in the mass model itself were not changed. In our studies of large-dimensional deformation spaces we have observed that the other macroscopic model used in the 1995 mass paper, the finite-range droplet model (FRDM), cannot be applied to strongly deformed shapes with narrow neck regions. Such shapes are important for describing saddle points of lighter nuclei, and for modeling the fission process between the saddle and the scission points. The reason is that some of the terms occurring in the finite-range droplet-model energy expression were derived assuming small deformations around a spherical shape. However, we find that this model is still our preferred model for nuclear masses since it describes masses more accurately than the mass model based on the finite-range liquid-drop macroscopic model and since no ground states involve such highly deformed shapes.

Our main emphasis is to calculate fission-barrier heights. Fission barriers of actinide nuclei are often “double-humped” and the first saddle, second (fission-isomeric) minimum and second saddle are usually denoted by E_A , E_{II} , and E_B respectively. Outside a narrow range of actinide nuclei the fission barrier is more complex than a simple double-humped barrier and the above parameters cannot be uniquely defined from the calculated potential-energy surfaces. We will elaborate later. However, all calculated potential-energy surfaces uniquely possess *one* maximum fission-barrier height and for most nuclei in our study we therefore present only this unique fission-barrier height.

In a few cases we present complete fission-barrier curves, that is we plot the energy along optimal paths in the higher-dimensional energy landscapes versus deformation. In the region beyond the fission-isomeric state there is often more than one valley in the calculated five-dimensional energy landscape. The valleys are separated by ridges, which can be several MeV high. Sometimes distinctly different saddle points separate these valleys from the fission-isomeric state. In other cases the additional valleys in the landscape develop beyond the outer saddle so that there is only one saddle between these valleys and the fission-isomeric states. For a few nuclei we present some of these features in the fission-barrier plots.

In our computer model most of the time is used to calculate the single-particle levels. Once the levels are determined the time needed to calculate the shell corrections and macroscopic contributions to the potential energy is almost negligible. The same set of levels can be

used to calculate the shell corrections for several neighboring nuclei to satisfactory accuracy. However, excursions too far away would lead to inaccuracies because the single-particle well radius changes with the size of the system and other parameters such as the spin-orbit strength also change slowly with nuclear size. In our calculation we consider nuclei between the neutron and proton drip lines (beyond which nuclei are unstable with respect to neutron or proton emission) from $A = 171$ to $A = 330$. We divide this region into 24 sub-regions, each of which is sufficiently limited so that within each region the shell correction can be calculated from the same set of single-particle levels. These regions are defined by first selecting nuclei lying in 8 strips with mass number A between 171 and 190, 191 and 210 and so on, with each strip including 20 mass chains. We then divide each of these strips into three regions: one region on the proton-rich side of β stability, one region containing β -stable and near- β -stable nuclei, and one region on the neutron-rich side of β stability. In each region we calculate the energy of each nucleus for the entire space of deformations using the single-particle levels found for a central nucleus of the region.

The high-dimensional potential-energy space of each nucleus is then analyzed by immersion techniques described in Sect. III and all minima and all saddle points are identified. The energies at these deformations are recalculated with the precise model parameters for the nucleus under consideration, that is the potential radii, depths and other quantities that characterize the single-particle potential and which are all slowly varying functions of Z and N assume exactly their proper values for this nucleus. This means that we assume that the location of a minimum or saddle is less sensitive to parameter variations than is the energy itself. We have performed numerous checks of this assumption and find it is fulfilled to a very high degree.

In the β parametrization we limit ourselves to constrained calculations. As discussed in Sect. III, such an approach often does not lead to a correct determination of saddle points. However, minima are usually well determined. In the constrained calculation we vary β_2 to fulfill an elongation constraint, and minimize the energy with respect to β_3 , β_4 , and β_6 . The starting values of the higher multipoles are those of the previous point. Because the minimization approach requires the calculation of energies of so few shapes compared to the immersion approach, in this calculation we do not use a common set of single-particle levels for several nuclei, we instead perform the calculations individually for each system. We investigate two different elongation constraints. One is the distance r between mass centers of the two halves of the nucleus; for definitions see Refs. [18, 21, 30, 31]. In a second study we simply use β_2 as our elongation constraint.

C. Level densities

The relative cross sections for reflection asymmetric and symmetric fission depend on the relative level densities at the outermost saddles, as well as the barrier heights and widths [36].

We calculate nuclear level densities by microscopic combinatorics based on single-particle levels and generate intrinsic (non-collective) many-particle-many-hole excitations [37]. Pairing is treated individually for *all* configurations within the BCS formalism [38]. The BCS wave function with excited quasi-particles is given by

$$|\tau\rangle = \prod_{\nu'' \in \tau_2} (-V_{\nu''} + U_{\nu''} a_{\nu''}^\dagger a_{\bar{\nu}''}^\dagger) \times \prod_{\nu' \in \tau_1} a_{\nu'}^\dagger \prod_{\nu \in \tau_0} (U_\nu + V_\nu a_\nu^\dagger a_{\bar{\nu}}^\dagger) |0\rangle, \quad (17)$$

where τ_2, τ_1 and τ_0 denote the spaces of double, single and zero quasi-particle excitations, respectively. U_ν and V_ν are the standard BCS occupation factors and $|0\rangle$ is the particle vacuum [39].

The pairing gap Δ and the Fermi energy λ are found by solving the BCS equations

$$\Delta = G \left[\sum_{\nu \in \tau_0} U_\nu V_\nu - \sum_{\nu'' \in \tau_2} U_{\nu''} V_{\nu''} \right], \quad (18)$$

$$N = 2 \sum_{\nu \in \tau_0} V_\nu^2 + \sum_{\nu' \in \tau_1} 1 + 2 \sum_{\nu'' \in \tau_2} U_{\nu''}^2. \quad (19)$$

The pairing strength G is adjusted to reproduce the microscopic pairing gap found at the saddle in the fission potential-energy calculation.

Collective excitations, *i.e.* rotational, vibrational, and discrete symmetry degrees of freedom, contribute substantially to the total level density [40]. The rotational enhancement is taken into account combinatorially by adding a modified rotor to each of the intrinsic non-collective states obtained from the single-particle spectrum. The rotational energy is given by

$$E_{\text{rot}} = \frac{I(I+1) - K^2}{2\mathcal{J}_\perp(\Delta)}, \quad (20)$$

where I is the nuclear spin, K is the spin projection on the symmetry axis of the intrinsic state upon which the rotational band is built and $\mathcal{J}_\perp(\Delta)$ is the moment of inertia around an axis perpendicular to the symmetry axis. The moment of inertia is approximated by the rigid-body moment of inertia modified by the pairing gap as given in Ref. [41]. Given the spin projection K and parity π of the band-head the rotational band includes the following set of levels

$$I^\pi = \begin{cases} K^\pi, (K+1)^\pi, (K+2)^\pi, \dots & \text{if } K \neq 0, \\ 0^+, 2^+, 4^+, \dots & \text{if } K = 0^+, \\ 1^-, 3^-, 5^-, \dots & \text{if } K = 0^-. \end{cases} \quad (21)$$

Counting all these states, while keeping track of parity and spin, gives the combinatorial level density $\rho_{\text{comb}}(E, I, \pi)$.

The total level density is given by

$$\rho_{\text{tot}}(E, I, \pi) = \rho_{\text{comb}}(E, I, \pi)K_{\text{vib}}(E), \quad (22)$$

where K_{vib} is the collective vibrational enhancement which is here approximated by the phenomenological attenuated phonon method [42, 43].

This level-density model has been tested by calculating s-wave neutron resonance level spacings for which experimental data is available [44, 45]. For the compound nucleus (Z, N) the level spacing D_0 is given by

$$D_0 = \frac{1}{\rho_{\text{tot}}(S_n, I_0 + 1/2, \pi_0) + \rho_{\text{tot}}(S_n, I_0 - 1/2, \pi_0)}, \quad \text{for } I_0 > 0,$$

and (23)

$$D_0 = \frac{1}{\rho_{\text{tot}}(S_n, 1/2, \pi_0)}, \quad \text{for } I_0 = 0,$$

where I_0 and π_0 are the ground state spin and parity of the target nucleus $(Z, N - 1)$ and S_n is the neutron separation energy. The model is compared to data using the rms deviation factor defined in Ref. [42]

$$f_{\text{rms}} = \exp \left[\frac{1}{N_e} \sum_{i=1}^{N_e} \ln^2 \frac{D_{\text{th}}^i}{D_{\text{exp}}^i} \right]^{1/2}, \quad (24)$$

where D_{th} (D_{exp}) is the theoretical (experimental) resonance spacing and N_e is the number of nuclei in the dataset. In this model $f_{\text{rms}} = 3.2$ for 223 axially deformed nuclei ($|\varepsilon_2| > 0.05$) which is somewhat larger than the $f_{\text{rms}} = 2.13$ obtained in the HFB model in Ref. [42], but this latter model has a number of adjusted parameters. In our study we have not adjusted any parameters to level-density data.

To be able to express our microscopic results in terms of familiar concepts we will, when we present our results below, adjust the Fermi-gas expression

$$\rho(E) = \frac{\sqrt{\pi}}{12a^{1/4}(E - E_{\text{shift}})^{5/4}} \exp \left[2\sqrt{a(E - E_{\text{shift}})} \right] \quad (25)$$

to our microscopic results and tabulate the resulting values for the level-density parameter a and backshift E_{shift} .

III. ANALYSIS

Optimal saddle points between minima of a function of several variables cannot be determined by any type of local argument [26]. This is often not fully appreciated. The need to use the techniques we describe below is better understood if we start by giving a few examples of how and why the commonly-used “minimization” techniques fail.

A. Fallacies in finding saddle points

For many in the nuclear physics community there has been a serious misconception that optimal saddle points between minima of a multi-dimensional potential-energy surface can be determined by calculating and displaying the potential-energy function as a function of two shape variables, for example, β_2 and β_4 [46] or β_2 and β_3 [47, 48], where the potential-energy function for each value of the displayed coordinates has been “minimized” with respect to additional multipoles such as β_4 , β_5 , β_6 , and β_7 , or even more multipoles in, for example, Ref. [49]. To the contrary, such a procedure can yield fictitious saddle points that may be either higher or lower than the correct ones. The corresponding “saddle-point shapes” would also be different from the shapes obtained in a correct treatment of the multi-dimensional problem.

It is *also* a common misconception that *constrained* self-consistent calculations, for example HF or HFB calculations with Skyrme or Gogny forces [50, 51] automatically “take into account” all non-constrained variables in a way that will lead to accurate determination of saddle points. This assumption is incorrect as is carefully explained in Ref. [52]. Here we reproduce and discuss in more detail the simplified example in Ref. [52] and add some additional examples. Figure 3 represents in terms of a two-dimensional contour plot features that often occur in multidimensional potential-energy surfaces. Let us assume that Θ represents an elongation coordinate such as ϵ_2 or Q_2 and that α represents all additional shape degrees of freedom. Often the essential features of such a high-dimensional potential-energy surface are represented by a one-dimensional (fission-barrier) curve. The aim in constructing such a curve is to include the optimal or lowest saddle point between successive minima. We illustrate in Fig. 3 that when using some common strategies, the optimal saddle points are **not** correctly identified. Let us assume we wish to plot in terms of the one variable Θ the optimal path and in particular include on this path the saddle point between the lowest point on the left vertical axis of the diagram at $\Theta = -100$ and $\alpha = 9.1$ and the lowest point on the right vertical axis at $\Theta = 100$ and $\alpha = -9.1$. It may then sound plausible, in particular if we study a function of more than two variables and cannot easily display it, that this optimal saddle point can be identified by plotting for each value of Θ the lowest point with respect to the other variables. This technique has been applied in macroscopic-microscopic calculations and is what effectively occurs in constrained HF calculations.

Why are these minimization techniques used at all? In the macroscopic-microscopic method we are using, prior to about 2000 [8] it was not practical to calculate the potential energy for large numbers of shapes using a relatively large number of shape degrees of freedom. Instead, the lowest point (the ground state) was located, then an elongation (fission) coordinate was incremented and then constrained, with the energy defined as the min-

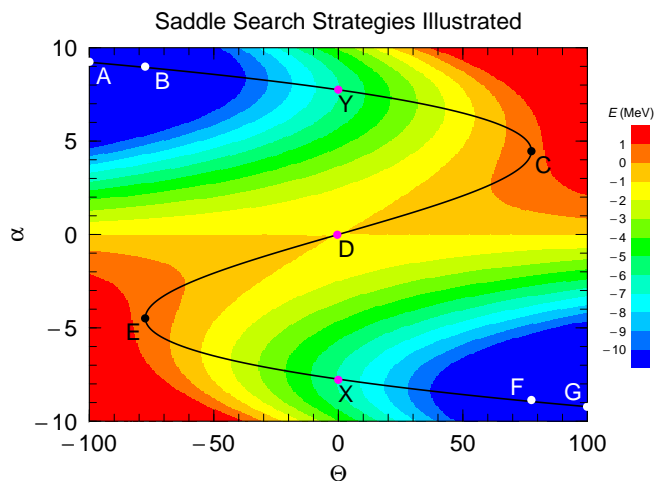


FIG. 3: (Color online) Two-dimensional schematic surface for which “minimizations” or constrained calculations fail. Blue colors represent lower energies, redder ones higher energies. The parameter Θ represents an elongation (fission) coordinate and α represents all other coordinates. The solid line, defined by the condition of zero derivative of the energy with respect to α for constrained Θ , follows valleys and ridges in the surface, and passes through the true saddle point. The mathematical representation of this surface was given in Ref. [52].

imum with respect to all the other coordinates, using their previous values as a starting point. This procedure yields a potential-energy curve as a function of a single fission variable. In constrained, self-consistent calculations, such as constrained Hartree-Fock, this is what happens more or less automatically. We should emphasize that minimization does not necessarily lead to the wrong solution; in many simple problems it will give the correct saddle point. Unfortunately, one cannot know *a priori* whether a true or incorrect solution will be found.

Referring again to Fig. 3, the technique of minimization sounds very plausible, because what we want to find is the optimal, minimum-energy path between the two low points at the edges of the contour diagram. However, if the energy is minimized with respect to α for various fixed elongations, starting on the left side of the plot then the upper valley will be followed if the previous value of α is used as a starting coordinate in the minimizations for successive Θ 's. Toward the right of the figure the upper valley disappears and a discontinuous jump in energy leading to the lower valley occurs. This is a common situation in constrained Hartree-Fock fission calculations. The sequence of points followed will be A, B, Y, C, F and G. The true saddle point, D, is located in the center of the figure. Similar difficulties occur when a potential-energy function is minimized with respect to higher multipoles and displayed as a function of β_2 and β_3 . The barrier curve inferred from the resulting two-dimensional contour plot may once again be very different from one derived from the full multi-dimensional

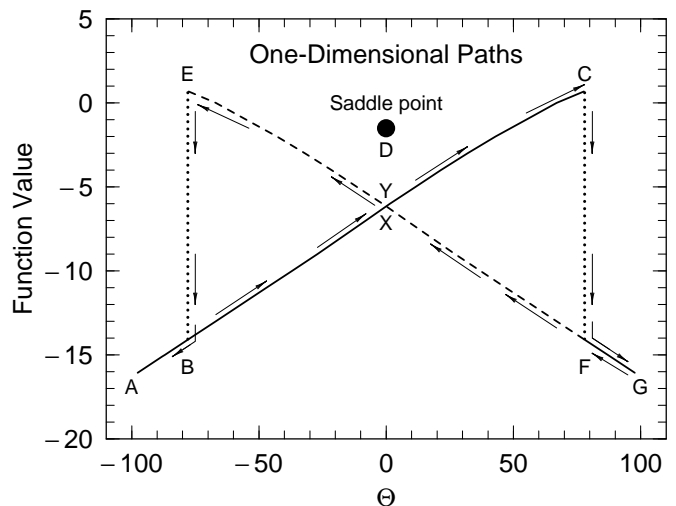


FIG. 4: Potential-energy curves obtained by local minimization of the two-dimensional surface given in Fig. 3. The true saddle point in this two-dimensional surface is represented by the black dot, which does not lie on any of the curves obtained by minimization. The arrows along the curves in the figure follow the time-line of the discussion in the text of Fig. 3, starting with the 30 degree upward-pointing arrow near the lower left of the figure.

function.

In Fig. 4 we show as a solid black line the monotonically increasing function, the “fission barrier,” we obtain by use of this strategy applied to the function in Fig. 3. At the turnaround point C in the solid curve between the upper valley and the middle ridge, occurring when the upper valley ceases to exist, there is a discontinuous drop in the energy and a transition into the lower valley. The energy along the path now followed in the lower valley is also shown as a solid line in Fig. 4. In constrained calculations it is sometimes customary to follow the solution in the lower valley backward. We then would follow the lower valley until it also disappears. The continuation of the lower solution backward is indicated by a dashed line in Fig. 4 and would involve points G, F, X, E, B and A, in that order. Since in this 2-dimensional example we actually can display the potential surface it is clear that the real saddle point D is located at $\Theta = 0$ and $\alpha = 0$. In cases where the surface can not be as easily displayed it has previously sometimes been assumed that the high point C on the solid line in Fig. 4 is the saddle, on other occasions that the intersection between the solid and dashed curve in Fig. 4, the overlap between points X and Y, is the saddle point. In reality the saddle energy is in between these two energies. For one constraint, typically the mass quadrupole moment Q_2 , self-consistent calculations often result in deficient solutions looking very much like those obtained in our example, see for example Ref. [50]. Another important consequence of using this procedure is a possible improper determination of the shape or structure of the true saddle

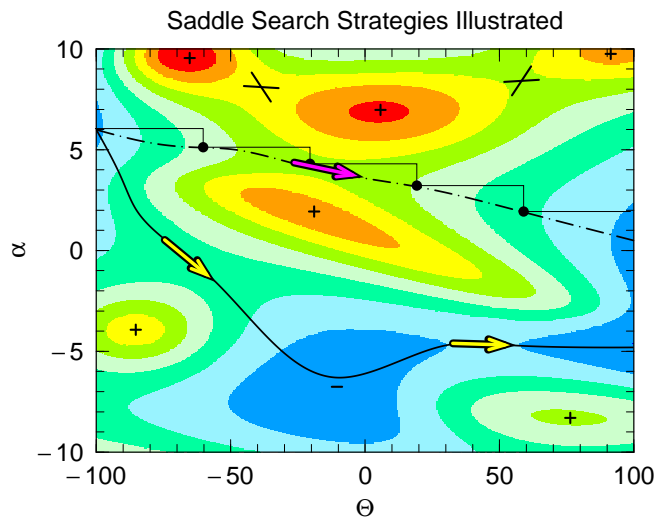


FIG. 5: (Color online) Maxima (+), minima (-), and saddle points (arrows or crossed lines) of a two-dimensional function. As discussed in the text it is not possible to obtain a lower-dimensional representation of the optimal path across this surface by “minimizing” with respect to the “additional” (α) shape degree of freedom. The function increases in value as the colors progress from blue to red.

point. In Sect. IV and in the Appendix we discuss actual examples of problems encountered for realistic nuclear potential-energy surfaces.

If instead two constraints are used, a two-dimensional contour map will be created. Then one may attempt to identify the true multi-dimensional saddle point with an apparent saddle point in the contour plot. In this situation, such as when two constraints are used in self-consistent calculations, as occurs in the study in terms of the quadrupole and octupole constraints in Ref. [51], two or more solutions, or sheets, may be obtained. The true saddle point lies somewhere in the multi-dimensional space between these sheets. When surfaces are obtained in terms of two variables in constrained calculations, a new complication relative to calculations versus one constrained variable, is how to decide what starting configuration to use at each grid point. In macroscopic-microscopic calculations values of the higher multipole parameters at “the previous point” are often used for the next point. In Hartree-Fock calculations a similar approach is used. But the definition of “the previous point” is not unique, in contrast to the one-dimensional case, because it depends upon the direction from which the particular point is approached. Another strategy employed is to calculate a complete grid in the additional multipoles for each value of Θ and plot the absolute minimum in this high-dimensional space. In the example here this method would yield as the saddle point the intersection point between the points X and Y on the two curves in Fig. 4 at $\Theta = 0$ and a function value about -6.5 , much lower than the real saddle point at -1.5 . In this situation, one might identify as the fission barrier the A, B,

X, F, G curve with an unphysical cusp at the top of the barrier.

For other types of potential-energy surfaces one may avoid the obvious discontinuities and cusps and obtain continuous functions versus elongation when the function is minimized with respect to additional shape degrees of freedom. But this still does not guarantee that the optimal saddle point is located on the curve obtained. Still sticking to the easy-to-visualize case of two dimensions, we show a more complex surface in Fig. 5. Because of the multiple saddle points, it is not clear *a priori* which one corresponds to the fission threshold. Therefore even if we could determine the location and energies of all points where the first derivatives are zero, we still could not determine which of these is the optimal saddle point. Let us use the minimization strategy and study the outcome. We identify the point $\Theta = -100$, $\alpha = 6$ as the ground state or fission-isomeric state and proceed to find a “constrained” fission barrier. From the starting point we increase Θ by 40 (smaller steps will not alter the result) while keeping α fixed. From the new position we then minimize with respect to α and find ourselves at the first black dot. When we repeat this process we obtain the dot-dashed curve. The energy along this path is a continuous function and the magenta arrow would be identified as the fission saddle point. However, this saddle is higher than those shown by yellow arrows, which can only be found when the full space is explored and which are located on the optimal fission path in terms of energy height.

B. Immersion method

A method that allows the unambiguous identification of the optimal saddle point between two minima was described in Ref. [53]. As presented there the method only allows the determination of the energy of the optimal saddle, which in fission potential-energy surfaces corresponds to the fission threshold energy. It was not discussed how to identify at what deformation the saddle is located. It was apparently unknown to the authors of Ref. [53] that the method of *immersion* had long been used in other fields, in particular in geography [26, 54]. A familiar example would be the determination of the location of the “continental divide” in the US. Again, the method is best explained by considering a two-dimensional case. We imagine that we have a geographical landscape of minima, maxima and saddle points and that we are looking for the minimum-height pass or saddle point between two minima of interest, the first being where we are, the second where we want to go. Instead of just searching for a saddle point between two minima we may also search for a saddle between a minimum, for example the fission-isomeric state, and a valley, for example a valley near the scission point. In this discussion we will designate the minima or valleys on opposing sides of the searched-for saddle point by “entry

point” and “exit point.”

We recall that the energy is defined in a multidimensional space defined by a set of shape coordinates, with each coordinate taking on a specific set of values. In other words, the potential energy is defined on a mesh in coordinate space. Identifying a minimum is very straightforward, as the energy at any local minimum has a lower value than all of its nearest neighbors on the mesh. To start, we fill the minimum where we are with “water” up to some level (we will be concrete about how we immerse our landscapes to facilitate the explanation, but the reader may feel free to imagine some other metaphor). We define the lowest grid point to be “wet.” We then select a filling level above the ground-state energy and scan the entire coordinate grid, at each point determining: 1) if the energy is below the filling level, and 2) if the point has a nearest neighbor which is wet. If both are true, that point is set to be wet. This scan is repeated until no new points are switched to wet in the last repetition. The water level is now raised and the iterations are repeated. At some sufficiently high water level the exit point will become wet. This level defines an upper limit to the saddle-point energy.

To relatively quickly obtain an accurate value of the saddle-point energy we start by choosing a large spacing between successive filling levels. Once determining the level where the exit point becomes wet, the process is repeated starting from the previous level, but with a decreased increment, until we have determined the energy of the saddle point to the desired precision.

It remains to determine the **location** of the saddle point, or equivalently the shape of the nucleus at the saddle point. It is also of interest to investigate if there are additional saddle points in the potential and determine if possible their significance. Furthermore, we might wish to determine if different fission modes exist, perhaps expressed as distinctly different valleys in the potential-energy surface, and if they are accessed across different saddle points. We consider these issues in the next section and when we present results of our analysis of the calculated potential-energy surfaces.

C. Computer model of immersion

In Fig. 6 we illustrate schematically in two dimensions how we simulate immersing the multi-dimensional energy landscape. The energy landscape is stored in the matrix E . This matrix has five indices corresponding to the values of the five shape coordinates defined on a grid. Another matrix IW indicates if a point is wet (1) or dry (0). To determine the saddle-point height between the entry point (solid circle near the lower left of the figure) $(I_1^a, I_2^a, I_3^a, I_4^a, I_5^a)$ and the exit point (solid circle near the upper right of the figure) $(I_1^b, I_2^b, I_3^b, I_4^b, I_5^b)$ we start by initializing all elements of IW to 0. Then we set $IW(I_1^a, I_2^a, I_3^a, I_4^a, I_5^a) = 1$, making the entry point wet. We now add water to the ground state until the exit point

becomes wet, that is when the water has overflowed the saddle between the entry and exit points. We start by filling the ground state with water to a specified height above the ground state, say 1 MeV. We assume that the edge of the “1-MeV pool” in Fig. 6 is given by the contour line around the ground-state minimum. The filling up to the 1-MeV level is done by checking each location, one by one. At each location we set IW equal to 1, if and only if the energy at the location is less than 1 MeV above the ground-state energy **and** one of the neighboring points is wet. The plus signs surrounded by small circles are points which have become wet ($IW=1$) at some stage of this first iteration, the other points remaining dry so far. This loop is repeated several times, until we have performed a final iteration in which no elements of IW change from their previous values. At this point we check the value of $IW(I_1^b, I_2^b, I_3^b, I_4^b, I_5^b)$. If it is 0, then the water has not overflowed the saddle and we raise the water by 1 MeV and repeat the procedure. The water level is raised until the exit point becomes wet, that is $IW(I_1^b, I_2^b, I_3^b, I_4^b, I_5^b) = 1$ at a water level E_L . The saddle height E_H is then in the interval $E_L - 1 < E_H < E_L$. To determine a more accurate value the procedure is repeated with smaller steps, say 0.1 MeV, starting from $E_L - 1$. Ever smaller steps are employed sequentially until the saddle height is determined to the desired accuracy.

The saddle-point **location** or equivalently the nuclear shape at the saddle point is determined by elaborating on this procedure. In principle, the iterations may be repeated until the uncertainty in the saddle-point energy defines a very narrow interval. The saddle is above E_L but below $E_L + \Delta E$ where ΔE is very small. Adding water starting from E_L , increasing the level to $E_L + \Delta E$, leads to an entire large region between the saddle point and the exit point becoming wet. All of these points, normally hundreds of thousands of them, have energies below E_L . A very few points may have energies in the interval E_L to $E_L + \Delta E$, this number decreasing as ΔE gets smaller. For a small enough increment, only one point will remain. This is the saddle point and its coordinates define the saddle-point shape.

This relatively simple mathematical procedure must be modified because of the finite precision of the energy values of each shape and the finite precision of numbers stored in computers. We have stored our energy matrices to a precision of 1 keV. The limited precision of numbers stored on a computer and the size of our deformation space has the consequence that there will be several points along the “rim” of the “lake” around the entry-point local minimum and along the rim of the water that has now flowed beyond the saddle that have exactly the same energy to this precision as does the saddle point. One and only one of these points is the saddle point. When we contemplate how to determine which point is the correct one, it turns out that some obvious approaches suggested by two-dimensional intuition end up being either relatively difficult to implement, or take

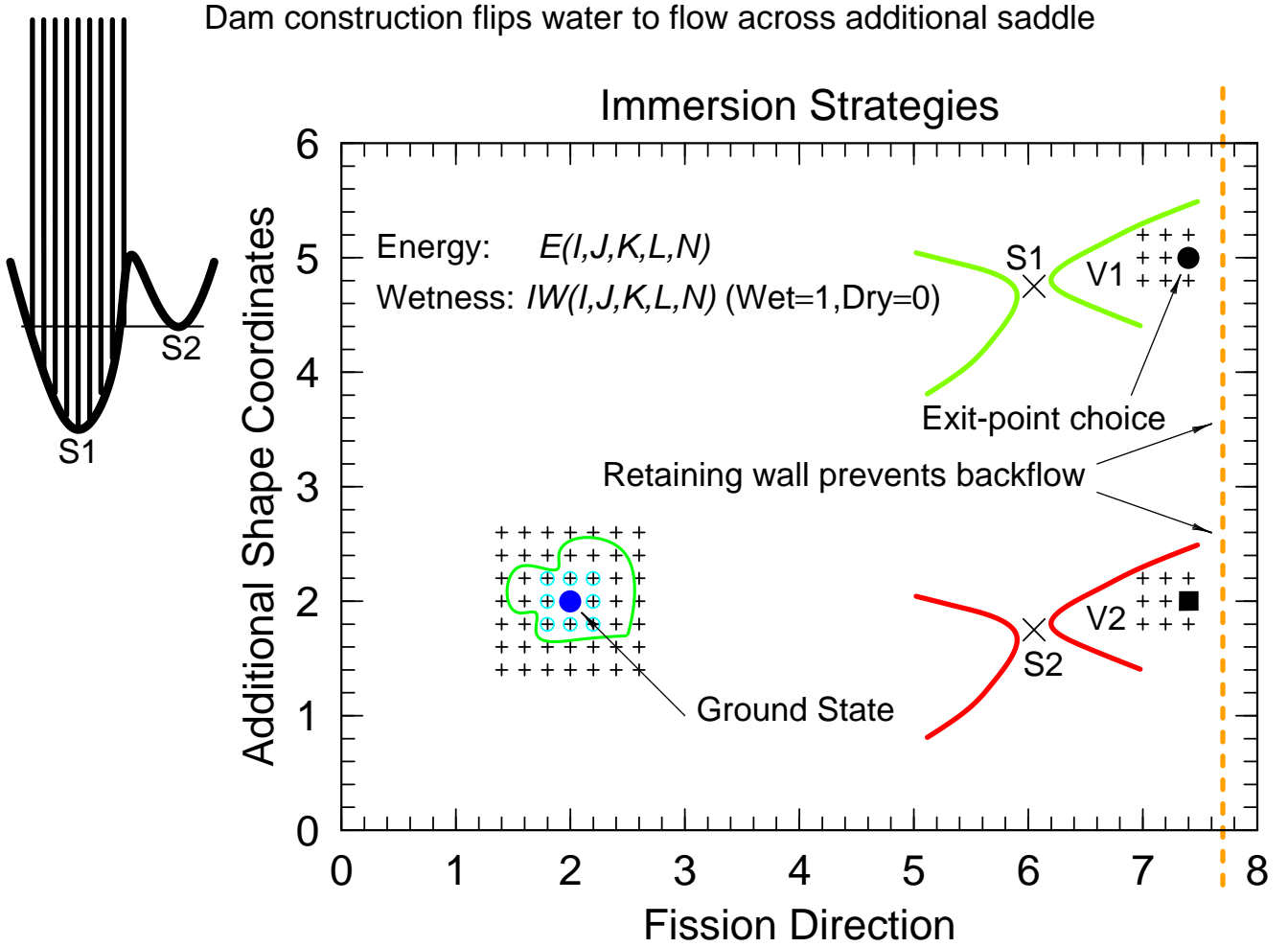


FIG. 6: (Color online) Illustration of our computer implementation of the immersion method for saddle-point identification. The figure is explained in the text.

considerably more time than the method outlined below. An example would be to evaluate the topography in the neighborhood of each point in an automated way, allowing for the restricted precision of the energy values for each point, and defining a foolproof algorithm to uniquely identify the true saddle as compared to a point lying on the side of a “hill.”.

We adopt the less obvious but efficient approach of adding to each element of E a different random number, usually $0.001 \cdot R$ MeV, where R is a random deviate uniformly distributed on the interval $[-1,1]$. Clearly this will not change the structure of the calculated potential-energy surface significantly, since the calculated energy values are associated with a higher numerical uncertainty, about 0.05 MeV. For the physical problem of saddle-point energies, such uncertainties are much less than both the uncertainty of experimental barriers, and the average deviations of the model from experiment. If the energy window ΔE is sufficiently small, usually 0.00001 MeV,

the probability that a point other than the saddle will have an energy inside the window is small. Such a small value of ΔE is more precision than is needed in determining the energy of the saddle point, but allows finding the shape of the saddle. In the rare case of two or more points still being found, the process of identifying the saddle-point energy is repeated with an independent set of random deviates added to E . The saddle point will then be identifiable as the only point common to both iterations. If several identical locations were to occur the procedure can be repeated until only one common location remains.

D. Alternative immersion strategies

An alternative approach would be to fill both the entry area (a) and exit area (b) simultaneously with water (both water levels always being the same) and store the

wet points in area (a) in a matrix IW_a and the wet points in area (b) in a matrix IW_b . If this is done “slowly,” water from the two pools will meet in one and only one point when the water level is sufficiently high, *i.e.* it reaches the saddle point. Computationally what occurs is that an identical location in IW_a and IW_b will become 1. Until the water reaches this level the locations where the matrices IW_a and IW_b are 1 are all different. This method is intuitively more appealing than the other method, but in practice more challenging to program. We are grateful to Andrius Juodagalvis for pointing out this method to us. We originally wrote a code based on filling only the ground-state area and decreasing the magnitude of the filling steps sufficiently to determine the saddle height and location. Juodagalvis subsequently wrote a code using his idea. We have checked that we obtain the same saddle heights and locations with both codes. Later Ludovic Bonneau wrote an independent code based on our original strategy and also obtains identical saddle points. We are grateful for these independent verifications of our implementation of these algorithms.

E. Additional saddle points

To find additional higher-energy saddle points between the ground state and an exit point, we “build a dam” at the lowest saddle point. We start by identifying the lowest saddle point, then raise the energy at this location to a very large value, say 1000 MeV. We again find the lowest saddle point. If the new saddle point is located adjacent to a high energy value, the water is just flowing around the partial dam at the lowest mountain pass. We raise the energy at this new location, continuing until eventually the next saddle point found is separated from the dam. This occurs when we have blocked the identified saddle region up to the elevation of the second saddle. The dam method is shown schematically as a small drawing outside the main frame in the very left part of Fig. 6. The thick wavy curve represents a cut through the potential-energy surface perpendicular to the direction of fission. When we look into the picture we look towards larger elongations in the fission direction and the minima represent the lowest and second lowest saddle points. The vertical lines represent successive dam sections that have been erected. When the bottom of the dam reaches the elevation of the second saddle point, the water flow will flip from near the dam to cross the second saddle.

What is the significance of the additional saddle? One can sometimes get guidance on this question by looking at the shape associated with the saddle. However, in most cases it is better to proceed differently and **first** identify valleys in the outer part of the fission potential-energy surface, for deformations greater than that of all saddle points. Then one can try to establish what saddle-point configurations provide entry points to the different valleys (fission modes). We outline how this is done in Sect. IV and present the actual structures we identify in

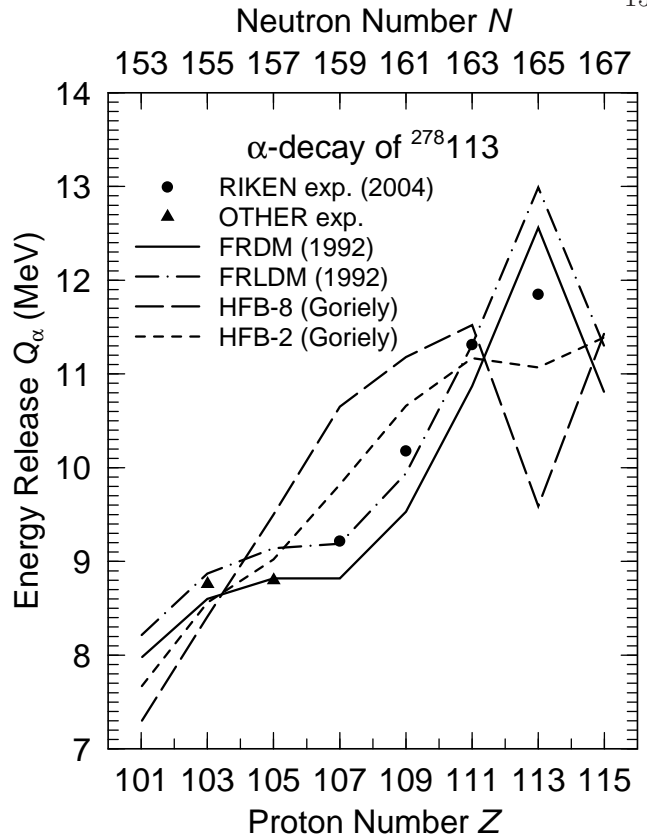


FIG. 7: Calculated and observed Q_α values in the α decay of element $^{278}_{113}$. The cusps in the FRDM and FRLDM curves occur because the calculated ground-state shape changes from deformed at $Z = 113$ to spherical at $Z = 115$. The cusp at $Z = 111$ in the HFB-8 curve occurs because the minimum identified as the ground state for $Z = 111$ has a deformation of $\beta_2 = 0.21$, while that for $Z = 113$ has $\beta_2 = 0.42$. As discussed in the text, we believe that for $^{278}_{113}$ another minimum should have been chosen as the ground state in the HFB-8 calculation.

the potential-energy surfaces of several nuclei.

F. Identifying the ground state

In our work we include essential refinements that in practice are not possible to consider in self-consistent Hartree-Fock calculations. To illustrate one issue, namely that it is non-trivial to determine which of several minima is the ground state, we show in Fig. 7 a comparison of calculated and observed Q_α values for the first $^{278}_{113}$ α -decay chain that was observed at RIKEN. The cusps at $N = 165$ in the FRDM and FRLDM models occur because of a change in ground-state deformation from deformed to spherical. Since no decay has been observed from $^{282}_{115}$ it is obviously not known at this point if the calculation is correct in this respect. But, the occurrence of such cusps in Q_α in α -decay chains that traverse magic numbers, or any substantial gap in level spectra, is well-established experimentally and is understood. In the

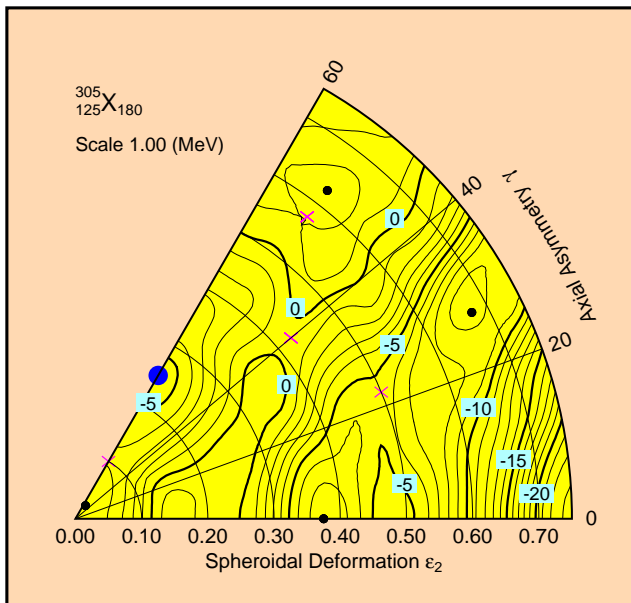


FIG. 8: (Color online) Calculated potential-energy surface for $^{305}_{125}\text{X}_{180}$. The filled dots indicate local minima, the x symbols significant saddles. The large (blue) filled dot designates the ground state. Although this minimum is not the lowest minimum it has the highest barrier with respect to fission and is therefore considered to be the ground-state minimum and is therefore considered to be the ground-state minimum, because it would be the shape most stable to fission decay.

HFB-8 calculation [55] the origin of the cusp is somewhat different. It occurs because of a deformation change from $\beta_2 = 0.21$ at $Z = 111$ to $\beta_2 = 0.42$ at $Z = 113$. However, although the more deformed minimum is the lowest found in the HFB-8 calculation, in our experience, a minimum for such a heavy nucleus with such a large deformation will have a very low barrier with respect to fission. Therefore, if it exists, a higher-energy, less deformed minimum which has a higher barrier to fission should be tabulated as the “ground state”. An example of this type of situation occurring in our calculation is illustrated in Fig. 8, which shows a contour plot of calculated potential energies for $^{305}_{125}\text{X}_{180}$. The deepest axially-symmetric minimum is at $\epsilon_2 = 0.375$ with $E \approx -7.5$ MeV. However, the saddle at $\epsilon_2 = 0.500$, $\gamma = 22.5$ indicates a barrier of only about a 2 MeV height. For this isotope, we should instead designate the minimum with the highest barrier with respect to fission as the ground state (an even more sophisticated approach would be to calculate the half-life with respect to all decay modes for all minima, but we do not take this step here). This strategy leads us to assign the minimum at $\epsilon_2 = 0.25$ and $\gamma = 60$ and $E \approx -5.5$ MeV as the ground state. Equivalently, the ground state is oblate with $\epsilon_2 = -0.25$. The saddle is at $\epsilon_2 = 0.425$ and $\gamma = 40.0$ and $E \approx -0.5$ MeV. The barrier with respect to fission is therefore about 5.0 MeV, sufficiently high to result in a fission half-life that is long enough to permit observation. We use for all nuclei in our fission studies

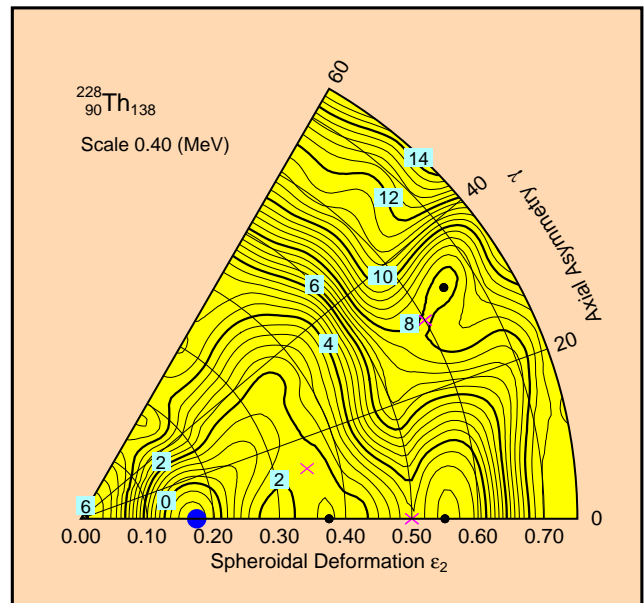


FIG. 9: (Color online) Potential energy for ^{228}Th . Beyond the ground state at $\epsilon_2 = 0.175$ there are two additional minima, one at $\epsilon_2 = 0.375$ and the other at $\epsilon_2 = 0.525$ and associated saddle points. In situations where there are several minima in addition to the ground state, it is not unambiguous which minimum and associated saddle should be compared with the “experimental” inner saddle and fission isomeric state. See text for details.

and nuclear-mass calculations, the immersion technique to assign the ground state to the correct minimum. So far HFB mass calculations do not use such techniques and might therefore choose the wrong deformation and energy for the ground state.

IV. DETAILED BARRIER STRUCTURE

To study the effect of axial asymmetry in the inner barrier region we use a three-dimensional deformation space in ϵ_2 , ϵ_4 , and γ . To visualize the results we generate contour plots for the 5254 nuclei studied, six of which are shown in Figs. 8–13. These contour maps are constructed in the following way. For each point ϵ_2 and γ we find the lowest energy obtained for the 14 ϵ_4 values calculated. The contour lines are generated from the 2D energy function defined in this way. We have emphasized in Sect. III A that in many situations such a strategy *does not* give reasonable results. One situation is when the surface contains multiple local minima versus ϵ_4 [10, 12]. However, we are using the method only for the purpose of displaying the results in a way that is relatively simple to understand. As a matter of fact, we find for the relatively modest deformations studied here that this two-dimensional potential-energy-surface approximation to the full 3D potential usually approximates the location of the saddle points and minima of

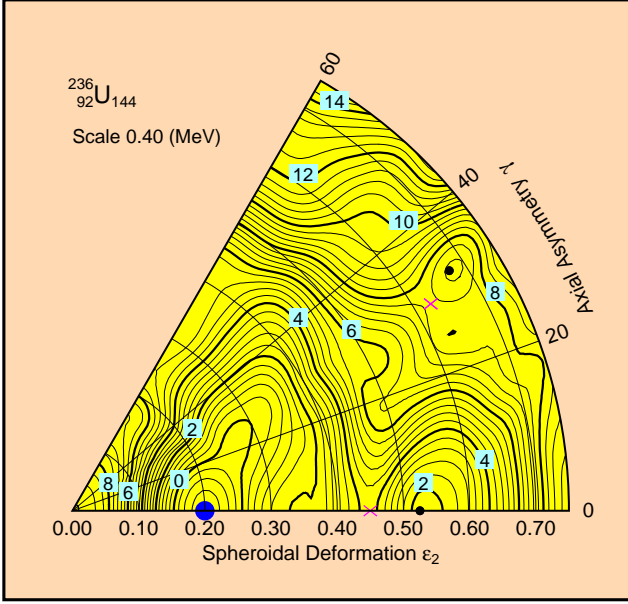


FIG. 10: (Color online) Potential energy for ^{236}U . The structure of this potential-energy surface is uncomplicated with an unambiguous fission isomeric state at $\epsilon_2 = 0.525$ and an inner saddle, which is stable with respect to axial asymmetry at $\epsilon_2 = 0.45$. The shallow local minimum at an energy around 7 MeV at $\epsilon_2 = 0.675$ and $\gamma = 32.5$ is expected to be of little consequence for the properties of this nucleus.

the full 3D space reasonably closely. However, all our barrier parameters, including those of the first barrier peaks displayed in Figs. 23–32 are obtained from a com-

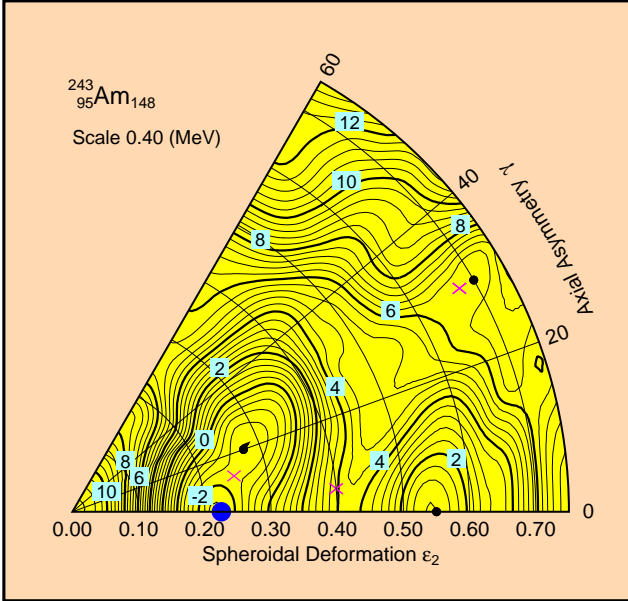


FIG. 11: (Color online) Potential energy for ^{243}Am . This isotope and some other Am isotopes have an axially asymmetric, low-lying shape isomer near the ground-state minimum.

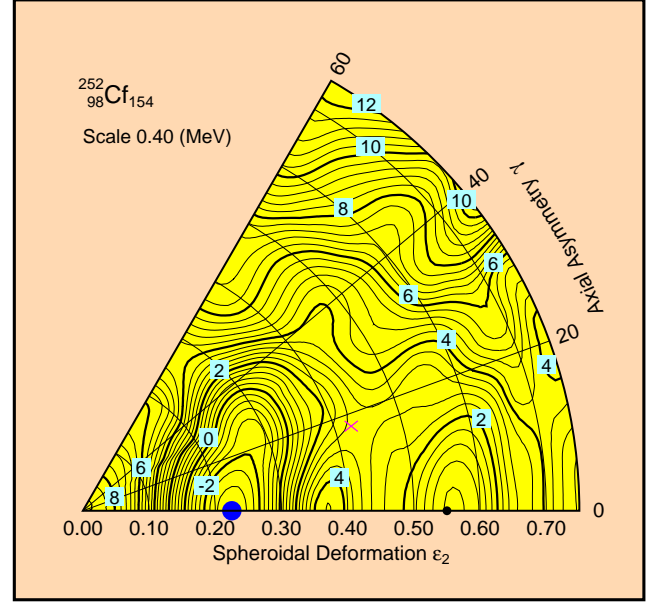


FIG. 12: (Color online) Potential energy for ^{252}Cf . The height of the inner barrier peak is lowered by about 1.4 MeV due to axial asymmetry.

plete analysis of the full 3D space. If we obtain a lower first saddle in the 5D 3QS parametrization this is used

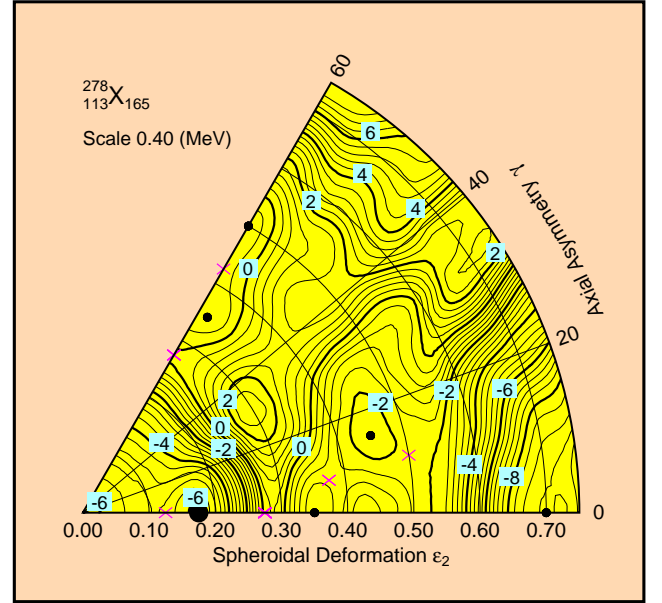


FIG. 13: (Color online) Potential energy for element $Z = 113$, currently one of the heaviest known elements; the isotope $^{278}113$ was recently observed for the first time at RIKEN [56]. The structure of this surface is interesting. This nucleus is in a transition region between deformed and spherical shapes. It has two almost equally deep minima below -6 MeV, one at $\epsilon_2 = 0.175$ and another at $\epsilon_2 = 0$, and several additional much shallower, less bound minima.

Fission-Barrier Structure for ^{238}Am

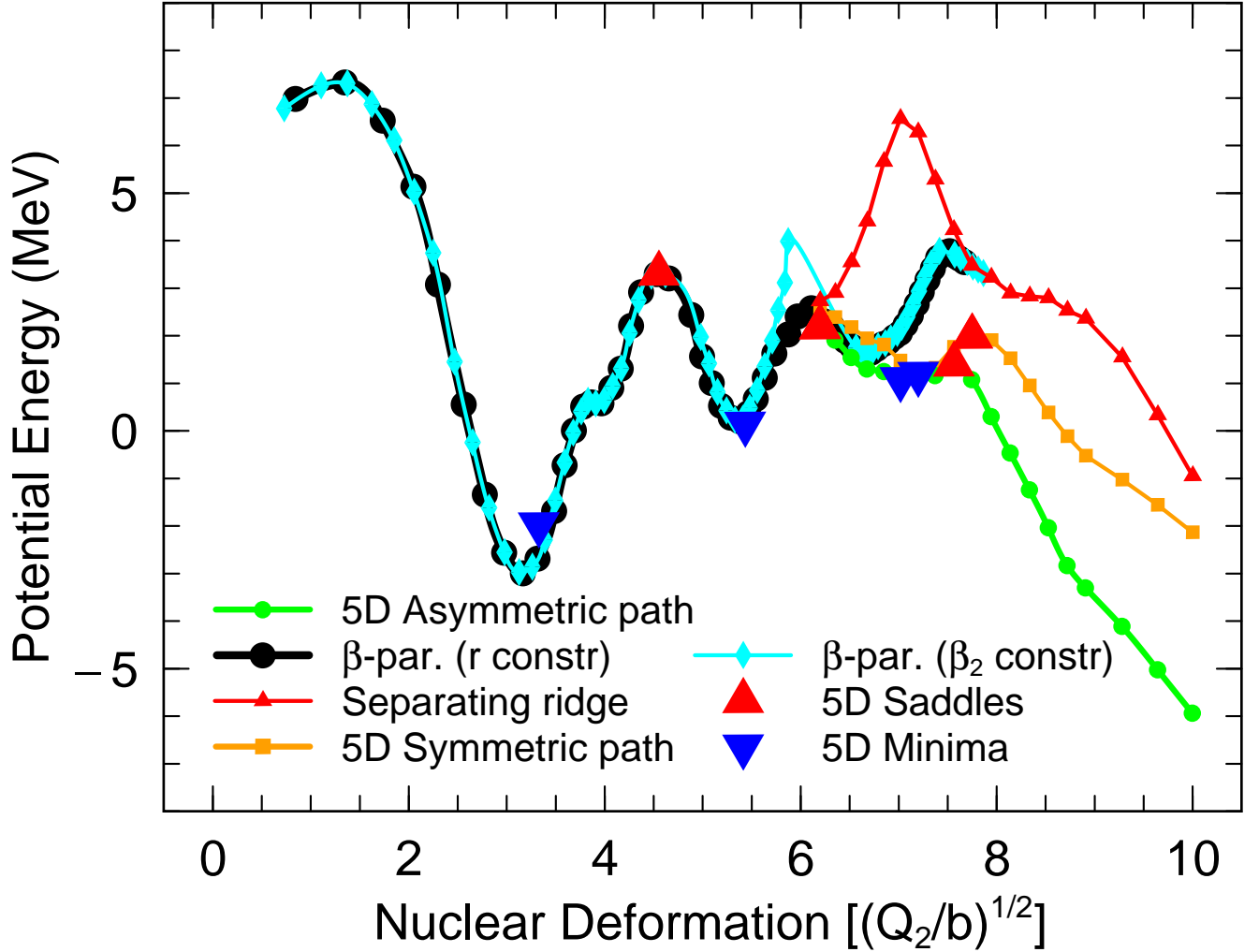


FIG. 14: (Color online) Fission-barrier structure for ^{238}Am calculated in two parametrizations. The black curve with round solid dots and the cyan curve with diamond symbols give results obtained in the constrained β parametrization with two different elongation constraints as discussed in the text; all other results are obtained in the full 5D 3QS calculation involving deformation spaces of millions of points. The dots and other symbols on the curves show the spacing of the deformation grid.

instead. The actual location and energies of the minima and saddles in the contour plots are not defined by the 2D approximate function, but instead come from the actual values determined in the full 3D calculation. The minima in the plots are shown as dots and the saddle points as \times symbols. Most potential-energy surfaces in the inner barrier region exhibit more than one minimum, namely the ground-state minimum and additional minima. For actinide nuclei near β stability there is often just one additional minimum, which is the fission-isomeric state. But a more complex structure is also possible, as our results in Fig. 13 show for one of the heaviest nuclei known $^{278}_{113}\text{X}$ [56].

The calculated 5D fission potential-energy surfaces are more complex. In Figs. 14 and 15 we present some as-

pects of our analysis of the multidimensional potential-energy surfaces in two different shape parametrizations, namely the (constrained) β parametrization and the full 5D 3QS parametrization. For each calculated 5D potential-energy surface we tabulate minima, saddles between pairs of minima, valleys as functions of Q_2 and ridges between all pairs of valleys. First we locate all minima in the potential-energy surface. We then determine by immersion the saddles between each pair of minima. We retain as significant only those minima for which all saddles are higher than 0.2 MeV relative to the higher of the two minima. Such minima are indicated by downward-pointing blue triangles and the saddles by upward-pointing red triangles. Interestingly there are only a very few minima in the calculated potential that

Fission-Barrier Structure for ^{242}Am

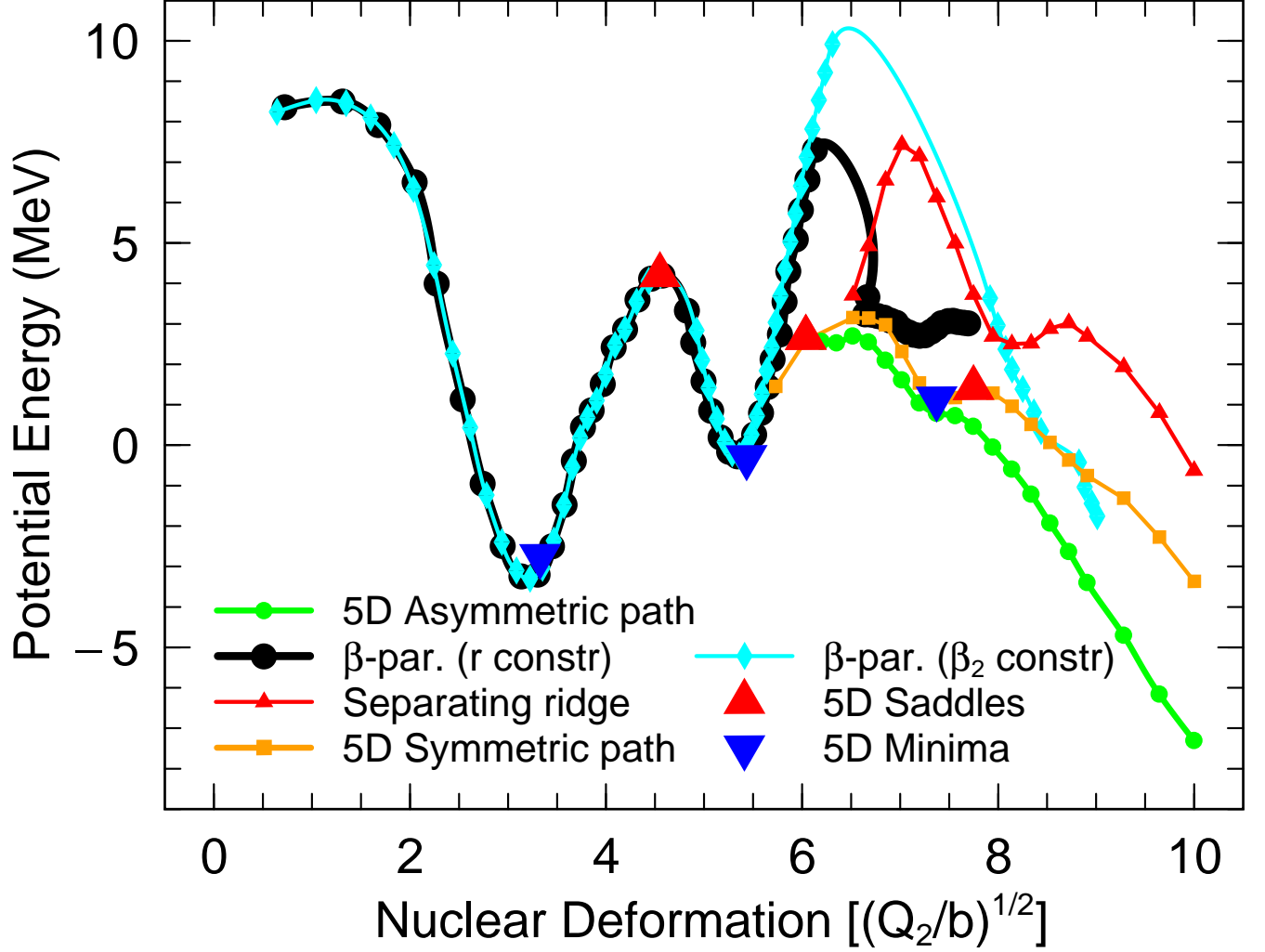


FIG. 15: (Color online) Fission-barrier structure for ^{242}Am calculated in two parametrizations. The black curve with round solid dots and the cyan curve with diamond symbols give results obtained in the constrained β parametrization with two different elongation constraints as discussed in the text; all other results are obtained in the full 5D 3QS calculation involving deformation spaces of millions of points. It is significant that the constrained calculations overshoot the true saddle by 5 MeV or more and that minor differences in the *type* of elongation constraint give rise to quite different “saddle” energies. The dots and other symbols on the curves show the spacing of the deformation grid.

are deeper than 0.2 MeV. This makes the interpretation of our results less involved than might otherwise have been the case.

Beyond the fission isomer we also look for “valleys” in the calculated potential-energy surface. We define a valley in the following manner. We fix Q_2 at one of our grid values and determine minima in the restricted 4D space (“slice”) that results. Saddles between the minima in this four-dimensional slice correspond to ridges between valleys in the full five-dimensional space. We may find several minima, but retain only minima deeper than a prescribed value. Specifically we generate 4 tables of valleys corresponding to criteria of minimum ridge heights of 2.0 MeV, 1.0 MeV, 0.5 MeV, and 0.2 MeV. Valleys are

defined as a sequence of similar minima that persist for successive Q_2 values. By similar we mean that shape parameters such as reflection asymmetry, nascent-fragment deformation and neck radius change only gradually as Q_2 increases.

For simplicity we display in Figs. 14 and 15 only two of the valleys we find, and the corresponding ridge between these. There is a good overlap in both energy and deformation between the fission-isomeric minimum obtained in the β parametrization at $Q_2/b^{1/2} \approx 5.5$ and the minimum indicated by a downward-pointing blue triangle, which is obtained in the 3QS parametrization. The saddle for ^{238}Am found beyond the isomer in the β parametrization with the “ r ” elongation constraint over-

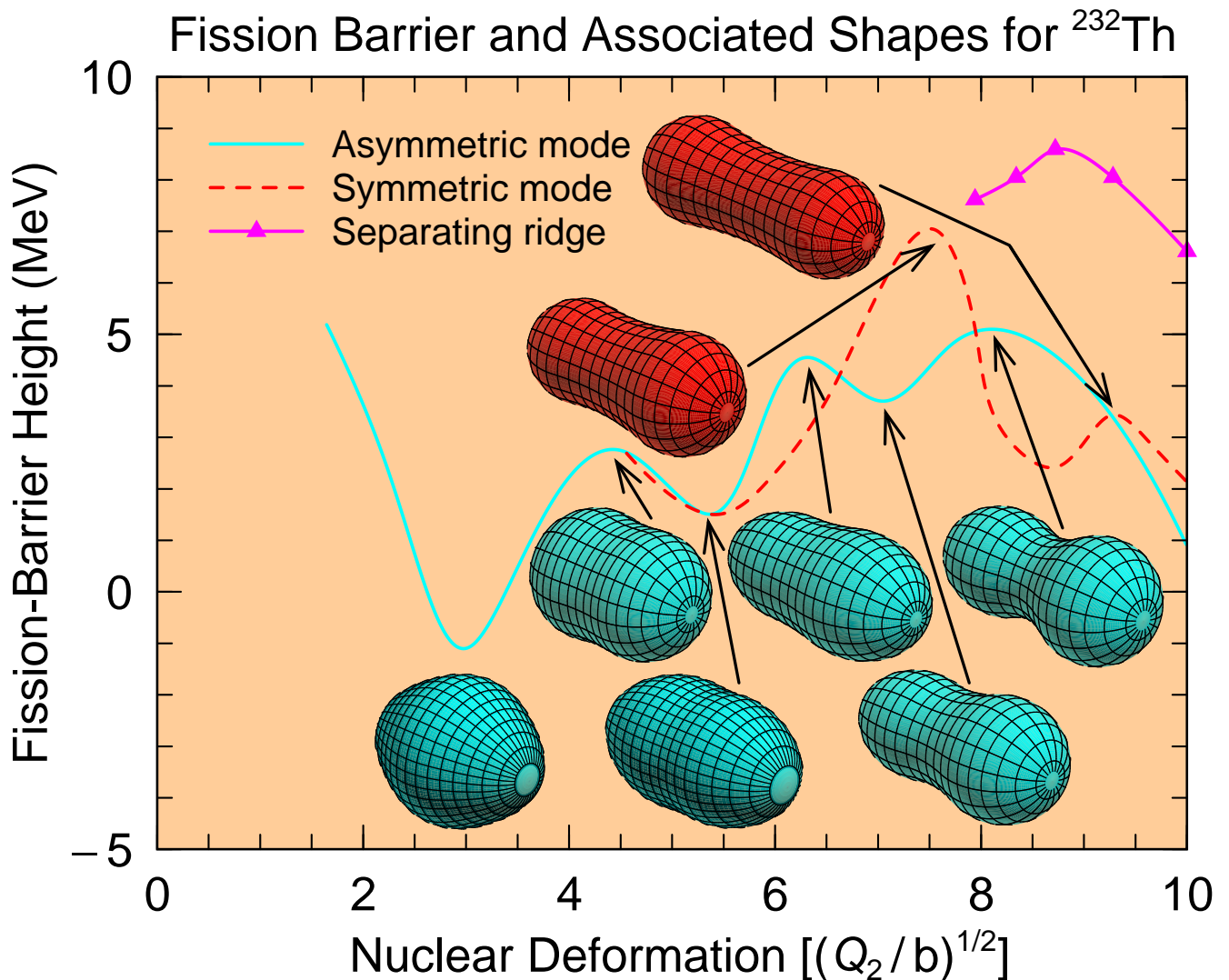


FIG. 16: (Color online) Fission barriers for ^{232}Th corresponding to different fission modes. The initial part of the barrier starting to the left of the ground state at $(Q_2/b)^{1/2} = 3.0$ extending to the fission isomeric minimum at $(Q_2/b)^{1/2} = 5.5$ is calculated in the β parametrization. Beyond the fission isomer the results are obtained in the 3QS parametrization. There are two distinct modes separated by a high ridge. Shapes associated with the barrier curves are displayed for representative points.

laps with the saddle obtained in the 3QS parametrization. This overlap between the two parametrizations in the outer saddle region is a further test of the model implementations. When instead β_2 is used as the elongation constraint the “saddle” is more than one MeV higher than the correct saddle. For ^{242}Am , the constrained calculation develops catastrophic problems near the outer barrier. The saddle in the r -constrained calculation is 4.5 MeV higher than the correct saddle, and with the β_2 constraint it is 7 MeV higher than the correct saddle. We give more details of the nature of the discrepancies in the shapes and energies found in the constrained calculation compared to the 5D one in the Appendix. This clearly demonstrates that “minimization” methods are deficient. In some cases, a reasonable saddle is found,

while for a neighboring nucleus wildly incorrect results can occur. Which will occur for a particular isotope is totally unpredictable *a priori*. It is particularly noteworthy that two reasonable choices of “elongation” constraints can give very different results. In HFB calculations it is often assumed that when elongation constraints are “cleverly” chosen problems like those we demonstrate can be avoided. Since such big differences occur for slightly different types of elongation constraint, one must conclude that it is not possible to make a “clever choice” of elongation constraints in such calculations which can be guaranteed not to lead to problems. Regardless of these difficulties, the overlaps between results from different parametrizations, when they do occur, are excellent checks of our calculations and our methods for find-

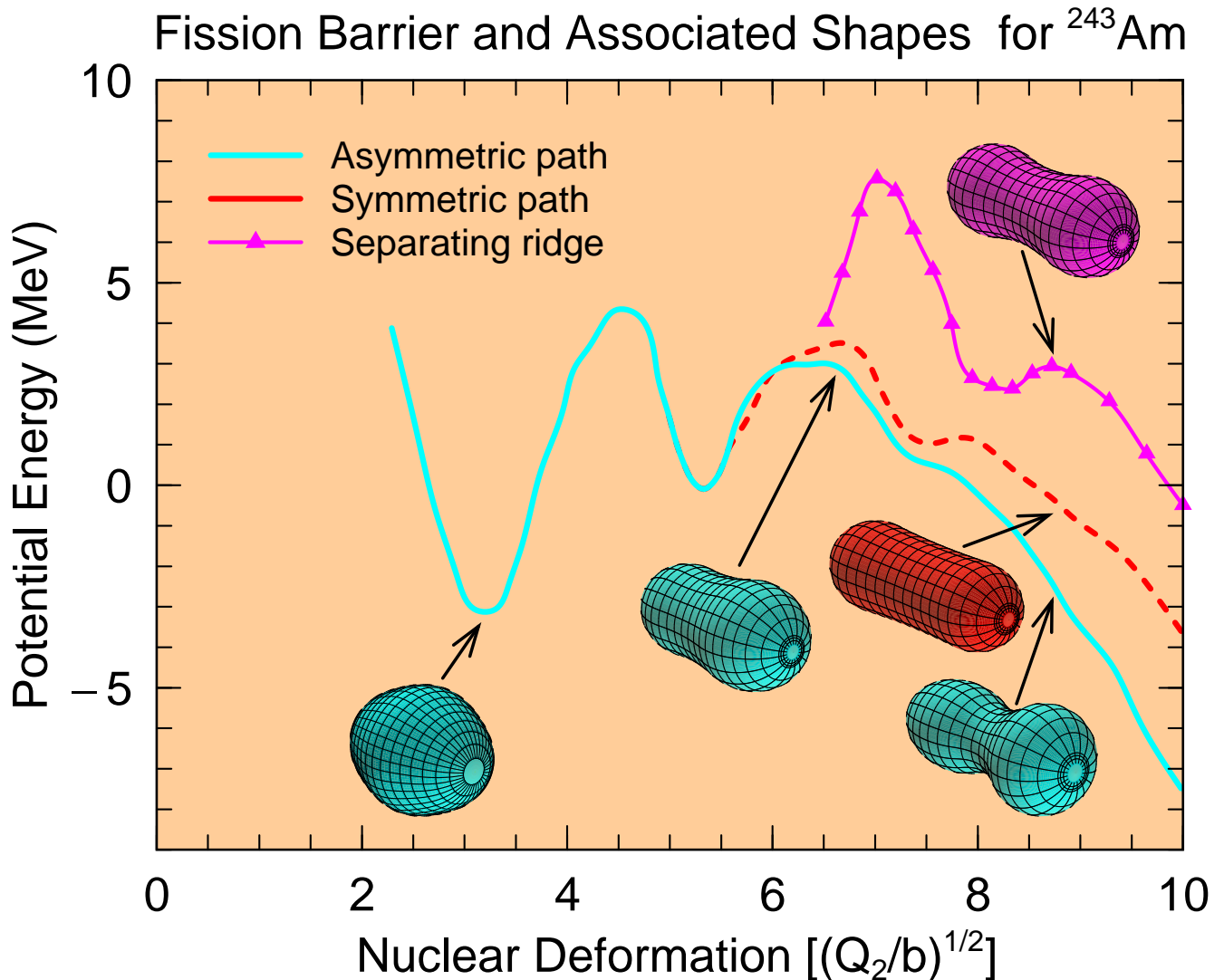


FIG. 17: (Color online) Fission barriers for ^{243}Am corresponding to different fission modes. The initial part of the barrier to the left of the ground state at $(Q_2/b)^{1/2} = 3.0$ extending to the fission isomeric minimum at $(Q_2/b)^{1/2} = 5.5$ is calculated in the β parametrization. Beyond the fission isomer the results are obtained in the 3QS parametrization. We find two distinct modes separated by a ridge. Since the ridge becomes lower than the fission saddle points at rather modest elongations, before the scission configuration is reached, one expects less well separated fission modes for this system than for ^{232}Th . The symbols on the ridge indicate the spacing along the Q_2 direction of our grid. Shapes associated with the barrier curves are displayed for representative points.

ing minima and saddles. For the ground state there is a slight non-overlap between the results obtained in the 5D 3QS parametrization and the β parametrization. But it is well-known that the 3QS parametrization cannot access some nuclear shapes that occur as ground-state shapes for some nuclei as well as can a multipole expansion [15]. This poses no difficulty, since we choose for saddle points and minima the lowest-energy result found in the three parametrizations.

In Figs. 16 and 17 we show calculated asymmetric and symmetric fission modes for ^{232}Th and ^{243}Am and nuclear shapes associated with these two modes. For ^{243}Am we also show a shape on the ridge separating these two

modes. In the lowest-energy mode, the mass-asymmetric one, shapes for both fissioning systems evolve toward separation into a large spherical “Sn-like” fragment and a smaller elongated deformed fragment. This is consistent with the long-postulated explanation for the predominantly mass-asymmetric character of fission for actinide nuclei; in fission the system strives to exploit the 10 MeV or so extra binding of spherical fragments near doubly magic ^{132}Sn . However, it is only our recent calculations based on large-dimensional deformation spaces that present a sufficiently exact and detailed theoretical description which verifies this basic mechanism in mass-asymmetric fission. Indeed, in our discovery papers [8–

10, 57, 58] we calculated the mean mass division in asymmetric fission to an average accuracy of 3 nucleons for 31 even-even fissioning systems.

The energy thresholds for the two fission modes (valleys) are different because different saddles or mountain passes provide access to the different valleys. When the ridge separating the two valleys is higher than the higher of the two saddles it is straightforward to use our immersion algorithm to establish this. And it is only in such situations that different fission modes are clearly expressed in fission-fragment data such as the variation of mass and kinetic-energy distributions with energy. However, we cannot find the higher of the two saddles by blindly applying our immersion method. Referring again to Fig. 6, there are two distinct valleys V1 and V2 reached by corresponding saddles S1 and S2. The energy at S2 is higher than that at S1. The exit point for V1 is a solid circle, while the exit point for V2 is a solid square. If we check at what level the square point becomes wet when we fill the ground-state minimum, it turns out we find the same energy as we do for V1. This is because the water will flow over S1, down V1, and then back up V2 without encountering S2. To locate the saddle S2 we need to block the waterflow down V1 to prevent backflow up V2. We do this by inserting a wall (schematically indicated by the dashed line in Fig. 6) beyond the outer saddles *and then* check when the square exit point becomes wet as the ground-state minimum is filled. The wall needs to be placed so that at the wall the ridge separating the two valleys has a higher energy than S2. In the computer program, we “build a wall” by restricting the value of Q_2 to be less than or equal to that at the wall. One could equally well define the wall by inserting large values in the energy matrix at points along the wall, as we do when building a “dam.”

A key question is how the valleys we find in the calculated potential-energy surfaces are reflected in observed fission properties. A reasonable expectation is that in systems for which valleys are persistent, that is they exist for a large range of Q_2 values and are stabilized by a high ridge, these features will leave more clear signatures on fission than will happen for systems where these features are less prominent. For example, for light actinides we find two and only two very distinct fission valleys separated by a high ridge beyond the fission-isomeric minimum. One of the valleys corresponds to shapes evolving toward separation with a compact asymmetric mass division while the other valley leads to more elongated symmetric fragments. These results correspond closely to observations of two modes of fission in the light actinide region associated with distinct saddle points of different heights, different mass divisions, and different fragment total kinetic-energy distributions in the two modes [59, 60]. A clear case is ^{232}Th in Fig. 16. In a nuclide like ^{243}Am shown in Fig. 17 the ridge separating the two modes is less prominent. The ridge becomes sufficiently low before scission that a nucleus starting in the symmetric valley at the energy corresponding to the fission

barrier could energetically cross the ridge before scission. This kind of qualitative argument does not allow a definite prediction of where the transition between the obvious bimodal fission of lighter actinides and the predominantly asymmetric fission of heavier systems will occur, but our results are definitely consistent with the fact that this transition occurs and with the observed asymmetric mass distribution for ^{243}Am .

An important task for the future is to understand how to take advantage of our significantly enhanced knowledge of the static fission potential-energy surface to improve modeling of a large number of fission properties, such as fission-fragment mass distributions, kinetic-energy distributions, neutron-emission probability as a function of fragment mass, and neutron-induced fission cross sections. The challenge is to develop global models for these quantities based on the rich structure we observe here. For a limited number of nuclei some steps in this direction have recently been taken, for example [61]. It is not obvious how to take into account the complex fission-barrier structure we now obtain in such calculations. We limit ourselves to giving below one illustration of possible impact, namely on level densities. The main scope of the paper is to present our methods and consistent results on the fission-barrier heights for a large number of heavy nuclei. This information is valuable for many considerations, for example design of experiments to reach superheavy nuclei, for electron-capture delayed fission, and how high in Z the $N = 126$ isotone might be populated.

V. FISSION-BARRIER HEIGHTS

Because the calculated potential-energy surfaces are very complex, it is not always possible to present results of our calculations in a straightforward way. Traditionally experimental data for actinide nuclei in the range $90 \leq Z \leq 99$ have been analyzed in terms of a double-humped fission barrier: a ground state, a first barrier peak, a second fission-isomeric minimum, and an outer barrier peak. We therefore in Table I represent, for 135 nuclei, our calculations in terms of such a double-humped structure for this range of proton number Z for a range of neutron numbers that corresponds to available data plus some additional proton- and neutron-rich isotopes for each element. Since most fission barriers cannot be represented in terms of a double-humped fission barrier, but do have a unique fission-barrier height, defined as the maximum height on the optimum path between the ground state and scission, we present in Table II this barrier height for 1585 heavy nuclei. Because of the finite precision of the storage of energies on the points of the coordinate grid, the energies in Tables I and II sometimes differ by 0.01 MeV.

If we were to calculate potential-energy surfaces in only one deformation space, for example the 3D space spanned

TABLE I: Calculated double-humped fission-barrier energies.

N	A	E_A (MeV)	E_2 (MeV)	E_B (MeV)	N	A	E_A (MeV)	E_2 (MeV)	E_B (MeV)	N	A	E_A (MeV)	E_2 (MeV)	E_B (MeV)
Z = 90 (Th)					Z = 93 (Np)					Z = 96 (Cm)				
135	225	4.18	4.74	7.59	141	234	3.86	3.50	4.63	153	249	6.38	3.87	6.56
136	226	3.68	4.24	7.20	142	235	4.20	3.40	4.83	154	250	5.87	3.71	6.25
137	227	3.39	3.92	6.98	143	236	4.64	3.29	4.80	155	251	5.27	3.55	6.09
138	228	2.94	3.43	6.53	144	237	4.95	3.08	4.86	156	252	4.79	3.37	5.68
139	229	2.85	3.34	6.06	145	238	5.36	3.05	5.20	Z = 97 (Bk)				
140	230	2.65	3.10	5.65	146	239	5.57	2.98	5.42	144	241	6.14	2.63	3.70
141	231	3.00	3.02	5.55	147	240	5.98	3.10	6.01	145	242	6.63	2.71	4.10
142	232	3.18	2.79	5.45	148	241	6.05	3.13	6.15	146	243	6.91	2.70	4.36
143	233	3.56	2.63	5.47	149	242	6.34	3.40	6.75	147	244	7.28	2.86	4.64
144	234	3.59	2.34	5.37	Z = 94 (Pu)					148	245	7.22	2.96	4.95
145	235	4.04	2.39	5.81	141	235	4.04	3.23	4.09	149	246	7.32	3.37	5.39
146	236	4.25	2.39	6.04	142	236	4.49	3.22	4.36	150	247	7.18	3.59	5.68
147	237	4.68	2.56	6.64	143	237	5.00	3.14	4.42	151	248	7.27	3.96	6.28
Z = 91 (Pa)					144	238	5.27	2.99	4.47	152	249	7.00	4.07	6.40
134	225	4.09	4.64	6.83	145	239	5.73	2.97	4.65	153	250	6.59	3.95	6.38
135	226	3.90	4.50	6.91	146	240	5.99	2.94	4.91	154	251	6.05	3.78	6.21
136	227	3.47	4.04	6.52	147	241	6.35	3.05	5.54	155	252	5.45	3.60	6.01
137	228	3.27	3.81	6.26	148	242	6.42	3.07	5.72	156	253	4.93	3.35	5.59
138	229	3.03	3.51	5.59	149	243	6.65	3.34	6.38	157	254	4.52	3.32	5.50
139	230	2.98	3.49	5.28	150	244	6.59	3.45	6.47	Z = 98 (Cf)				
140	231	2.93	3.25	4.99	151	245	6.67	3.77	6.93	147	245	6.98	2.59	4.16
141	232	3.26	3.20	4.97	152	246	6.34	3.86	7.07	148	246	7.15	2.70	4.34
142	233	3.54	2.99	4.99	153	247	6.05	3.84	7.12	149	247	7.35	3.16	4.88
143	234	3.81	2.91	5.14	Z = 95 (Am)					150	248	7.24	3.38	5.18
144	235	4.11	2.65	5.34	142	237	4.80	3.13	4.04	151	249	7.31	3.76	5.74
145	236	4.48	2.68	5.75	143	238	5.34	3.17	4.22	152	250	7.09	3.87	5.92
146	237	4.73	2.64	5.99	144	239	5.67	3.08	4.42	153	251	6.64	3.78	5.94
147	238	5.18	2.79	6.57	145	240	6.12	3.06	4.68	154	252	6.07	3.55	5.83
Z = 92 (U)					146	241	6.34	3.02	4.87	155	253	5.51	3.36	5.62
137	229	3.23	3.74	4.95	147	242	6.73	3.12	5.17	156	254	5.00	3.11	5.27
138	230	3.02	3.52	4.28	148	243	6.80	3.15	5.36	157	255	4.63	3.08	5.21
139	231	3.11	3.52	4.46	149	244	6.99	3.45	6.10	158	256	4.35	2.86	4.82
140	232	3.17	3.39	4.73	150	245	6.80	3.56	6.28	159	257	4.38	2.95	4.56
141	233	3.56	3.36	4.79	151	246	6.88	3.88	6.84	160	258	4.43	2.91	4.23
142	234	3.80	3.22	4.89	152	247	6.62	3.94	6.83	Z = 99 (Es)				
143	235	4.20	3.12	4.87	153	248	6.20	3.90	6.91	145	244	6.28	2.13	3.04
144	236	4.45	2.87	5.03	154	249	5.69	3.79	6.59	146	245	6.53	2.21	3.40
145	237	4.87	2.81	5.44	Z = 96 (Cm)					147	246	6.89	2.41	3.82
146	238	5.08	2.75	5.64	143	239	5.48	2.80	3.64	148	247	7.07	2.56	4.12
147	239	5.52	2.87	6.21	144	240	5.84	2.74	3.92	149	248	7.44	3.06	4.58
148	240	5.65	2.92	6.37	145	241	6.32	2.81	4.27	150	249	7.38	3.29	4.95
149	241	5.98	3.20	6.93	146	242	6.56	2.78	4.45	151	250	7.48	3.68	5.50
150	242	5.95	3.33	7.10	147	243	6.97	2.87	4.85	152	251	7.24	3.81	5.69
Z = 93 (Np)					148	244	6.92	2.94	5.07	153	252	6.79	3.70	5.70
137	230	3.14	3.65	3.81	149	245	7.12	3.33	5.58	154	253	6.22	3.45	5.47
138	231	3.01	3.47	3.81	150	246	7.01	3.50	5.87	155	254	5.67	3.26	5.36
139	232	3.16	3.57	4.14	151	247	7.11	3.82	6.49	156	255	5.04	2.99	5.01
140	233	3.40	3.49	4.36	152	248	6.80	3.95	6.65					

TABLE II: Calculated fission-barrier heights.

N	A	B_f (MeV)	N	A	B_f (MeV)	N	A	B_f (MeV)	N	A	B_f (MeV)	N	A	B_f (MeV)	N	A	B_f (MeV)
$Z = 78$ (Pt)			$Z = 79$ (Au)			$Z = 80$ (Hg)			$Z = 82$ (Pb)			$Z = 83$ (Bi)			$Z = 84$ (Po)		
93	171	11.36	108	187	15.33	123	203	25.55	94	176	7.58	106	189	8.60	121	205	18.08
94	172	11.73	109	188	16.01	124	204	26.11	95	177	7.74	107	190	9.15	122	206	19.02
95	173	12.23	110	189	16.57	125	205	27.09	96	178	7.99	108	191	9.45	123	207	20.01
96	174	12.39	111	190	17.16	126	206	27.21	97	179	8.15	109	192	9.99	124	208	20.81
97	175	12.52	112	191	17.99	127	207	26.10	98	180	8.47	110	193	10.59	125	209	22.24
98	176	12.38	113	192	18.87	128	208	25.51	99	181	8.48	111	194	11.14	126	210	22.14
99	177	12.48	114	193	19.26	129	209	24.37	100	182	8.62	112	195	11.79	127	211	21.33
100	178	12.82	115	194	19.96	130	210	23.32	101	183	8.65	113	196	12.31	128	212	20.27
101	179	13.34	116	195	20.54	131	211	22.17	102	184	8.92	114	197	13.29	129	213	18.99
102	180	13.78	117	196	21.47	132	212	21.27	103	185	9.12	115	198	14.23	130	214	17.76
103	181	14.43	118	197	22.31	$Z = 81$ (Tl)		104	186	9.61	116	199	15.22	131	215	16.47	
104	182	14.90	119	198	23.16	92	173	9.11	105	187	9.83	117	200	16.18	132	216	15.42
105	183	15.46	120	199	23.97	93	174	8.96	106	188	10.32	118	201	16.99	133	217	14.56
106	184	16.09	121	200	25.07	94	175	9.13	107	189	10.63	119	202	17.90	134	218	13.85
107	185	16.66	122	201	25.78	95	176	9.19	108	190	11.18	120	203	18.71	135	219	12.93
108	186	17.06	123	202	26.53	96	177	9.04	109	191	11.68	121	204	19.59	136	220	12.47
109	187	17.59	124	203	27.01	97	178	9.01	110	192	12.85	122	205	20.47	$Z = 85$ (At)		
110	188	17.75	125	204	27.95	98	179	8.81	111	193	13.57	123	206	21.42	99	184	4.12
111	189	18.26	126	205	28.03	99	180	8.65	112	194	14.50	124	207	22.28	100	185	4.39
112	190	18.80	127	206	27.09	100	181	8.86	113	195	14.77	125	208	23.23	101	186	4.68
113	191	19.60	128	207	26.36	101	182	8.98	114	196	15.66	126	209	23.88	102	187	5.00
114	192	20.08	129	208	25.36	102	183	9.49	115	197	16.36	127	210	22.74	103	188	5.44
115	193	20.84	$Z = 80$ (Hg)		103	184	9.87	116	198	17.28	128	211	21.76	104	189	5.56	
116	194	21.47	91	171	10.03	104	185	10.44	117	199	18.09	129	212	20.49	105	190	5.94
117	195	22.26	92	172	9.81	105	186	10.97	118	200	18.89	130	213	19.17	106	191	6.02
118	196	23.01	93	173	9.79	106	187	11.48	119	201	19.67	131	214	17.89	107	192	6.76
119	197	23.67	94	174	9.63	107	188	12.11	120	202	20.48	132	215	16.79	108	193	7.24
120	198	24.54	95	175	9.77	108	189	12.74	121	203	20.91	133	216	16.05	109	194	7.67
121	199	25.52	96	176	9.62	109	190	13.49	122	204	21.91	134	217	15.65	110	195	7.96
122	200	26.30	97	177	9.41	110	191	14.31	123	205	23.08	135	218	15.16	111	196	8.33
123	201	27.06	98	178	9.32	111	192	15.13	124	206	23.94	$Z = 84$ (Po)			112	197	8.63
124	202	27.51	99	179	9.68	112	193	15.99	125	207	24.76	97	181	3.89	113	198	9.10
125	203	28.34	100	180	9.81	113	194	16.38	126	208	24.95	98	182	4.35	114	199	9.95
126	204	28.50	101	181	10.27	114	195	17.08	127	209	23.97	99	183	4.89	115	200	10.80
127	205	27.64	102	182	10.85	115	196	18.04	128	210	22.91	100	184	5.49	116	201	11.73
128	206	26.98	103	183	11.32	116	197	18.85	129	211	21.88	101	185	5.93	117	202	12.66
129	207	25.77	104	184	11.92	117	198	19.73	130	212	20.77	102	186	6.35	118	203	13.70
130	208	24.77	105	185	12.43	118	199	20.63	131	213	19.87	103	187	6.64	119	204	14.72
$Z = 79$ (Au)			106	186	12.99	119	200	21.66	132	214	19.13	104	188	6.92	120	205	15.41
92	171	10.83	107	187	13.50	120	201	22.23	133	215	18.43	105	189	7.27	121	206	16.63
93	172	10.94	108	188	13.98	121	202	23.29	134	216	17.95	106	190	7.55	122	207	17.46
94	173	10.94	109	189	14.52	122	203	24.04	135	217	17.48	107	191	7.89	123	208	18.31
95	174	10.64	110	190	15.22	123	204	24.80	136	218	16.83	108	192	8.25	124	209	19.10
96	175	11.00	111	191	16.02	124	205	25.49	$Z = 83$ (Bi)			109	193	8.66	125	210	19.99
97	176	11.28	112	192	16.75	125	206	26.38	95	178	5.33	110	194	9.46	126	211	20.27
98	177	11.07	113	193	17.56	126	207	26.50	96	179	5.40	111	195	9.59	127	212	19.37
99	178	11.23	114	194	18.10	127	208	25.55	97	180	5.69	112	196	10.29	128	213	18.56
100	179	11.36	115	195	18.79	128	209	24.72	98	181	5.73	113	197	10.66	129	214	17.35
101	180	11.83	116	196	19.65	129	210	23.55	99	182	6.40	114	198	11.52	130	215	16.03
102	181	12.28	117	197	20.48	130	211	22.42	100	183	6.53	115	199	12.37	131	216	14.99
103	182	12.76	118	198	21.45	131	212	21.58	101	184	7.16	116	200	13.31	132	217	14.16
104	183	13.20	119	199	22.24	132	213	20.79	102	185	7.38	117	201	14.18	133	218	13.31
105	184	13.84	120	200	23.23	133	214	19.97	103	186	7.75	118	202	15.14	134	219	12.46
106	185	14.31	121	201	24.05	$Z = 82$ (Pb)		104	187	7.75	119	203	16.15	135	220	12.12	
107	186	15.03	122	202	24.79	93	175	7.62	105	188	8.14	120	204	17.02	136	221	11.75

TABLE II: Calculated fission-barrier heights.

N	A	B_f (MeV)															
Z = 85 (At)			Z = 87 (Fr)			Z = 88 (Ra)			Z = 89 (Ac)			Z = 90 (Th)			Z = 91 (Pa)		
137	222	11.64	105	192	4.43	115	203	6.89	126	215	13.36	138	228	6.52	150	241	7.43
138	223	11.13	106	193	4.38	116	204	7.49	127	216	12.19	139	229	6.06	151	242	7.87
139	224	11.03	107	194	4.35	117	205	8.51	128	217	11.08	140	230	5.66	Z = 92 (U)		
Z = 86 (Rn)			108	195	4.48	118	206	9.75	129	218	10.40	141	231	5.55	111	203	1.21
100	186	4.19	109	196	4.58	119	207	10.82	130	219	10.03	142	232	5.44	112	204	1.14
101	187	4.43	110	197	5.18	120	208	11.70	131	220	9.71	143	233	5.47	113	205	1.74
102	188	4.45	111	198	5.82	121	209	12.54	132	221	9.34	144	234	5.38	114	206	2.27
103	189	4.62	112	199	6.39	122	210	13.26	133	222	9.13	145	235	5.80	115	207	3.24
104	190	4.54	113	200	7.10	123	211	14.00	134	223	8.69	146	236	6.04	116	208	3.84
105	191	4.49	114	201	7.62	124	212	14.40	135	224	8.50	147	237	6.64	117	209	4.59
106	192	4.63	115	202	8.33	125	213	15.11	136	225	8.05	148	238	6.84	118	210	5.44
107	193	5.02	116	203	8.92	126	214	14.94	137	226	7.71	149	239	7.35	119	211	6.51
108	194	5.43	117	204	9.64	127	215	13.93	138	227	7.53	150	240	7.53	120	212	7.18
109	195	6.05	118	205	10.94	128	216	13.01	139	228	7.24	Z = 91 (Pa)			121	213	7.85
110	196	6.41	119	206	11.98	129	217	11.80	140	229	6.68	109	200	2.18	122	214	8.30
111	197	6.83	120	207	12.85	130	218	11.25	141	230	6.49	110	201	2.08	123	215	8.82
112	198	7.40	121	208	13.71	131	219	10.81	142	231	6.24	111	202	2.06	124	216	9.25
113	199	8.09	122	209	14.60	132	220	10.25	143	232	6.19	112	203	2.08	125	217	9.78
114	200	8.61	123	210	15.40	133	221	10.03	144	233	6.08	113	204	2.64	126	218	9.67
115	201	9.39	124	211	16.02	134	222	9.57	145	234	6.16	114	205	3.04	127	219	8.54
116	202	10.29	125	212	16.72	135	223	9.20	146	235	6.27	115	206	4.01	128	220	7.62
117	203	11.16	126	213	16.66	136	224	8.78	147	236	6.89	116	207	4.74	129	221	7.06
118	204	12.10	127	214	15.65	137	225	8.40	148	237	7.08	117	208	5.62	130	222	6.46
119	205	13.20	128	215	14.81	138	226	8.23	149	238	7.61	118	209	6.55	131	223	5.87
120	206	14.20	129	216	13.46	139	227	8.02	Z = 90 (Th)			119	210	7.44	132	224	5.65
121	207	15.14	130	217	12.74	140	228	7.61	108	198	2.53	120	211	8.19	133	225	5.81
122	208	15.94	131	218	12.40	141	229	7.31	109	199	2.77	121	212	8.97	134	226	5.59
123	209	16.75	132	219	11.57	142	230	7.04	110	200	2.69	122	213	9.33	135	227	5.48
124	210	17.61	133	220	11.33	143	231	7.01	111	201	2.89	123	214	9.97	136	228	5.13
125	211	18.47	134	221	10.81	144	232	6.94	112	202	2.86	124	215	10.35	137	229	4.94
126	212	18.63	135	222	10.47	145	233	6.97	113	203	3.61	125	216	10.93	138	230	4.28
127	213	17.65	136	223	10.02	146	234	6.90	114	204	3.85	126	217	10.81	139	231	4.46
128	214	16.69	137	224	9.64	147	235	7.16	115	205	4.79	127	218	9.68	140	232	4.72
129	215	15.45	138	225	9.22	148	236	7.33	116	206	5.44	128	219	8.60	141	233	4.79
130	216	14.24	139	226	9.02	Z = 89 (Ac)			117	207	6.43	129	220	8.20	142	234	4.89
131	217	13.52	140	227	8.61	106	195	3.40	118	208	7.57	130	221	7.55	143	235	4.87
132	218	12.83	141	228	8.36	107	196	3.29	119	209	8.55	131	222	6.93	144	236	5.03
133	219	12.02	142	229	8.12	108	197	3.24	120	210	9.39	132	223	6.91	145	237	5.43
134	220	11.47	143	230	8.04	109	198	3.44	121	211	10.11	133	224	7.03	146	238	5.63
135	221	11.18	144	231	7.96	110	199	3.45	122	212	10.66	134	225	6.84	147	239	6.21
136	222	10.82	145	232	8.01	111	200	3.64	123	213	11.34	135	226	6.91	148	240	6.38
137	223	10.57	146	233	7.92	112	201	4.05	124	214	11.68	136	227	6.51	149	241	6.93
138	224	10.30	147	234	8.09	113	202	4.81	125	215	12.34	137	228	6.26	150	242	7.10
139	225	9.72	Z = 88 (Ra)			114	203	5.19	126	216	12.17	138	229	5.59	151	243	7.50
140	226	9.45	104	192	3.92	115	204	5.72	127	217	11.02	139	230	5.28	152	244	7.46
141	227	9.26	105	193	3.77	116	205	6.49	128	218	9.99	140	231	4.99	153	245	7.39
142	228	9.04	106	194	3.76	117	206	7.42	129	219	9.17	141	232	4.97	154	246	7.21
143	229	8.88	107	195	3.46	118	207	8.46	130	220	8.45	142	233	4.99	Z = 93 (Np)		
144	230	8.81	108	196	3.72	119	208	9.50	131	221	8.27	143	234	5.13	113	206	1.16
145	231	8.81	109	197	4.12	120	209	10.58	132	222	7.99	144	235	5.33	114	207	1.66
146	232	8.82	110	198	3.99	121	210	11.31	133	223	8.20	145	236	5.76	115	208	2.52
Z = 87 (Fr)			111	199	4.63	122	211	12.03	134	224	7.85	146	237	5.99	116	209	3.05
102	189	4.24	112	200	5.12	123	212	12.65	135	225	7.59	147	238	6.57	117	210	3.72
103	190	4.44	113	201	5.85	124	213	12.99	136	226	7.20	148	239	6.72	118	211	4.49
104	191	4.33	114	202	6.26	125	214	13.52	137	227	6.98	149	240	7.27	119	212	5.21

TABLE II: Calculated fission-barrier heights.

N	A	B_f (MeV)	N	A	B_f (MeV)												
Z = 93 (Np)			Z = 94 (Pu)			Z = 95 (Am)			Z = 97 (Bk)			Z = 98 (Cf)			Z = 99 (Es)		
120	213	6.09	135	229	2.95	149	244	6.99	127	224	3.98	145	243	6.55	161	260	4.64
121	214	6.67	136	230	3.07	150	245	6.80	128	225	3.44	146	244	6.69	Z = 100 (Fm)		
122	215	7.00	137	231	3.05	151	246	6.88	129	226	2.84	147	245	6.99	126	226	2.84
123	216	7.52	138	232	3.23	152	247	6.83	130	227	2.17	148	246	7.16	127	227	2.08
124	217	7.83	139	233	3.50	153	248	6.91	131	228	2.17	149	247	7.35	128	228	0.80
125	218	8.28	140	234	3.83	154	249	6.59	132	229	1.93	150	248	7.24	129	229	0.90
126	219	8.26	141	235	4.09	155	250	6.37	133	230	1.72	151	249	7.31	130	230	0.79
127	220	7.32	142	236	4.49	Z = 96 (Cm)			134	231	1.64	152	250	7.09	131	231	0.85
128	221	6.47	143	237	5.00	119	215	3.04	135	232	1.81	153	251	6.64	132	232	1.25
129	222	6.01	144	238	5.26	120	216	3.31	136	233	1.94	154	252	6.07	133	233	1.39
130	223	5.28	145	239	5.74	121	217	3.78	137	234	2.27	155	253	5.62	134	234	1.46
131	224	4.96	146	240	5.98	122	218	4.09	138	235	2.71	156	254	5.27	135	235	1.56
132	225	4.43	147	241	6.35	123	219	4.59	139	236	3.37	157	255	5.21	136	236	1.87
133	226	4.17	148	242	6.41	124	220	4.99	140	237	3.99	158	256	4.82	137	237	2.39
134	227	3.78	149	243	6.66	125	221	5.62	141	238	4.55	159	257	4.56	138	238	2.88
135	228	3.70	150	244	6.59	126	222	5.64	142	239	5.16	160	258	4.43	139	239	3.49
136	229	3.81	151	245	6.93	127	223	4.85	143	240	5.76	161	259	4.57	140	240	4.14
137	230	3.81	152	246	7.07	128	224	4.16	144	241	6.14	162	260	4.64	141	241	4.50
138	231	3.81	153	247	7.12	129	225	3.69	145	242	6.63	Z = 99 (Es)			142	242	4.88
139	232	4.14	154	248	6.80	130	226	3.02	146	243	6.91	125	224	2.29	143	243	5.29
140	233	4.37	155	249	6.59	131	227	2.68	147	244	7.28	126	225	2.51	144	244	5.57
141	234	4.63	156	250	6.17	132	228	2.11	148	245	7.22	127	226	1.80	145	245	5.94
142	235	4.83	Z = 95 (Am)			133	229	1.99	149	246	7.32	128	227	0.98	146	246	6.13
143	236	4.81	117	212	2.40	134	230	1.87	150	247	7.18	129	228	1.01	147	247	6.48
144	237	4.94	118	213	3.13	135	231	2.00	151	248	7.27	130	229	0.70	148	248	6.73
145	238	5.36	119	214	3.57	136	232	2.10	152	249	7.00	131	230	1.30	149	249	7.12
146	239	5.57	120	215	4.03	137	233	2.24	153	250	6.59	132	231	1.30	150	250	7.22
147	240	6.01	121	216	4.56	138	234	2.61	154	251	6.21	133	232	1.44	151	251	7.38
148	241	6.15	122	217	4.81	139	235	3.23	155	252	6.01	134	233	1.46	152	252	7.16
149	242	6.76	123	218	5.32	140	236	3.81	156	253	5.59	135	234	1.56	153	253	6.74
150	243	6.87	124	219	5.60	141	237	4.34	157	254	5.50	136	235	1.83	154	254	6.24
151	244	7.35	125	220	6.19	142	238	4.92	158	255	5.10	137	236	2.38	155	255	5.72
152	245	7.27	126	221	6.23	143	239	5.48	Z = 98 (Cf)			138	237	2.96	156	256	5.11
153	246	7.39	127	222	5.46	144	240	5.85	123	221	3.09	139	238	3.59	157	257	4.75
Z = 94 (Pu)			128	223	4.74	145	241	6.32	124	222	3.39	140	239	4.32	158	258	4.52
115	209	1.72	129	224	4.33	146	242	6.56	125	223	3.89	141	240	4.95	159	259	4.54
116	210	2.25	130	225	3.80	147	243	6.97	126	224	4.04	142	241	5.32	160	260	4.62
117	211	3.05	131	226	3.61	148	244	6.92	127	225	3.41	143	242	5.70	161	261	4.68
118	212	3.59	132	227	2.91	149	245	7.13	128	226	2.65	144	243	5.98	162	262	4.82
119	213	4.39	133	228	2.71	150	246	7.02	129	227	1.99	145	244	6.28	163	263	4.75
120	214	5.09	134	229	2.50	151	247	7.11	130	228	1.39	146	245	6.53	164	264	4.49
121	215	5.70	135	230	2.46	152	248	6.80	131	229	1.58	147	246	6.90	165	265	4.23
122	216	6.01	136	231	2.51	153	249	6.56	132	230	1.58	148	247	7.07	166	266	3.94
123	217	6.45	137	232	2.65	154	250	6.25	133	231	1.67	149	248	7.44	Z = 101 (Md)		
124	218	6.78	138	233	2.79	155	251	6.09	134	232	1.57	150	249	7.38	128	229	0.70
125	219	7.28	139	234	3.27	156	252	5.68	135	233	1.50	151	250	7.48	129	230	0.84
126	220	7.34	140	235	3.80	157	253	5.57	136	234	1.64	152	251	7.24	130	231	0.74
127	221	6.44	141	236	4.33	158	254	5.20	137	235	2.10	153	252	6.79	131	232	0.89
128	222	5.62	142	237	4.80	Z = 97 (Bk)			138	236	2.69	154	253	6.22	132	233	1.03
129	223	5.07	143	238	5.34	121	218	2.90	139	237	3.34	155	254	5.67	133	234	1.30
130	224	4.47	144	239	5.66	122	219	3.16	140	238	4.01	156	255	5.05	134	235	1.57
131	225	4.24	145	240	6.12	123	220	3.65	141	239	4.64	157	256	5.01	135	236	1.72
132	226	3.74	146	241	6.34	124	221	3.93	142	240	5.22	158	257	4.50	136	237	2.01
133	227	3.43	147	242	6.72	125	222	4.49	143	241	5.83	159	258	4.32	137	238	2.49
134	228	2.93	148	243	6.80	126	223	4.66	144	242	6.16	160	259	4.43	138	239	2.86

TABLE II: Calculated fission-barrier heights.

N	A	B_f (MeV)															
$Z = 101$ (Md)			$Z = 102$ (No)			$Z = 104$ (Rf)			$Z = 105$ (Db)			$Z = 107$ (Bh)			$Z = 109$ (Mt)		
139	240	3.25	155	257	5.52	139	243	2.01	160	265	6.36	152	259	5.66	145	254	1.96
140	241	3.64	156	258	4.98	140	244	2.28	161	266	6.80	153	260	5.87	146	255	2.37
141	242	4.09	157	259	5.00	141	245	2.54	162	267	6.99	154	261	6.01	147	256	2.76
142	243	4.46	158	260	4.93	142	246	2.95	163	268	7.00	155	262	6.20	148	257	3.22
143	244	4.80	159	261	5.26	143	247	3.33	164	269	6.59	156	263	6.20	149	258	3.58
144	245	5.11	160	262	5.11	144	248	3.64	165	270	6.13	157	264	6.39	150	259	4.20
145	246	5.47	161	263	5.26	145	249	3.95	166	271	5.62	158	265	6.34	151	260	4.65
146	247	5.74	162	264	5.36	146	250	4.36	167	272	5.18	159	266	6.71	152	261	5.13
147	248	6.03	163	265	5.40	147	251	4.76	$Z = 106$ (Sg)			160	267	6.97	153	262	5.48
148	249	6.24	164	266	5.01	148	252	5.09	138	244	1.15	161	268	7.20	154	263	5.70
149	250	6.70	165	267	4.72	149	253	5.53	139	245	1.27	162	269	7.60	155	264	5.91
150	251	6.98	166	268	4.19	150	254	5.87	140	246	1.44	163	270	7.69	156	265	5.88
151	252	7.23	$Z = 103$ (Lr)			151	255	6.24	141	247	1.73	164	271	7.39	157	266	5.88
152	253	7.01	132	235	1.07	152	256	6.26	142	248	2.11	165	272	6.94	158	267	6.04
153	254	6.61	133	236	1.18	153	257	6.02	143	249	2.38	166	273	6.38	159	268	6.28
154	255	6.13	134	237	1.44	154	258	5.65	144	250	2.67	167	274	5.93	160	269	6.70
155	256	5.69	135	238	1.75	155	259	5.49	145	251	3.16	168	275	5.30	161	270	7.14
156	257	5.09	136	239	1.95	156	260	5.36	146	252	3.59	169	276	5.13	162	271	7.49
157	258	4.84	137	240	2.12	157	261	5.56	147	253	4.02	170	277	4.80	163	272	7.68
158	259	4.67	138	241	2.28	158	262	5.59	148	254	4.44	171	278	4.82	164	273	7.41
159	260	4.92	139	242	2.46	159	263	5.61	149	255	4.86	$Z = 108$ (Hs)			165	274	7.11
160	261	4.99	140	243	2.79	160	264	5.79	150	256	5.30	142	250	1.02	166	275	6.59
161	262	5.05	141	244	3.18	161	265	6.27	151	257	5.70	143	251	1.55	167	276	6.16
162	263	5.12	142	245	3.49	162	266	6.43	152	258	5.93	144	252	1.97	168	277	5.63
163	264	4.89	143	246	3.89	163	267	6.43	153	259	5.82	145	253	2.39	169	278	5.44
164	265	4.59	144	247	4.19	164	268	6.03	154	260	5.84	146	254	2.82	170	279	5.31
165	266	4.31	145	248	4.50	165	269	5.60	155	261	5.88	147	255	3.22	171	280	5.47
166	267	3.99	146	249	4.81	166	270	5.10	156	262	5.91	148	256	3.64	172	281	5.48
167	268	3.75	147	250	5.26	167	271	4.72	157	263	6.17	149	257	4.01	173	282	5.79
$Z = 102$ (No)			148	251	5.55	168	272	4.28	158	264	5.98	150	258	4.54	174	283	5.88
130	232	0.83	149	252	5.97	$Z = 105$ (Db)			159	265	6.27	151	259	4.93	175	284	6.30
131	233	0.75	150	253	6.27	136	241	1.31	160	266	6.69	152	260	5.39	$Z = 110$ (Ds)		
132	234	0.97	151	254	6.70	137	242	1.44	161	267	7.08	153	261	5.65	146	256	1.76
133	235	1.03	152	255	6.60	138	243	1.55	162	268	7.29	154	262	5.88	147	257	2.12
134	236	1.27	153	256	6.27	139	244	1.68	163	269	7.30	155	263	6.01	148	258	2.68
135	237	1.59	154	257	5.90	140	245	1.94	164	270	6.92	156	264	6.13	149	259	3.15
136	238	2.05	155	258	5.52	141	246	2.18	165	271	6.48	157	265	6.26	150	260	3.70
137	239	2.35	156	259	5.21	142	247	2.59	166	272	5.94	158	266	6.26	151	261	4.17
138	240	2.55	157	260	5.39	143	248	2.88	167	273	5.48	159	267	6.47	152	262	4.68
139	241	2.82	158	261	5.37	144	249	3.21	168	274	4.96	160	268	6.59	153	263	4.99
140	242	3.18	159	262	5.52	145	250	3.53	169	275	4.70	161	269	7.04	154	264	5.27
141	243	3.58	160	263	5.48	146	251	4.01	170	276	4.39	162	270	7.37	155	265	5.35
142	244	3.94	161	264	5.73	147	252	4.44	$Z = 107$ (Bh)			163	271	7.49	156	266	5.34
143	245	4.32	162	265	5.97	148	253	4.81	140	247	1.13	164	272	7.30	157	267	5.47
144	246	4.62	163	266	6.03	149	254	5.26	141	248	1.33	165	273	6.93	158	268	5.48
145	247	4.98	164	267	5.63	150	255	5.67	142	249	1.70	166	274	6.45	159	269	5.95
146	248	5.24	165	268	5.22	151	256	6.05	143	250	1.91	167	275	6.08	160	270	6.45
147	249	5.61	166	269	4.81	152	257	6.22	144	251	2.45	168	276	5.52	161	271	6.92
148	250	5.83	167	270	4.36	153	258	6.01	145	252	2.88	169	277	5.68	162	272	7.31
149	251	6.25	$Z = 104$ (Rf)			154	259	5.76	146	253	3.27	170	278	5.50	163	273	7.48
150	252	6.50	134	238	1.11	155	260	5.81	147	254	3.74	171	279	5.18	164	274	7.27
151	253	6.93	135	239	1.28	156	261	5.76	148	255	4.10	172	280	5.27	165	275	6.90
152	254	6.76	136	240	1.53	157	262	5.94	149	256	4.54	173	281	5.62	166	276	6.49
153	255	6.38	137	241	1.67	158	263	5.90	150	257	5.00	174	282	5.51	167	277	6.09
154	256	5.94	138	242	1.82	159	264	6.08	151	258	5.41	$Z = 109$ (Mt)			168	278	5.59
												144	253	1.59			

TABLE II: Calculated fission-barrier heights.

N	A	B_f (MeV)	N	A	B_f (MeV)	N	A	B_f (MeV)	N	A	B_f (MeV)	N	A	B_f (MeV)	N	A	B_f (MeV)
Z = 110 (Ds)			Z = 112 (X)			Z = 114 (X)			Z = 117 (X)			Z = 119 (X)			Z = 123 (X)		
169	279	5.64	163	275	6.71	171	285	8.82	162	279	4.83	180	299	7.72	175	298	5.84
170	280	5.69	164	276	6.59	172	286	9.00	163	280	5.21	181	300	7.37	176	299	5.60
171	281	5.86	165	277	6.36	173	287	9.23	164	281	6.01	Z = 120 (X)			177	300	5.54
172	282	5.94	166	278	5.99	174	288	9.18	165	282	6.30	167	287	6.35	178	301	5.45
173	283	6.46	167	279	5.78	175	289	9.61	166	283	6.69	168	288	6.85	179	302	5.45
174	284	6.70	168	280	5.89	176	290	9.89	167	284	7.27	169	289	7.35	180	303	5.01
175	285	7.25	169	281	6.25	177	291	9.97	168	285	7.79	170	290	7.70	181	304	4.93
176	286	7.26	170	282	6.51	178	292	9.98	169	286	8.34	171	291	8.26	182	305	4.25
177	287	7.45	171	283	6.99	Z = 115 (X)			170	287	8.70	172	292	7.36	183	306	3.69
178	288	7.45	172	284	7.41	157	272	3.08	171	288	8.57	173	293	7.44	184	307	2.95
Z = 111 (Rg)			173	285	8.00	158	273	3.47	172	289	8.61	174	294	7.57	185	308	1.94
148	259	2.32	174	286	8.24	159	274	3.86	173	290	8.90	175	295	7.71	Z = 124 (X)		
149	260	2.71	175	287	8.40	160	275	4.29	174	291	8.88	176	296	7.69	176	300	5.64
150	261	3.20	176	288	8.53	161	276	4.75	175	292	8.99	177	297	7.54	177	301	5.77
151	262	3.62	Z = 113 (X)			162	277	5.20	176	293	8.96	178	298	7.33	178	302	5.63
152	263	4.21	153	266	3.06	163	278	5.61	177	294	9.04	179	299	7.48	179	303	5.45
153	264	4.42	154	267	3.25	164	279	6.51	178	295	9.06	180	300	7.01	180	304	4.12
154	265	4.75	155	268	3.25	165	280	6.70	179	296	9.17	181	301	6.68	181	305	3.90
155	266	4.72	156	269	3.38	166	281	6.82	Z = 118 (X)			182	302	6.07	182	306	3.32
156	267	4.80	157	270	3.80	167	282	7.18	163	281	4.73	183	303	5.55	183	307	2.74
157	268	4.88	158	271	4.26	168	283	7.60	164	282	5.49	184	304	4.86	184	308	2.01
158	269	5.10	159	272	4.77	169	284	8.18	165	283	5.88	Z = 121 (X)			185	309	1.85
159	270	5.70	160	273	5.22	170	285	8.58	166	284	6.31	169	290	7.07	186	310	1.75
160	271	6.13	161	274	5.70	171	286	8.96	167	285	6.85	170	291	6.46	187	311	1.74
161	272	6.62	162	275	6.09	172	287	9.20	168	286	7.37	171	292	6.82	188	312	1.66
162	273	6.96	163	276	6.38	173	288	9.42	169	287	8.12	172	293	6.89	Z = 125 (X)		
163	274	7.20	164	277	6.31	174	289	9.29	170	288	8.32	173	294	7.31	178	303	5.64
164	275	7.01	165	278	6.06	175	290	9.53	171	289	8.85	174	295	7.03	179	304	5.45
165	276	6.71	166	279	6.12	176	291	9.60	172	290	8.39	175	296	7.19	180	305	4.93
166	277	6.37	167	280	6.41	177	292	9.76	173	291	8.41	176	297	7.16	181	306	4.44
167	278	6.06	168	281	6.66	Z = 116 (X)			174	292	8.41	177	298	7.05	182	307	3.71
168	279	5.70	169	282	6.98	159	275	3.32	175	293	8.53	178	299	6.99	183	308	1.81
169	280	6.01	170	283	7.35	160	276	3.79	176	294	8.48	179	300	7.10	184	309	1.08
170	281	6.03	171	284	7.93	161	277	4.25	177	295	8.46	180	301	6.66	185	310	1.96
171	282	6.37	172	285	8.33	162	278	4.91	178	296	8.36	181	302	6.31	186	311	1.80
172	283	6.64	173	286	8.72	163	279	5.35	179	297	8.49	182	303	5.64	187	312	1.98
173	284	7.26	174	287	8.75	164	280	6.21	180	298	8.05	183	304	5.11			
174	285	7.55	175	288	8.92	165	281	6.41	181	299	7.76	Z = 122 (X)					
175	286	8.06	Z = 114 (X)			166	282	6.66	182	300	7.15	172	294	6.32			
176	287	7.87	155	269	2.76	167	283	7.16	Z = 119 (X)			173	295	6.54			
177	288	7.90	156	270	2.97	168	284	7.65	165	284	5.51	174	296	6.53			
Z = 112 (X)			157	271	3.37	169	285	8.23	166	285	6.19	175	297	6.31			
150	262	2.65	158	272	3.79	170	286	8.47	167	286	6.70	176	298	6.33			
151	263	3.15	159	273	4.26	171	287	8.76	168	287	7.34	177	299	6.28			
152	264	3.61	160	274	4.69	172	288	9.02	169	288	7.90	178	300	6.19			
153	265	3.79	161	275	5.15	173	289	8.95	170	289	8.06	179	301	6.23			
154	266	4.05	162	276	5.53	174	290	8.94	171	290	7.62	180	302	5.60			
155	267	4.11	163	277	5.85	175	291	9.08	172	291	7.80	181	303	5.51			
156	268	4.06	164	278	6.55	176	292	9.26	173	292	8.05	182	304	4.87			
157	269	4.25	165	279	6.97	177	293	9.35	174	293	8.12	183	305	4.33			
158	270	4.72	166	280	7.13	178	294	9.46	175	294	8.29	184	306	3.62			
159	271	5.18	167	281	7.18	179	295	9.49	176	295	8.06	185	307	2.60			
160	272	5.63	168	282	7.33	180	296	9.10	177	296	8.07	186	308	1.82			
161	273	6.10	169	283	7.65	Z = 117 (X)			178	297	7.94	Z = 123 (X)					
162	274	6.51	170	284	8.09	161	278	4.14	179	298	8.10	174	297	6.09			

by ϵ_2 , ϵ_4 , and γ discussed in subsection III F, it would be straightforward to calculate the fission-barrier height. We would just subtract the energy of the minimum identified as the ground state, with zero-point energy added, from the associated saddle-point energy. However, in our current study we make calculations in several different deformation spaces and want to optimally use information from all. We also need to use computer programs to analyze the results from the different deformation spaces and determine the barrier height. There are two reasons for this. First, we need to assure that we use a consistent decision process; second, it is impractical to deal “manually” with 5254 potential-energy surfaces.

As a starting point for obtaining the barrier parameters in Table I, we tabulate a ground-state and a saddle-point energy as obtained in the 3D calculation for each nucleus. We then minimize in a 4D space, as discussed in section II A 1, all the minima we find on the oblate and prolate axes in the 3D calculation. For each nucleus we tabulate the lowest minimum. We compare the shape coordinates of the lowest 4D minimum to those of the ground-state minimum determined from the barrier condition in the 3D space. The barrier condition yields a minimum with a significantly different deformation for 270 nuclei. Only 7 of the nuclei in this group have $A \leq 292$. These are all in the group $99 \leq Z \leq 102$ and $128 \leq N \leq 130$, meaning they are very proton-rich nuclei emerging from the $N = 126$ shell having very low barriers. For all 270 nuclei in this group we use only the 3D calculation to determine the barrier height. For some superheavy nuclei in this group we obtain a substantial barrier, which would not occur if we were to analyze only axially symmetric deformation spaces. In particular for some specific cases, such as that shown in Fig. 8, choosing as the ground state the lowest-energy minimum may lead to a 1 MeV barrier, whereas the actual barrier exceeds 5 MeV.

For the remaining nuclei that are not in the group of 270, we use the 5D 3QS calculation as the starting point to determine the barrier parameters. To generate the barrier parameters for the nuclei in Table I we start by selecting from those minima having a deformation not too different from those known for fission-isomer states that minimum with the highest saddle-point energy with respect to the ground state. When more than one minimum shares this highest saddle, the lowest-energy minimum is chosen as the fission isomer. If a minimum with a corresponding Q_2 is found in the 3D calculation and/or in the constrained β -parametrization calculation, we tabulate as the energy of the second minimum the lowest of these values. We then determine in the β and 5D spaces the energy of the saddle between the second minimum and the ground state. We compare these saddle energies to the energy of the corresponding saddle in the 3D space and choose the lowest one as the energy of the first saddle. For some nuclei the axial asymmetry included in the 3D calculation leads to a considerably lower energy for the first saddle compared to the energy obtained in the axially symmetric calculations, a result which has

been known since about 1970. The outer barrier peak is determined using only the 5D calculation as the optimum saddle between the second minimum and the lowest potential-energy point at our highest Q_2 value. The energies tabulated in Table I are: E_A , the difference between the energies of the inner saddle and the ground state, E_2 , the difference between the energies of the second minimum and the ground state, and E_B , the difference between the energies of the outer saddle and the ground state. In all cases, before the difference is taken a zero-point energy taken from our FRLDM (1992) model [13] is added to the energies of the ground state and second minimum. For a few nuclei $E_{II} > E_A$. This occurs because the calculated *potential energy* at the first saddle may be only marginally higher than the calculated potential energy at the isomeric minimum. To obtain E_{II} we have added a zero-point energy to the *potential energy* at the second minimum, which sometimes has the consequence that $E_{II} > E_A$.

The highest saddle on the optimum path between the ground-state and scission configurations, which is tabulated in Table II, could in principle be obtained as just the larger of E_A and E_B determined as described above. However, since it is difficult, and sometimes impossible, to determine a “two-humped” barrier structure outside the narrow range of nuclei tabulated in Table I, we obtain the barrier heights in Table II from a somewhat different analysis. For the group of 270 nuclei discussed above we still use only the 3D calculation as the basis for calculating a barrier height. For the other nuclei we start by determining in the 5D potential-energy calculation the energy of the optimum saddle between the ground state and scission. If the deformation of that saddle is similar to the deformation of the first saddle obtained in the 3D calculation, which includes axial asymmetry, we check if the saddle energy in the 3D calculation is lower. If not, the optimum saddle energy is that found in the 5D calculation. But if the saddle in 3D space is lower (usually because of axial asymmetry), that energy is a tentative candidate for the optimum saddle energy. We then check for a second, outer saddle in the 5D calculation, which will have an energy lower than that of the original 5D inner saddle. If one does not exist, the optimum saddle will be the 3D one already tentatively identified. Otherwise, the saddle point will be the one having the higher energy. We again calculate the barrier height as the difference between the energy of the chosen saddle point and the ground-state energy found in the 4D minimization including the zero-point correction, and tabulate this value in Table II. When the identical nucleus is tabulated in Table I we expect that the higher of the E_A and E_B values in Table I will equal the value in Table II. This is indeed the case. Since different decision pathways are used to generate the numbers, this constitutes a good check on the implementation of this logic. This implementation is nontrivial due to numerous issues we do not feel are very enlightening to discuss here; one example being the occurrence of some very “pathological” potential-energy

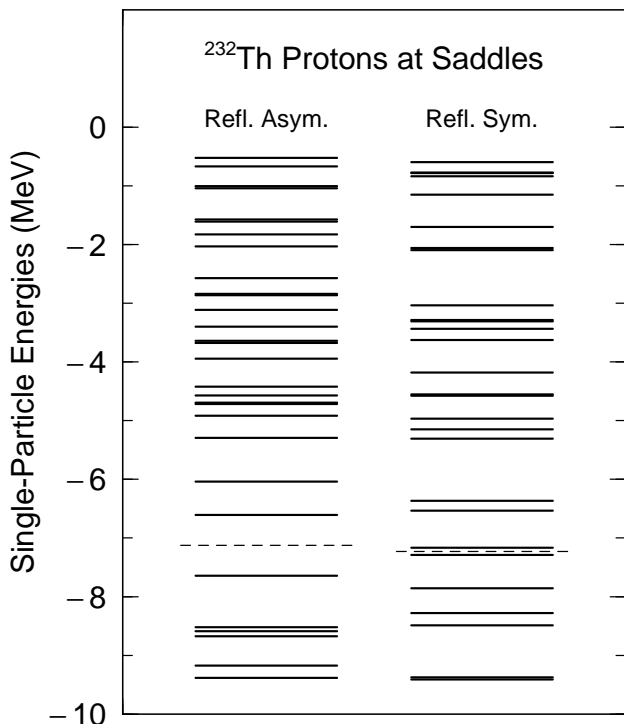


FIG. 18: Calculated proton single-particle levels for ^{232}Th at the saddles corresponding to the symmetric and asymmetric fission modes. The single-particle level density at the Fermi surface given by the dashed line is much lower at the asymmetric saddle than at the symmetric saddle. This is consistent with the shapes corresponding to these saddles. At the asymmetric saddle one of the nascent fragments is a spherical nearly doubly-magic system, *cf.* Fig. 16, resulting in a lower level density compared to the symmetric saddle.

surfaces for certain heavy nuclei.

VI. SHAPES AND LEVEL DENSITIES

Our calculations also give information about the saddle-point symmetry properties and the corresponding microscopic level structure at the saddles. Since we determine more realistic saddle-point shapes than previously, we investigate the impact of the more realistic shapes on level densities. We show in Figs. 18 and 19 calculated single-particle levels at the symmetric and asymmetric saddle points of ^{232}Th , see also Fig. 16. We find that the single-particle level density near the Fermi surface is lower at the asymmetric saddle than at the symmetric saddle. This is as expected, since the partially formed spherical Sn-like fragment at the asymmetric saddle (see Fig. 16) is responsible for this lower level density. We use the approach outlined in Sect. II C to calculate the total level density versus excitation energy for the nucleus ^{232}Th at the asymmetric and symmetric outer saddle points. The results are shown in Fig. 20 where the solid curve gives the result at the reflection asymmetric saddle and the dot-dashed curve the reflection symmetric

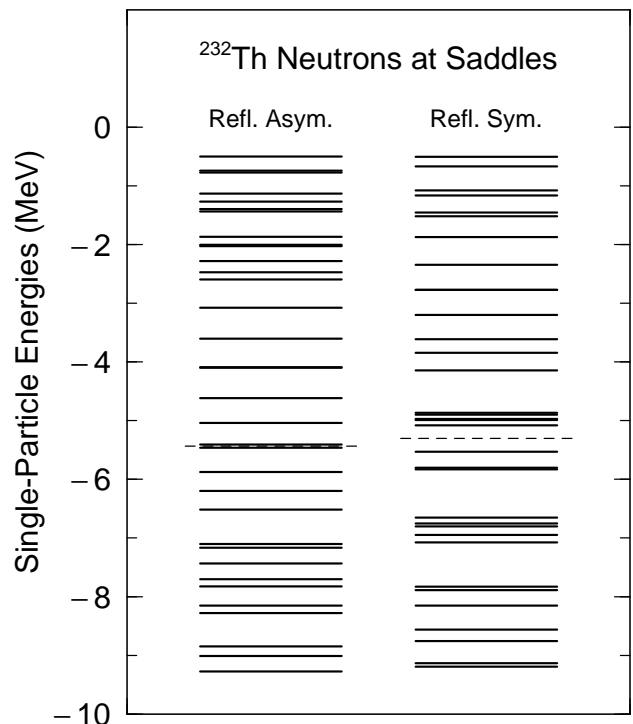


FIG. 19: Calculated neutron single-particle levels for ^{232}Th at the saddles corresponding to the symmetric and asymmetric fission modes. The single-particle level density near the Fermi surface given by the dashed line is much lower at the asymmetric saddle than at the symmetric saddle. This is consistent with the shapes corresponding to these saddles. At the asymmetric saddle one of the nascent fragments is a spherical nearly doubly-magic system, *cf.* Fig. 16, resulting in a lower level density compared to the symmetric saddle. Some of the levels near the Fermi surface at the symmetric saddle are partially overlapping so the level density is higher than might be inferred from the figure alone.

saddle, respectively. The results are given both with respect to the ground-state energy and with respect to the saddle energies. The slopes of the level densities at the two saddles differ considerably, which is a consequence of the underlying single-particle level structure close to the Fermi surface shown in Figs. 18 and 19. The level density is very sensitive to this single-particle structure since the intrinsic (non-collective) part roughly behaves as $\rho_{\text{intr}}(E) \sim \exp(2\sqrt{aE})$ where $a = \frac{\pi^2}{6}(g_p + g_n)$ is the level-density parameter and g_p and g_n are the proton and neutron single-particle level densities at the Fermi surface, respectively [39]. For this nucleus a spherical, nearly doubly-magic nascent fragment lowers the single-particle level density at the Fermi surface at the reflection asymmetric saddle giving rise to a more slowly increasing total level density. As examples of calculated total level densities for odd-even nuclei, we show three isotopes of Am (^{239}Am , ^{241}Am , and ^{243}Am) in Fig. 21 and for odd-odd nuclei we show two other isotopes of Am (^{238}Am and ^{242}Am) in Fig. 22. We determine equivalent Fermi-gas-model parameters by performing least-square fits of shifted Fermi-

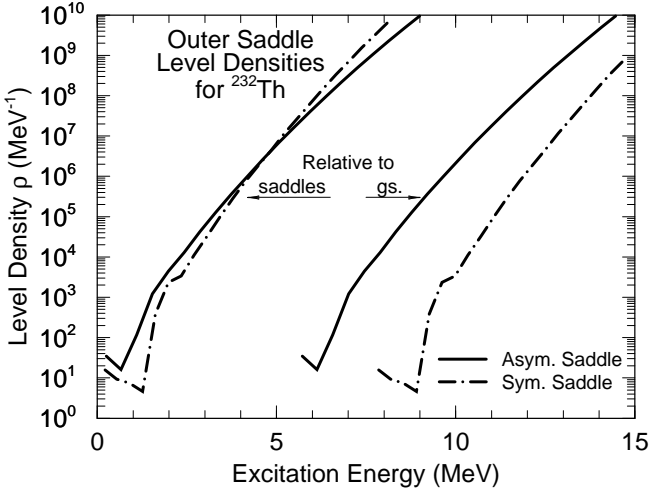


FIG. 20: Calculated total level densities at the mass-asymmetric (lower) and mass-symmetric outer saddles of ^{232}Th . The different slopes of the total level densities at the two saddles clearly reflect the difference between the intrinsic level structure at the symmetric and asymmetric fission saddle points.

gas models for level densities to our calculated densities; these are tabulated in Table III. By “Density fit” we mean a fit to the actual calculated level densities, which emphasizes the higher-energy region, while the “Log fit” is to the logarithm of the calculated densities. The latter gives roughly equal weight to all excitation energies. Noticeably different Fermi-gas parameters are obtained in the two schemes. The root cause is that the Fermi-gas expression in Eq. 25 is a poor approximation to the microscopic level-density-model results. A significant result is that there is considerable variation between systems, due to differences in the microscopic level structure at

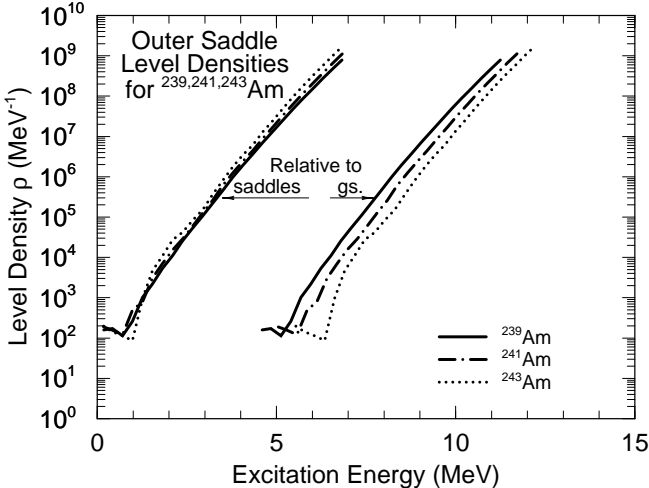


FIG. 21: Calculated total level densities at the outer saddles of ^{239}Am , ^{241}Am , and ^{243}Am . The slopes of the different total level-density curves are fairly similar. Because these systems are odd-even the level density is higher than at the ^{232}Th saddles in Fig. 20.

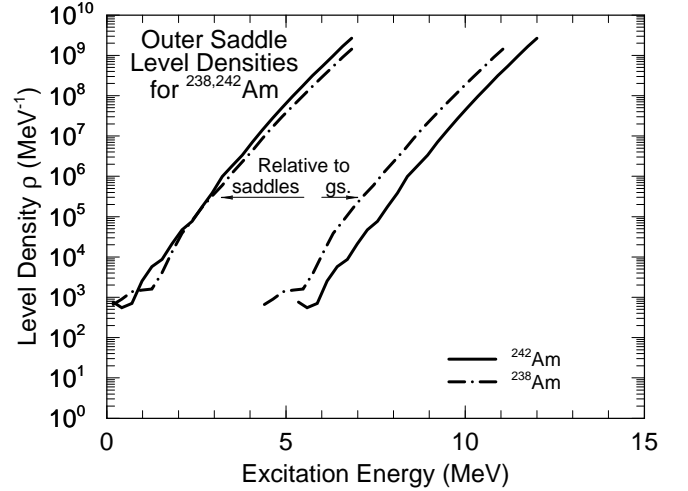


FIG. 22: Calculated total level densities at the outer saddles of ^{238}Am and ^{242}Am . The slopes of the different total level-density curves are fairly similar. Because these systems are odd-odd the level density is higher than at the ^{232}Th saddles in Fig. 20 and at the saddles of the odd-even Am systems in Fig. 21.

the saddle points. See Sect. VII E for a discussion on experimental data on level densities for the asymmetric and symmetric fission modes of ^{232}Th .

TABLE III: Fermi-gas level-density parameters determined from adjustments of parameters of the Fermi-gas model to microscopic calculations of intrinsic level densities. The numbers in parentheses are (1) for an asymmetric saddle, and (2) for a symmetric saddle. B and C refer to the second and third saddle, respectively, for a triple-humped barrier, see Fig. 14.

Nucleus		Density Fit			Log Fit	
		$Q_2^{1/2}$ (barn $^{1/2}$)	a (MeV) $^{-1}$	E_{shift} (MeV)	a (MeV) $^{-1}$	E_{shift} (MeV)
even-even systems						
^{232}Th	(1)	7.75	17.708	2.483	15.403	1.177
^{232}Th	(2)	7.56	20.538	2.492	18.963	1.898
odd-even systems						
^{239}Am	(1)	6.04	19.369	1.275	16.906	0.607
^{241}Am	(1)	6.04	19.879	1.232	19.156	0.980
^{243}Am	(1)	6.04	20.281	1.097	17.828	0.470
odd-odd systems						
^{238}Am	(1B)	6.20	19.041	0.810	19.125	0.700
^{238}Am	(1C)	7.56	17.259	0.232	17.814	0.420
^{242}Am	(1)	6.04	19.740	0.618	21.961	0.980

VII. COMPARISONS TO DATA AND OTHER MODELS

We present calculated barrier heights for 1585 nuclei. After analysis of additional calculated potential-energy surfaces we plan to present a data base of barrier heights for all nuclei between the proton and neutron drip lines from $A = 170$ to nuclei so heavy that stability with respect to fission is completely lost. This data base will provide barrier heights for more than 5000 nuclei. In this discussion we would like to investigate if our calculations can be expected to be reliable for such extrapolations. We therefore compare our results to several different types of data that are affected by fission-barrier heights. First, we compare calculated barrier heights to barrier heights deduced from experimental reaction data. It is not straightforward to compare calculated barrier parameters to experimental data. First, the experimental barrier parameters are determined from fits of models to cross-section data. The “experimental” fission-barrier heights depend strongly on model assumptions. Second, the barrier may have more than two barrier peaks and more than one fission mode; analysis in terms of a two-peaked barrier is therefore only a crude approximation. But on the other hand, analysis in terms of a more complicated structure introduces a large number of additional parameters to be fitted to data, which leads to other difficulties.

Double-humped fission-barrier parameters have only been experimentally determined for a fairly limited number of nuclei, mainly actinide nuclei. To obtain insight about the reliability of our results for larger regions of nuclei we therefore also discuss how our results compare to other types of experimental data that depend strongly on fission-barrier heights, specifically fission half-lives, and β - or electron-capture-delayed fission. We show that our results are consistent with such data. We also discuss how our results compare to other calculations, in particular HFB calculations.

A. Fission-barrier heights

In Figs. 23–32 we compare our calculated barrier parameters (solid lines) to the experimental evaluations by Madland [62] (black circles) and the RIPL-2 evaluation [44, 45] (red squares). The evaluation by Madland is based on data in Refs. [36, 63–65].

It is of interest to try to understand if the barrier calculations are reliable outside the region of nuclei to which the model parameters were adjusted. The FRLDM (2002) parameters we use here were determined in 2002 [12]. It was not reasonable to retain the FRLDM (1992) parameter set because our vastly more general deformation spaces for fission potential-energy calculations now include millions of deformation points compared to 175 deformation points for the potential energy surfaces on which the FRLDM (1992) was based; a more than 10 000

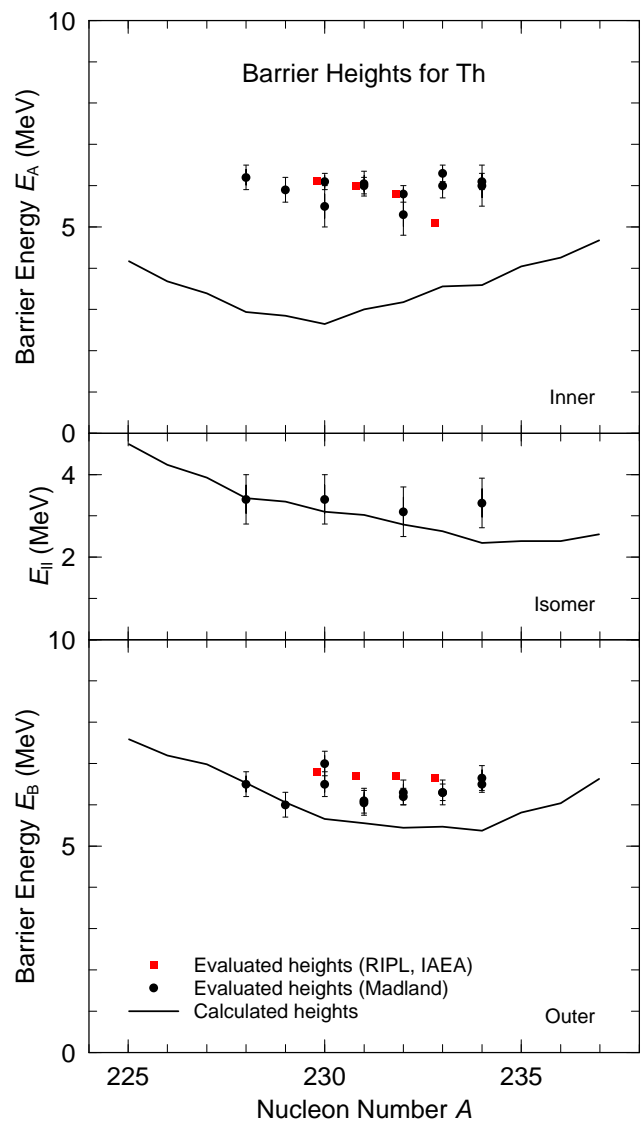


FIG. 23: (Color online) Calculated first and second saddle heights and fission-isomer energies for Th isotopes, compared to experimental data where available.

fold increase. This leads to a systematic lowering of all calculated barrier heights by up to 3 MeV. [8, 57]. The experimental mass data set [66] used in the 2002 parameter determination is identical to the set used for the 1995 mass table [13]. Thirty-one outer barrier heights were used in the fission-barrier-height data set. The rms error between barrier heights derived from experimental data is 0.999 MeV, the mass-model error for 1654 nuclei is 0.752 MeV. If we assume that the intrinsic model errors are randomly distributed, and are of the same magnitude for saddle points as for ground states, and that the saddle and ground-state errors are uncorrelated, then one expects, due to the subtraction required to extract a barrier height from the saddle-point and the ground-state energies, that the error σ_{bar} should fulfill

$$\sigma_{\text{bar}} = \sqrt{2}\sigma_{\text{mass}} \quad (26)$$

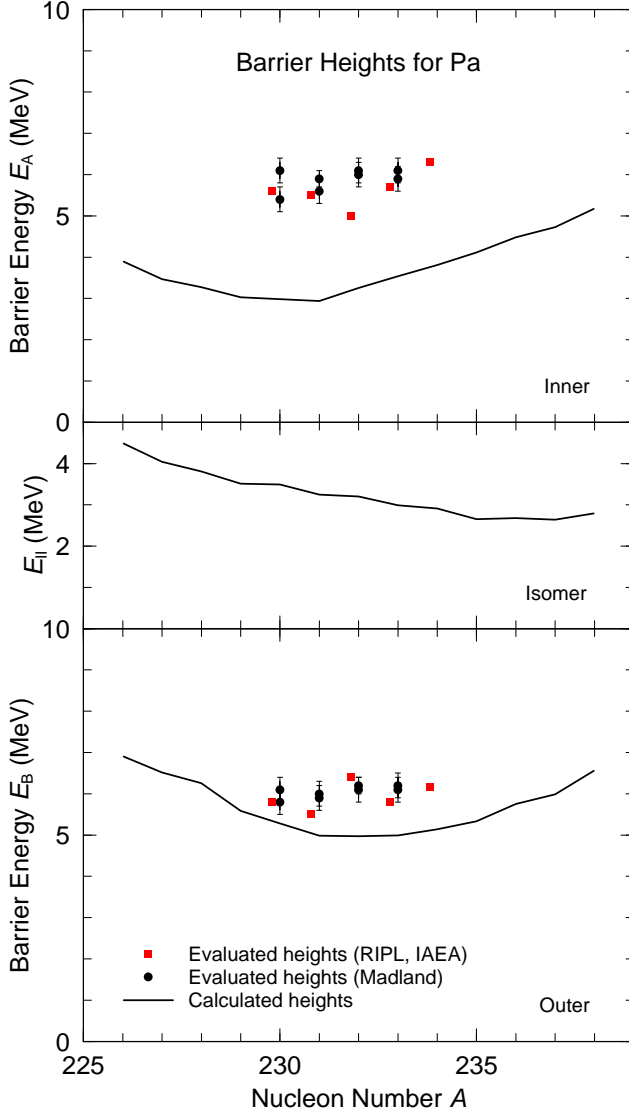


FIG. 24: (Color online) Calculated first and second saddle heights and fission-isomer energies for Pa isotopes, compared to experimental data where available.

This requirement is consistent with the error estimates in the FRLDM (2002) model, but was not for the FRLDM (1992) model, for which the estimate for σ_{bar} was about 1.4 MeV.

For light actinide nuclei we consistently obtain that the outer peak, beyond the fission isomeric minimum, is split into two about equally high peaks (denoted E_B and E_C), separated by a shallow minimum (denoted E_{III}) which is 0.5 to 1 MeV deep. It has been argued [7] that it is the inner of these peaks that should be compared to what in experimental evaluations has been tabulated as the first barrier peak. That would bring the calculated and experimental values for the height of the first barrier peak into much better agreement with each other. However, experimental (n,f) data for ^{232}Th and nearby nuclei were subsequently analyzed in terms of a three-humped barrier structure [67]. A general feature of the results of this

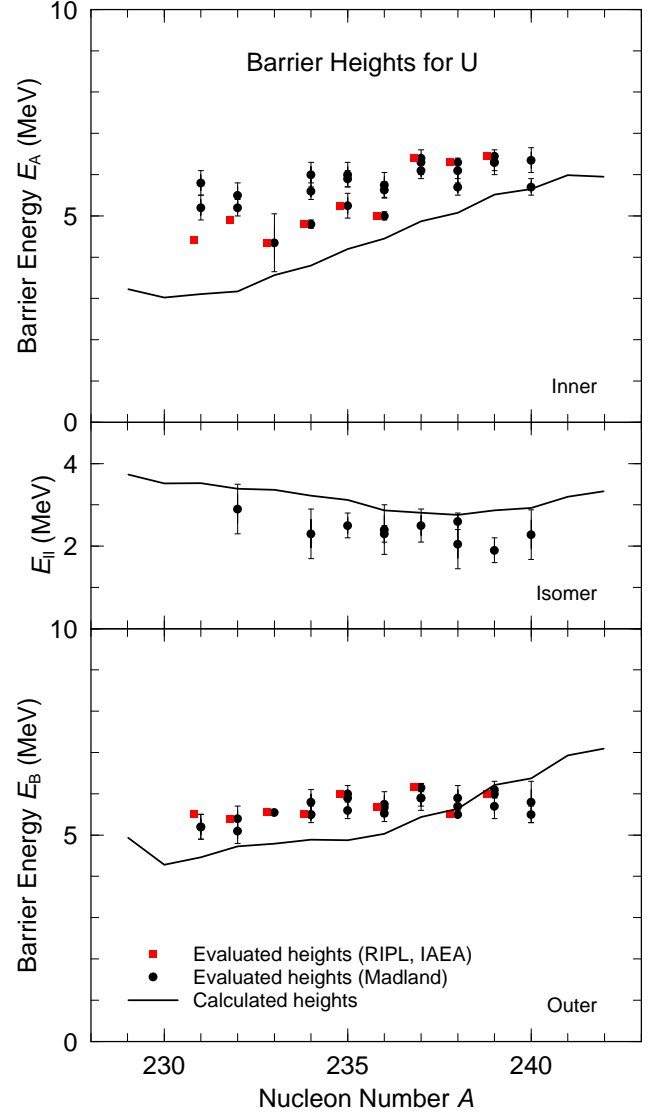


FIG. 25: (Color online) Calculated first and second saddle heights and fission-isomer energies for U isotopes, compared to experimental data where available.

analysis for ^{230}Th , ^{231}Th , ^{233}Th , and ^{237}U is that the barriers of these nuclei do exhibit a triple-humped structure. The heights of the saddles and minima depend on the K quantum number of the fission channel. For the first peak the results in MeV are 5.40–6.14, 5.11–5.50, 5.10–6.00, and 5.00–5.20, for ^{230}Th , ^{231}Th , ^{233}Th , and ^{237}U , respectively. At the lower end of the range of values these experimental values are up to one MeV lower than those given by the experimental evaluations used in Figs. 23 and 25. In the outer barrier region this experimental study deduces that the conventional outer saddle is split into two peaks by a shallow “third” minimum about 0.5 MeV deep. Each of the outer peaks is about 6 MeV high. For the lighter nuclei in this sequence it is the outer of the two peaks that is the higher by 0.5 MeV or so, for ^{237}U it is the inner of the two peaks that is the highest. For details see Ref. [67]. Our results for the outer-barrier

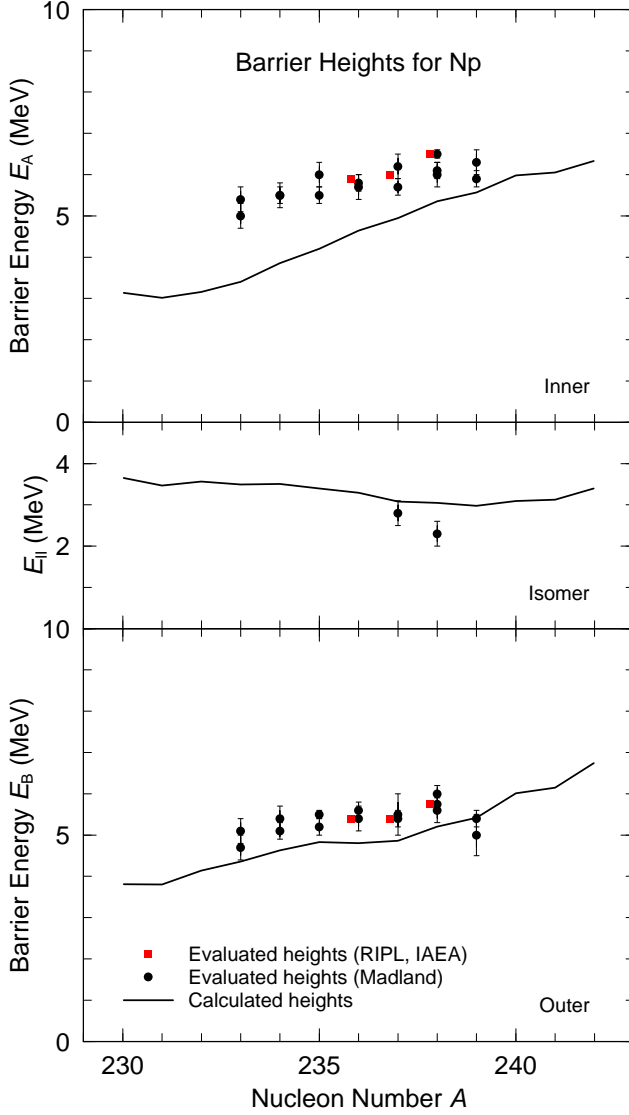


FIG. 26: (Color online) Calculated first and second saddle heights and fission-isomer energies for Np isotopes, compared to experimental data where available.

region are in very good agreement with this analysis as can be seen in Fig. 16. We also reproduce the experimentally deduced trend of the relative height of E_B and E_C with neutron number. However, our inner barrier E_A is still lower than those resulting from this refined analysis of the experimental data. Calculated first barrier peaks that are lower than values obtained from analysis of experimental data for light actinides is a well-known, still unresolved issue, and are obtained in many theoretical studies, for example in [7, 53, 68–74].

For Pu, Am, Cm, and Cf the calculated second barrier heights for neutron number N in the range 150 to 155 appear too high compared with experimental data. The lighter of the fission fragments in fission of these nuclei corresponds to a region near ^{108}Ru where we have recently shown that the ground-state mass is lowered by up to 0.7 MeV by allowing axially asymmetric shapes [75].

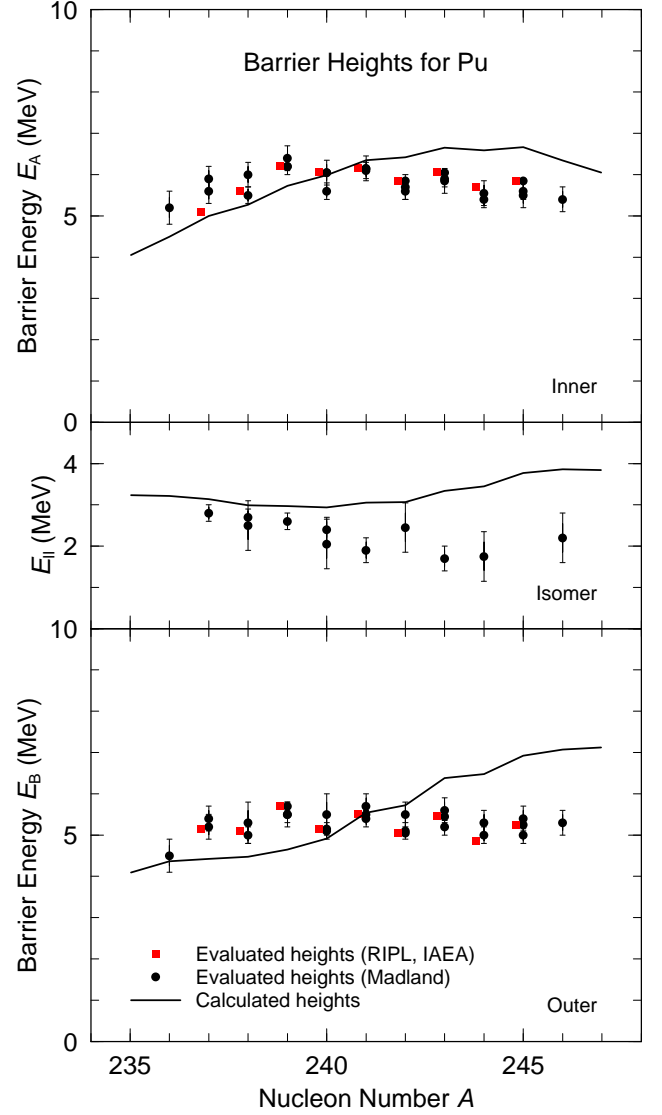


FIG. 27: (Color online) Calculated first and second saddle heights and fission-isomer energies for Pu isotopes, compared to experimental data where available.

We know that some fragment properties already begin to emerge at the outer saddle point in fission. It would be interesting to include triaxial shape degrees of freedom at the outer saddle point since the fragments are already partially formed there. This will be a formidable task since it requires that the three-quadratic-surface parametrization be extended to allow triaxial shapes, and that in order to allow different amounts of triaxiality for each nascent fragment, the dimensionality of the deformation space must increase from five to seven.

B. Other models

To gain additional insight about the reliability of our results and those of other models, we wish to compare to other efforts that study several nuclear properties

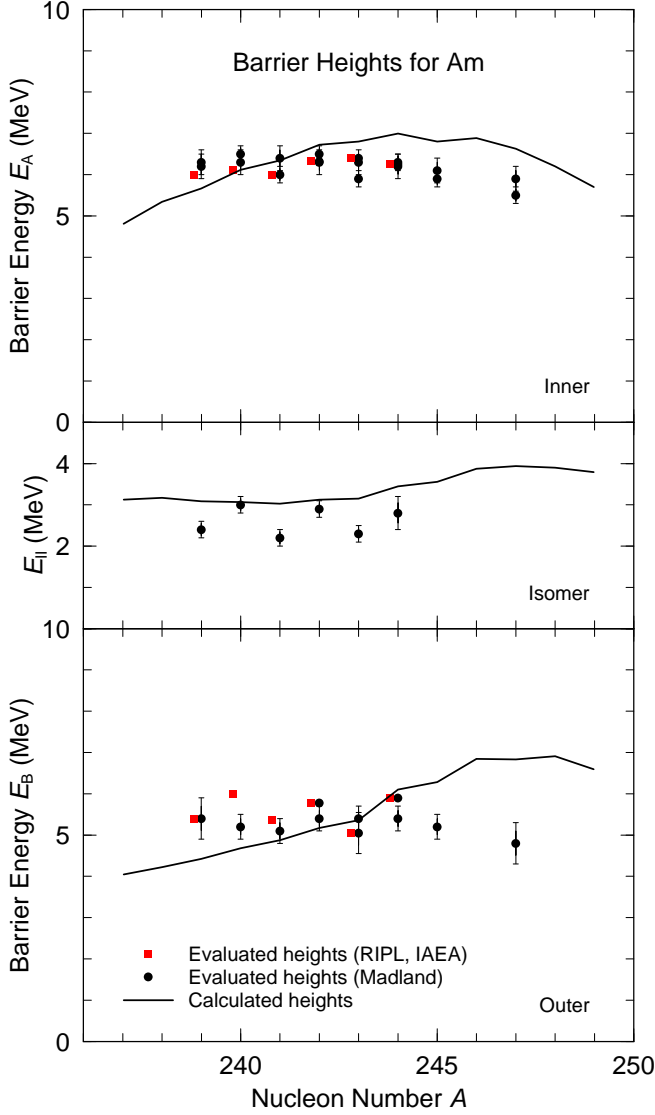


FIG. 28: (Color online) Calculated first and second saddle heights and fission-isomer energies for Am isotopes, compared to experimental data where available.

(universality) such as nuclear ground-state masses, deformations, and fission barriers for a large number of nuclei (globality). We are aware of only one other set of studies that fit into this category, namely the Brussels/Montreal HFB-1,,HFB-n (where n stands for model version and currently is about 15)[55, 76, 77]. We compare our fission-barrier results to studies based on the HFB-n framework. This work is often presented as “self-consistent,” “fundamental,” and “microscopic” and our work is referred to as “phenomenological” and this characterization is given as evidence that our work must be expected to be less reliable when used to predict properties of currently unknown nuclei. This claim is misleading. To begin with, the values of the parameters defining the effective two-body interaction used in this type of model are adjusted to nuclear properties, including masses (phenomenological). Second, in mass studies

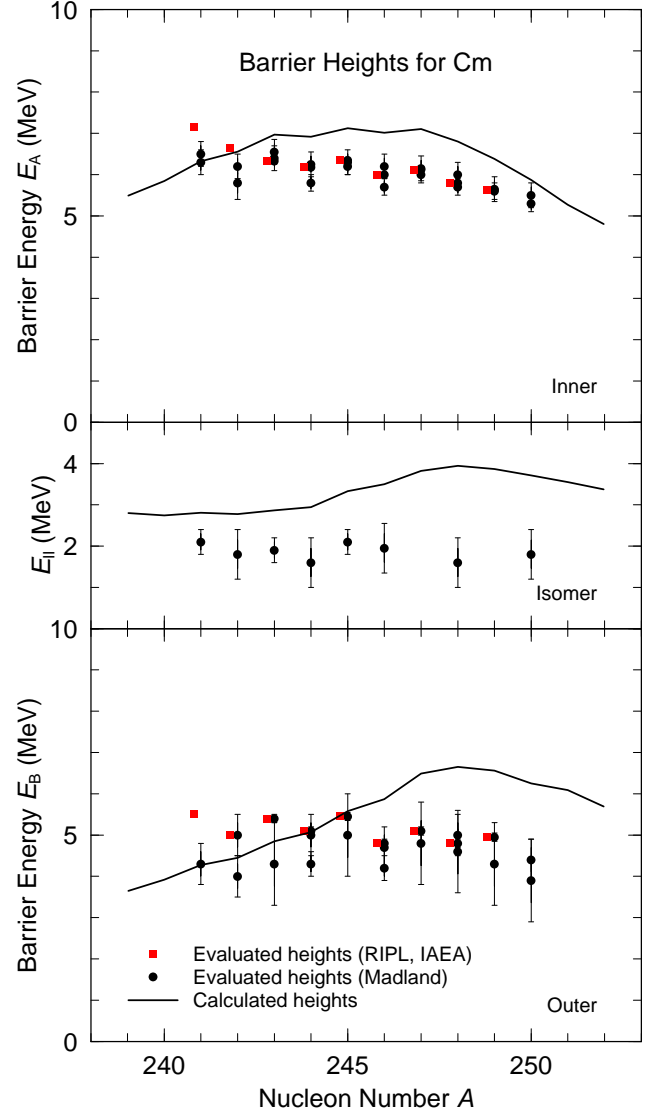


FIG. 29: (Color online) Calculated first and second saddle heights and fission-isomer energies for Cm isotopes, compared to experimental data where available.

the HFB calculations use other phenomenological terms with adjustable parameters, for example terms to describe what is referred to as the Wigner energy. Thirdly, in the latest work on barriers [77], an admittedly phenomenological “collective correction” term with three or four parameters is added. The authors of this work mention that the good reproduction of experimental barriers in this model “is entirely the result of the three extra fitting parameters provided by this term.” Therefore, the HFB work is also phenomenological, no longer self-consistent, and is actually a type of macroscopic-microscopic model. Certainly its microscopic content is higher than that in our model, with the effective volume, surface and Coulomb energies arising from the microscopically calculated densities. Both the HFB model and our model have spin-orbit effective interactions that are not derived from fundamental considerations. The form and

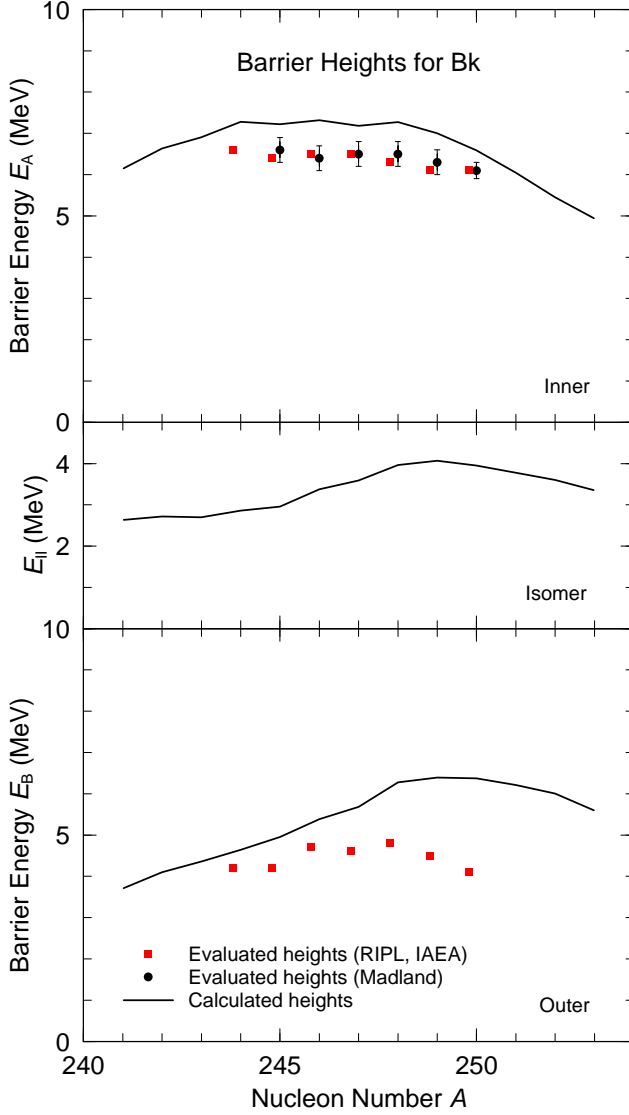


FIG. 30: (Color online) Calculated first and second saddle heights and fission-isomer energies for Bk isotopes, compared to experimental data where available.

strength of the spin-orbit term provide some of the major sources of uncertainty for any model applied to nuclei far from stability.

This being said, what are the current accomplishments of the two efforts and what kind of reliability can we expect of our fission-barrier calculations? It may seem straightforward to compare calculated barrier heights with “experimental” barrier heights. However, the experimental barrier heights are not measured as directly as nuclear masses can be measured. They are, as we have discussed, deduced from modeling measured fission cross-section excitation functions. But it is a standard comparison. Both our calculation and the HFB-14 calculation yield good agreement with data for actinides, with about a 1 MeV average error. It is difficult to evaluate the reliability of extrapolation of the models to extremely neutron-rich nuclides that are relevant for the r-process.

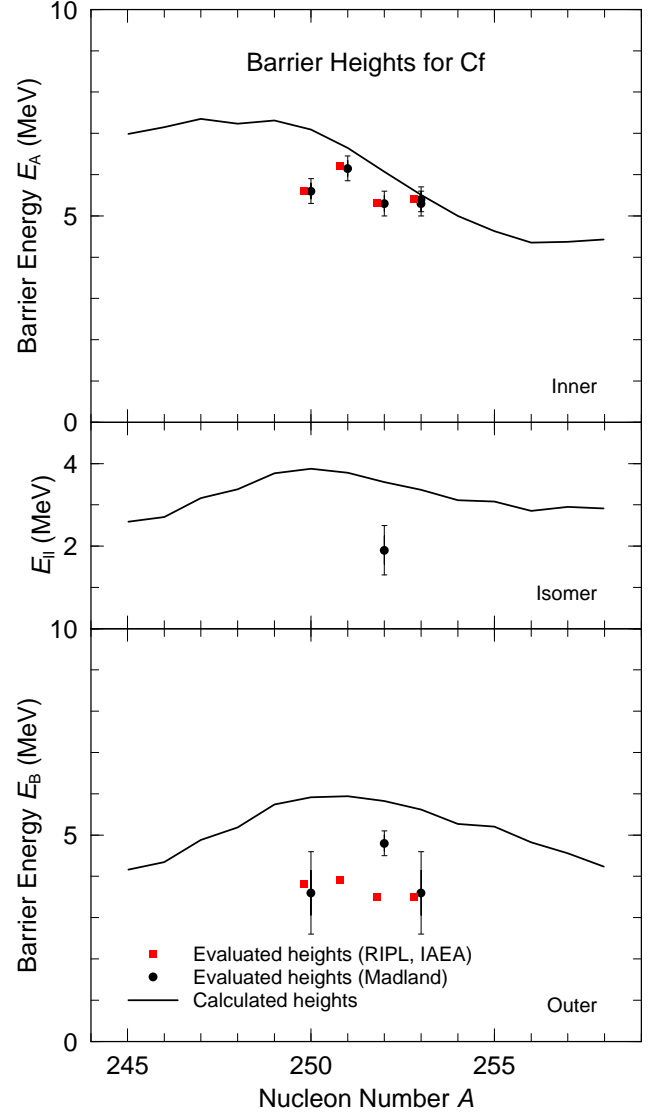


FIG. 31: (Color online) Calculated first and second saddle heights and fission-isomer energies for Cf isotopes, compared to experimental data where available.

The only direction of extrapolation directly accessible is to lower values of Z . From Fig. 5 of [77], one can infer a systematic overestimation of the barrier heights in the $Z = 80$ to 87 region. This is typical of self-consistent microscopic models, all of which have a very large effective curvature energy [78, 79], which tends to increase the energy of the more deformed saddle points characteristic of lighter nuclei. HFB-14 results for systems with $Z < 80$ are not given. Our model, on the other hand, has been compared to barriers down to $Z = 34$, with no apparent increase of average deviation for the lighter nuclei [12]. It is also possible to make indirect comparisons of calculated barrier heights with other types of data. For example, the calculated barrier heights should be sufficiently high that they are compatible with observed half-lives. In the HFB and the somewhat related ETFSI studies in the region $Z \geq 107$ [53, 55] many of the fission barriers

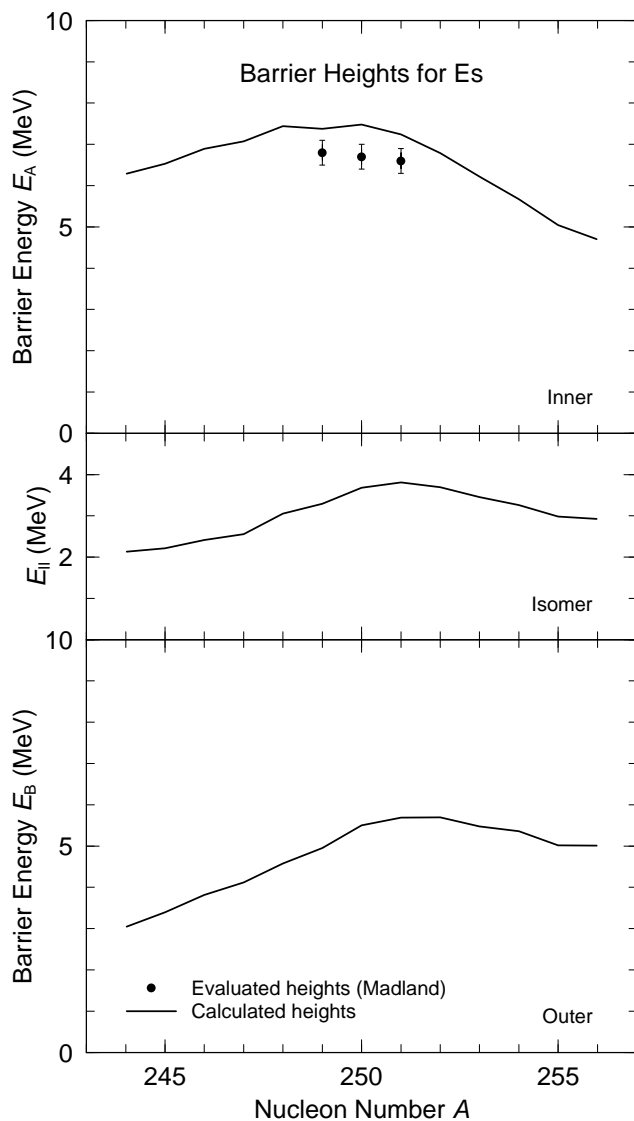


FIG. 32: Calculated first and second saddle heights and fission-isomer energies for Es isotopes, compared to experimental data where available.

for nuclei which have been observed are in the 2–3 MeV range which are too low to be compatible with observations of 100% α -decay branches with half-lives in the ms range. Another area in which our model has been shown to extrapolate well compared to HFB-n is in predicting the masses of superheavy elements, which although not yet measured, do lead to the observed α -decay Q values for the elements with $Z = 110$ to $Z = 113$. Our predictions for these elements [13, 22], which predate the measurements, give a good reproduction of the Q values for all α -decay chains which have so far been measured in this mass region; an example is shown in Fig. 7. Since barriers in the HFB model do not extrapolate as well as those in our model do either in the direction of lower Z and A , or to the superheavy region, we remain skeptical of how well it may extrapolate in the large- N direction. There is no evidence presented in [77] for the claim

TABLE IV: Fission and α -decay half-lives for selected nuclei. The experimental fission half-lives are from [81]. The calculated and experimental α half-lives are from [22] and [82], respectively. The top five entries are comparisons between calculations and experimentally available fission and α -decay half-lives for representative (and somewhat challenging) actinide nuclei. The three middle entries represent predicted stability for even-even nuclides with $N = 126$ heavier than the last observed $N = 126$ nuclide (^{218}U). The next three entries illustrate the much shorter half-lives just beyond the $N = 126$ shell in the transition region between spherical and well-deformed nuclei. The last entry is for a $Z = 112$ deformed “superheavy” nucleus.

Nuclide			$^{10}\text{Log}(T_{1/2}^f/y)$		$^{10}\text{Log}(T_{1/2}^\alpha/y)$	
Z	N	A	Calc.	Exp.	Calc.	Exp.
92	144	236	14.31	16.39	8.18	7.37
94	138	232	-1.29		-3.21	-4.19
94	146	240	9.22	11.05	4.51	3.93
100	152	252	6.06	2.09	-1.14	-2.54
100	158	258	-7.34	-10.91		
96	126	222	9.41		-4.12	
98	126	224	1.65		-4.70	
100	126	226	-3.03		-5.29	
96	128	224	-2.16		-8.35	
96	134	230	-10.76		-1.48	
98	132	230	-15.96		-4.52	
112	165	277	-5.37		-11.91	-11.11

“Model HFB-14...is well suited for a new calculation of all the barriers involved in the r-process.” We cannot claim to know how well our model extrapolates to fission barriers in the r-process region, but have at least some confidence because of the above points, and because of its good historical record of extrapolating to regions of nuclear masses that were not known when the mass tables were published[20, 80].

C. Heavy-element stability

We display 1122 of the barrier heights tabulated in Table II in terms of a contour diagram in Fig. 33. Our calculated barrier heights agree well with experimentally deduced barrier heights as we discussed above. We now discuss a number other of observed fission-related properties and how they compare to our calculations.

Heavy nuclei primarily decay by α and β -decay and by fission. We have earlier provided extensive tables of α - and β -decay half-lives [83]. The β half-lives were calculated in a microscopic model which is accurate to about a factor of three [84]. If parent and daughter masses are known the α - and β -decay half-lives can be estimated from simple Q -value systematics to within one or two orders of magnitude. However, theoretical fission half-lives are more difficult to calculate than α -decay half-lives and are subject to greater uncertainties.

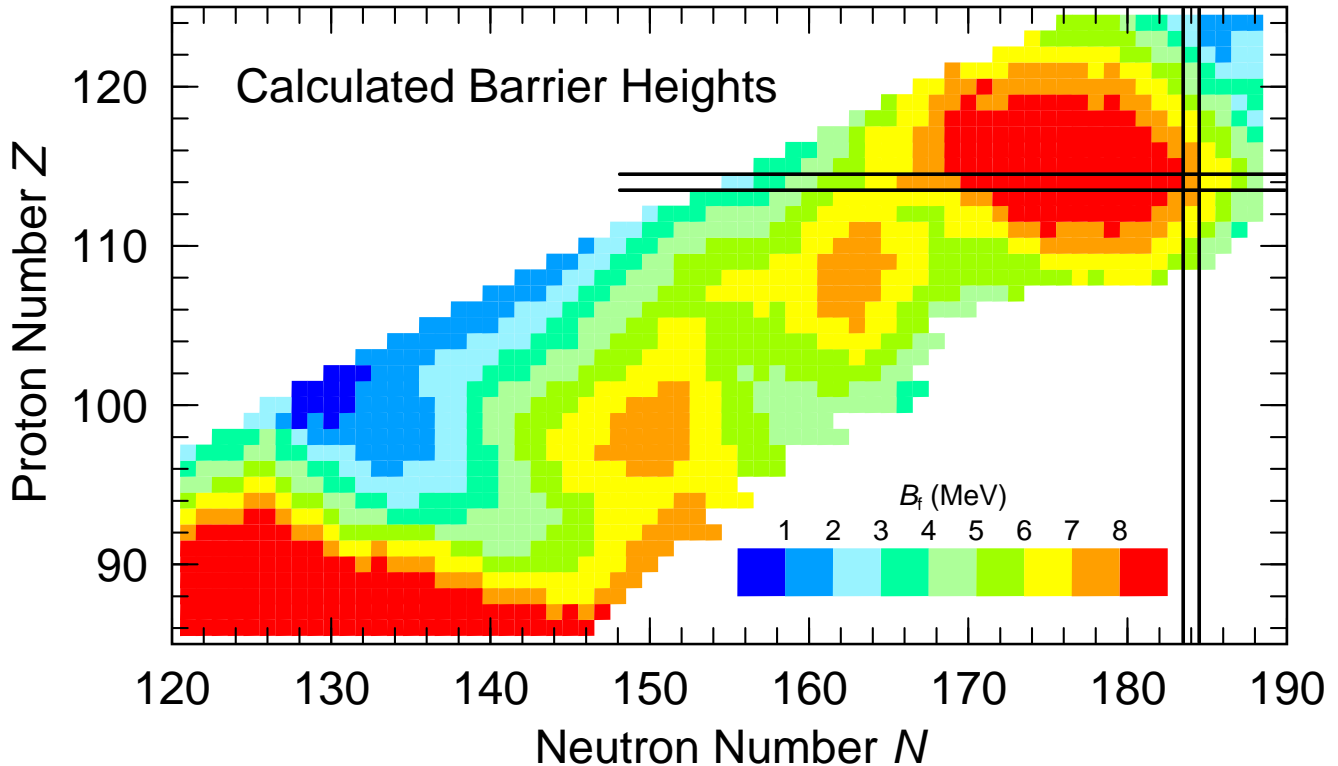


FIG. 33: (Color online) Calculated fission-barrier heights for 1122 heavy nuclei. As discussed in the text we find that the calculated barrier heights agree well with experimental data related to barrier heights (for example half-lives and regions of EC-delayed fission occurrence) for nuclei throughout the heavy region. Red color indicates barrier heights above 8 MeV (9 MeV and higher may be included).

To calculate spontaneous-fission half-lives it is necessary to know the fission potential energy, the inertia associated with the motion through the barrier and the path from the ground state through the barrier. Conceptually it is appealing to calculate the potential energy and inertia tensors in terms of several shape variables and then determine the least-action trajectory for barrier penetration by use of dynamical programming techniques, see for example [85]. Although this technique is theoretically very appealing it has in practice had results which are not an improvement over simpler, semi-empirical techniques [18, 31, 86–90]. In the semi-empirical technique optimum saddle points and minima are obtained from the multidimensional potential-energy surface. A one-dimensional fission barrier is then constructed by connecting neighboring minima by third-degree polynomials whose first derivatives are zero at the maxima and minima. This completely defines the barrier. The inertia is given by a semi-empirical model in which certain boundary conditions are imposed on the inertia. The model was introduced 35 years ago [86] and has been used in many studies; see [21] for a more recent review. It turns out that the semi-empirical inertia in practice agrees well with microscopic cranking-model results [85, 91]. Another reason for not using the microscopic approach here is that it has never been applied in five dimensions, which

would be extremely cumbersome. We therefore use the semi-empirical method here to predict a few fission half-lives based on our current potential-energy surfaces. The parameters of the semi-empirical inertia are those determined in 1976 [89] with generalizations introduced in 1987 [31] to allow studies of compact symmetric fission modes. We tabulate the calculated fission and α half-lives in Table IV. We also provide experimental values where available. For the first five entries in Table IV we have selected representative actinide nuclei to benchmark our calculations. We find excellent agreement between calculated and experimental half-lives, especially considering the extreme sensitivity of the calculated fission half-lives to small changes in calculated barrier energies. Results are especially sensitive to changes in the ground-state energy. A one-MeV change in this energy will give rise to a change in the calculated half-life of 6 orders of magnitude. It was stated in Refs. [21, 30] that one could expect average deviations between calculated and experimental fission half-lives of about 3 orders of magnitude. For Fm the calculated half-lives are 3–4 orders of magnitude too large. However, the average deviation for the five cases is within the expected three-order-of-magnitude accuracy of the approach. And it is noteworthy that we get quite reasonable results over the 27(!) order-of-magnitude variation of the experimental half-lives. For ^{258}Fm we have

used the mass parameter we associate with the compact fission valley [31]. For ^{232}Pu fission has not been observed experimentally; the α -decay half-life is 34m. Our calculated fission half-life is 19 days. This is compatible with observing only an α branch at almost 1000 times the calculated fission decay rate. We were surprised by this long fission half-life because the fission-barrier height in Table II is only 3.23 MeV. However, in the fission half-life calculations we use additional information from our potential-energy surfaces. The barrier for ^{232}Pu is double-humped and both the inner and outer peak are about 3 MeV. The fairly long fission half-life is a consequence of the barrier being relatively wide.

There is some interest in experimentally investigating stability for constant $N = 126$. Currently the heaviest known $N = 126$ isotone is ^{218}U . After our satisfactory benchmarking of our methods we have some confidence in applying the model to unknown nuclei and show on the next three lines predicted half-lives for fission and α decay of ^{222}Cm , ^{224}Cf , and ^{226}Fm . Clearly these nuclei would be fairly stable and decay mainly by α decay according to our predictions, if there were a sufficiently large evaporation-residue cross section in reactions which might be employed to produce them.

Although fission barriers or fission half-lives have not been systematically determined for nuclei with $107 \leq Z \leq 113$ discovered during the last 25 years or so [56, 92–97], we know that α decay usually is the dominant mode of decay. Consequently fission barriers have to be sufficiently high to correspond to fission-decay half-lives that are longer than the observed α half-lives. We compare the calculated fission half-life of $^{277}112$ to its calculated and measured α half-life in the last entry in Table IV. It is many orders of magnitude larger than the observed α half-life, so our results are consistent with the observations. The HFB and ETFSI 2-MeV barriers obtained for many such heavy systems are not consistent with these results. By artificially raising the ground state in our calculated potential barrier we find that we need at least a 4.5 MeV barrier to obtain 1 ms or longer half-lives for fission. This may seem contradictory to our result for ^{232}Pu above for which we obtained a 19 day half-life with only a 3.23 MeV barrier. However, that system has a two-peaked barrier, whereas $^{277}112$ only has a first barrier peak, which leads to a much narrower barrier, and consequently a much higher penetrability for a given barrier height. Our current results remain consistent with this explanation.

D. EC-delayed fission

An additional way to indirectly compare calculated fission-barrier heights to data is to consider EC-delayed fission data. Electron-capture delayed fission (ECdf) can be expected to be an observable decay branch if Q_{EC} is sufficiently high compared to the barrier height in the

TABLE V: (Color online) Calculated Q values Q_{EC} for electron capture and calculated fission-barrier heights B_f in the daughter of the EC decay for reactions where EC-delayed fission has been observed experimentally.

Reaction		Q_{EC} (MeV)	B_f (MeV)	$Q_{\text{EC}} - B_f$ (MeV)
$^{180}_{81}\text{Tl}$	$\xrightarrow{\text{EC}} ^{180}_{80}\text{Hg}$	10.44	9.81	0.63
$^{188}_{81}\text{Bi}$	$\xrightarrow{\text{EC}} ^{188}_{82}\text{Pb}$	10.83	10.32	0.51
$^{192}_{81}\text{At}$	$\xrightarrow{\text{EC}} ^{192}_{84}\text{Po}$	10.33	8.25	2.08
$^{194}_{81}\text{At}$	$\xrightarrow{\text{EC}} ^{194}_{84}\text{Po}$	9.42	9.46	-0.04
$^{196}_{81}\text{At}$	$\xrightarrow{\text{EC}} ^{196}_{84}\text{Po}$	9.10	10.29	-1.19
$^{228}_{93}\text{Np}$	$\xrightarrow{\text{EC}} ^{228}_{92}\text{U}$	4.26	5.13	-0.87
$^{232}_{95}\text{Am}$	$\xrightarrow{\text{EC}} ^{232}_{94}\text{Pu}$	4.88	3.23	1.65
$^{234}_{95}\text{Am}$	$\xrightarrow{\text{EC}} ^{234}_{94}\text{Pu}$	4.12	3.83	0.29
$^{238}_{97}\text{Bk}$	$\xrightarrow{\text{EC}} ^{238}_{96}\text{Cm}$	4.77	4.92	-0.15
$^{240}_{97}\text{Bk}$	$\xrightarrow{\text{EC}} ^{240}_{96}\text{Cm}$	3.85	5.85	-1.99
$^{242}_{99}\text{Es}$	$\xrightarrow{\text{EC}} ^{242}_{98}\text{Cf}$	5.22	6.16	-0.94
$^{244}_{99}\text{Es}$	$\xrightarrow{\text{EC}} ^{244}_{98}\text{Cf}$	4.45	6.69	-2.24
$^{246}_{99}\text{Es}$	$\xrightarrow{\text{EC}} ^{246}_{98}\text{Cf}$	3.69	7.16	-3.47
$^{248}_{99}\text{Es}$	$\xrightarrow{\text{EC}} ^{248}_{98}\text{Cf}$	2.98	7.24	-4.26
$^{246}_{101}\text{Md}$	$\xrightarrow{\text{EC}} ^{246}_{100}\text{Fm}$	6.28	6.13	0.14
$^{248}_{101}\text{Md}$	$\xrightarrow{\text{EC}} ^{248}_{100}\text{Fm}$	5.28	6.73	-1.45
$^{250}_{101}\text{Md}$	$\xrightarrow{\text{EC}} ^{250}_{100}\text{Fm}$	4.58	7.22	-2.64

daughter of the EC decay. A rough rule-of-thumb is that

$$Q_{\text{EC}} \gtrsim B_f - 2 \text{ MeV} \quad (27)$$

In Fig. 34 we show the magnitude of the window for ECdf and indicate where ECdf has been observed experimentally. There is limited experimental data available in the light Pb region [98–101]. More extensive and systematic studies have been carried out in the actinide region [102–112]. In Table V we compare Q_{EC} values obtained in the FRDM (1992) mass model [13] (experimental masses are not available) to our calculated barrier heights in the daughters following EC capture, for systems in which EC-delayed fission has been observed. Thirteen of the seventeen entries in the table fulfill the simple rule given by Eq. 27. All of the five deviations occur for nuclei near $Z \approx 100$ and $146 \leq N \leq 154$ and a possibility is that our calculated ground states here are too deep by one MeV or so. Figure 31 hints at this possibility. This would also be consistent with our four order-of-magnitude too long half-life for ^{252}Fm in table IV. Raising the ground-state energy by one MeV decreases the calculated half-life by six orders of magnitude. However, in general this comparison supports the overall reliability of our results. We are consistent with the data for EC delayed fission in the Pb region, so there is no obvious indication of divergence from data for very proton-rich nuclei near the proton drip line.

Calculated Energy Window for EC-Delayed Fission

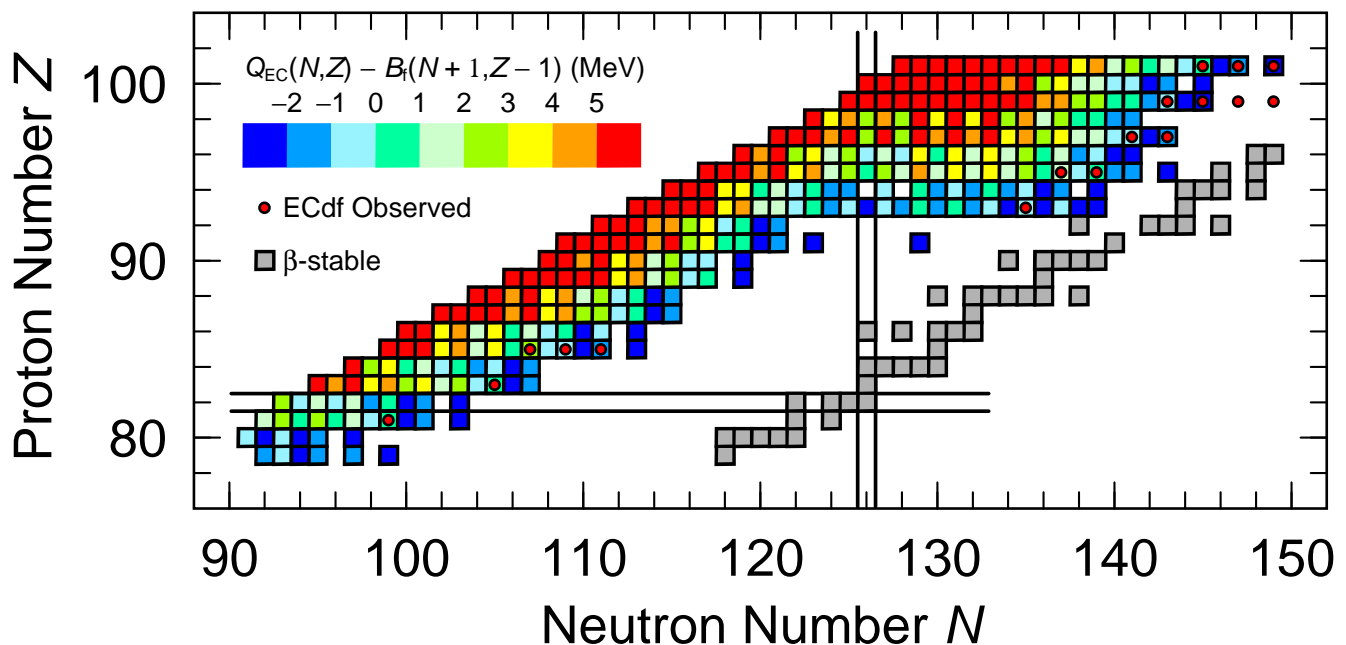


FIG. 34: (Color online) Window for fission in the daughter of EC decay. When the window is negative electron capture only populates daughter states at energies below the barrier saddle point. For states not too far below the barrier saddle some fission branching is still possible, see text for further discussion. New data in the neutron-deficient Pb region provide challenging tests for fission theory, far from the well-studied actinide region. Function values below -3 MeV are not plotted; red color indicates function values 5 MeV and higher (6 MeV and higher may be included).

E. Bimodal fission

Fission data for some nuclei have been interpreted as showing the presence of at least two separate *modes* of fission. Such coexistence in the data of two modes can involve, for example, two separated peaks in kinetic-energy distributions, symmetric and asymmetric peaks in fragment mass distributions, and separate thresholds for the onset of asymmetric and symmetric fission. Of particular interest are the correlations that can be observed among such properties. Early detailed observations of such features in the Ra region are in Refs. [59, 113–115]. Later, different coexisting fission modes were also observed in nuclei near ^{258}Fm [116, 117]. These authors coined the phrase “*bimodal fission*” for this type of fission.

We previously showed [10] that our potential-energy surfaces for ^{228}Ra are very consistent with the experimental observation of well separated symmetric and asymmetric fission modes; the symmetric mode having an about 2 MeV higher fission threshold and lower fragment kinetic energies than the asymmetric mode. Similar results were obtained for ^{234}U ; in this case the ridge separating the two modes is lower. In Fig. 16 we show that two well-separated modes are also present in the results for ^{232}Th . We find that the existence of two well-separated fission modes is a quite general feature in our results for light actinide nuclei.

A large Japanese collaboration has more recently per-

formed extensive and systematic studies of bimodality in fission of a substantial number of other light actinide nuclei, see for example Refs. [60, 118–123]. In their analysis they see evidence of bimodal fission in many systems, from ^{232}Th to ^{244}Cm . Our calculations here are consistent with several aspects of their results. We find that our scission shapes are more elongated for the symmetric fission mode, compared to the asymmetric fission mode. This is consistent with the observation that the fission-fragment kinetic energies are higher in asymmetric fission than in symmetric fission. Furthermore, in the analysis of their data in terms of two modes of fission they also observe that they must assume that the level-density parameter is 3%–15% larger in the symmetric mode than in the asymmetric mode [120]. We find for ^{232}Th that the symmetric level-density parameter is 15% higher than the asymmetric level-density parameter with the weights implied by a density fit, and 23% with the log fit, see Table III. Thus, we are consistent with the result of a larger level-density parameter in the symmetric mode, compared to the asymmetric mode. The analysis of bimodal aspects of actinide fission [120] furthermore concludes that the barrier corresponding to the symmetric mode is about 2 MeV higher than the barrier corresponding to the asymmetric mode. This is in contrast to our results. We find that the barrier leading to the symmetric mode becomes more nearly equal to the asymmetric barrier in Am isotopes, see Figs. 14, 15, and

17. However, in the analysis of [120] many simplifying assumptions are made that may have a significant impact on the barrier parameters that are obtained. For example, both the symmetric and asymmetric barriers are assumed to be *single-peaked* parabolic barriers. The barrier curvature parameters are not fitted, they are imposed and simple phenomenological Fermi-gas models are used for level densities. A definite conclusion on how realistic the parameters of our calculated barriers for the symmetric and asymmetric modes are can probably not be drawn until a more refined analysis of the experimental data is carried out. At this point there is no standard approach available for such an analysis. It is our hope that our more detailed potential-energy-surface predictions can stimulate developments in this direction.

For nuclei near ^{258}Fm the bimodal features are somewhat reversed compared to the observations for the lighter actinides. In particular, in spontaneous fission two peaks in the kinetic-energy distributions are observed simultaneously, and it is the symmetric mode that is associated with the higher kinetic energy. It had been assumed that the two modes would correspond to different fission barriers, one corresponding to symmetric fission and high fission-fragment kinetic energy and a second mode corresponding to asymmetric fission and lower kinetic energy. A perceived mystery at the time of these studies was why different barriers could yield similar probabilities for spontaneous fission, as both modes were observed in the same experiment with not too different probabilities. This was taken to mean that the spontaneous fission half-lives for the different barriers had to be similar. However, just adding two neutrons to ^{256}Fm , which is predominantly asymmetric, decreased the half-life from 2.63 days to 0.37ms in ^{258}Fm , possessing a significant symmetric component. This corresponds to a 7 order-of-magnitude change. So it was assumed the mystery was why there was not a similar difference in the probabilities of the two modes when they were observed in the same nucleus, because barriers corresponding to the different modes must surely differ just as substantially as the barrier difference between ^{256}Fm and ^{258}Fm . In Ref. [117] the abstract stated that “...*no physical grounds have been advanced that would allow the near equal populations traveling each path. We suggest that this failure to find a reason for the somewhat equal branching may be a fundamental flaw of current fission models.*”

It is unfortunate that such a strong statement was made, when in fact physical grounds had been advanced some three years previously in Ref. [31]. As is common in mysteries, a large part of a mystery arises because the problem is (unknowingly) deceptively presented. The question was asked, “how can two (different, totally uncorrelated) barriers correspond to similar half-lives?” The parenthesized words were not always explicitly expressed but were implied. The answer is, of course, they cannot. But the fact here is that the barriers are not uncorrelated nor are they totally different. The calculations

of potential-energy surfaces for ^{258}Fm and nearby nuclei in [31] were only based on about 300 deformation points, but were sufficiently informative to lead to the explanation. The key observation is that the barriers or paths defining the asymmetric and symmetric barriers only become separate after the second minimum, and the barrier penetrability is dominated by the first peak. From Ref. [31], “...*the same barrier is penetrated in the two cases except for a tiny portion at the end of the penetration process.*” In our current calculations the essential features of the previous results are retained (see Ref. [10], especially Fig. 6 and the associated discussion.) The principle behind the simultaneous observation of the characteristic signatures of both modes in the same experiment is further elucidated in Refs. [18, 21, 124]. We illustrate by a test half-life calculation the insensitivity of the half-lives to realistic differences in the two relatively tiny sections of the outer barrier that define the two fission modes. In the fifth line of Table IV we present the calculated half-life for compact fission into the new valley (cf. Ref. [31] for terminology), and note we agree to within 4 orders of magnitude. The first barrier, second minimum, and second barrier with respect to the ground state are 5.32, 2.27 and 4.69 MeV. We add a zero-point energy of 0.8 to the ground-state energy leading in Table IV to the barrier height of 4.52 MeV. To study the sensitivity of the half-life to changes in the outer barrier where the only difference between the two modes originate, we now calculate the half-life for a 1 MeV higher outer barrier and obtain for the log of the lifetime -6.82 , compared to -7.34 for the barrier we actually calculated. In Ref. [31] the barrier along the switchback path, the tiny outer part of the barrier that takes you into the “old” valley leading to elongated fragments and low-kinetic-energy events was found to be only 0.3 MeV higher than the compact-mode barrier. Of course the switchback path is associated with a different inertia compared to the compact path, and possibly a different path length, but since the parts of the barrier that differ between compact and elongated fission modes are such small fractions of the complete barrier, we expect that these differences, just like differences in barrier height, will only have a small influence on the total barrier penetrabilities. Thus, 20 years ago we presented a physical picture that allows nearly equal populations of the two fission modes. Since the paths associated with the two modes only separate along a tiny portion of the barrier, where the inertia is much lower than in the common section of the barrier, this explanation is relatively model-insensitive and robust.

Acknowledgments

The authors are grateful to A. N. Andreyev, L. Bonneau, A. Juodagalvis, F. Kondev, H. Nakahara, K. Nishio, T. Ohtsuki, J. M. Pearson, and W. J. Swiatecki for valuable discussions. P. M. thanks JAEA (formerly JAERI) for supporting the original work on 5D potential-

Fission-Barrier and Associated Shapes for ^{242}Am

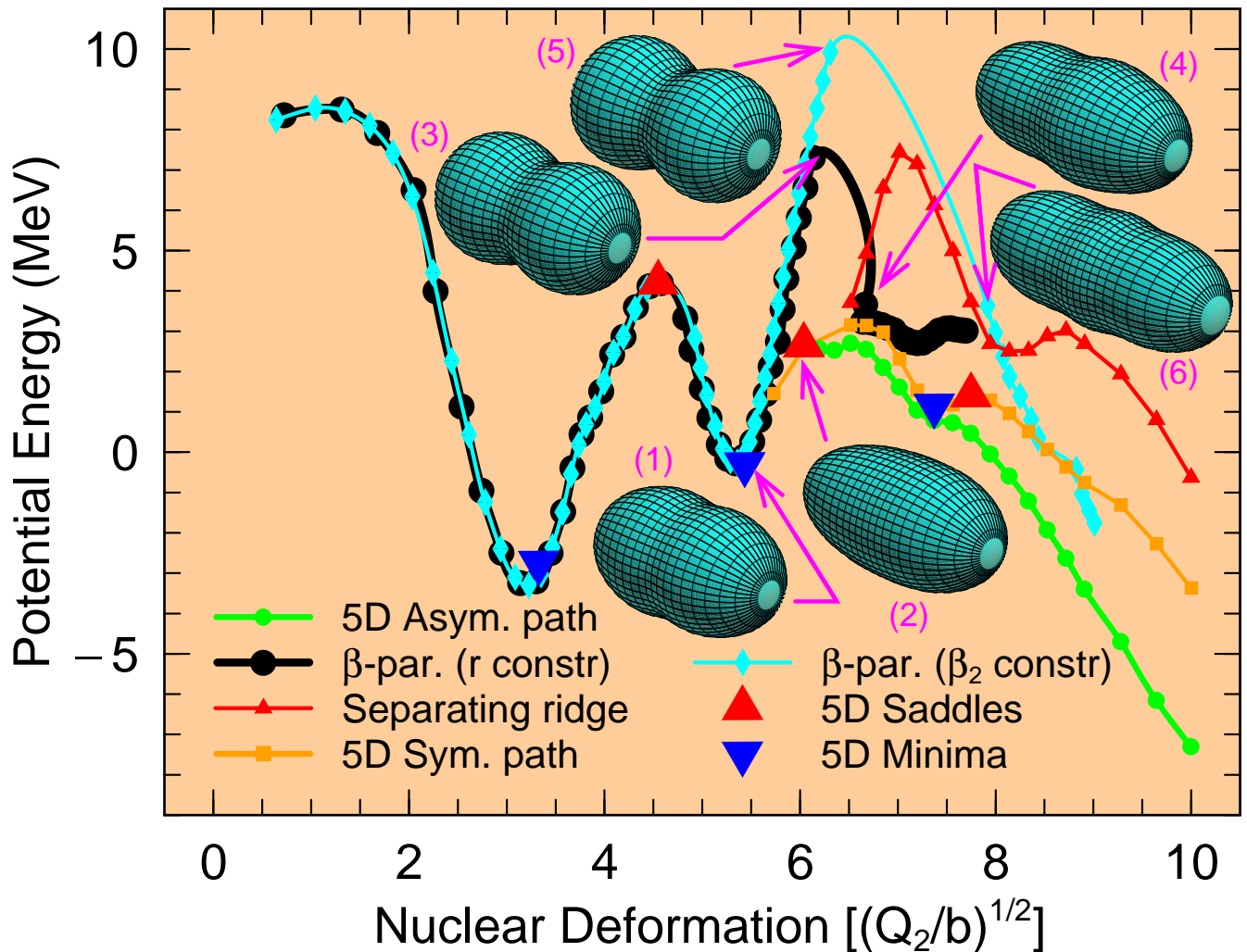


FIG. 35: (Color online) The same fission-barrier structure for ^{242}Am shown in Fig. 15, with shapes for selected points displayed.

energy surfaces during a 3-month visit in 1998–1999, and the Department of Mathematical Physics, Lund Institute of Technology, for hospitality during several visits in 2002–2008. T. I., A. I., R. B., and H. U. would like to thank LANL for hospitality during visits in 2002–2007.

This work was supported by travel grants for P. M. to JUSTIPEN (Japan-U. S. Theory Institute for Physics with Exotic Nuclei) under grant number DE-FG02-06ER41407 (U. Tennessee).

This work was carried out under the auspices of the National Nuclear Security Administration of the U. S. Department of Energy at Los Alamos National Laboratory under Contract No. DE-AC52-06NA25396.

VIII. APPENDIX

In this appendix we discuss in more detail the nature of the difficulties encountered when applying the minimiza-

tion method in the neighborhood of the second barrier in ^{242}Am , shown in Fig. 15. In the calculation in which β_2 is constrained, we increase it in steps of 0.02. In the calculation in which r is constrained, it is increased in steps of 0.015. In Figure 35 we reproduce the barrier structure from Fig. 15 along with some selected shapes. The isomer shape (1) is essentially the same in all three calculations. It is a reflection-symmetric shape comprising prolate spheroids with a neck having a large curvature joining them. The second saddle uncovered by immersion in the 3QS analysis has a very different shape (2), exhibiting reflection asymmetry and no neck. Both constrained calculations follow a sequence of similar reflection symmetric shapes with end bodies of decreasing eccentricity and necks with increasing curvature. In the r -constrained calculation, the last shape in this sequence (3) is found at $r = 1.335$, which has $Q_2 = 37.6$. The shape which immediately follows (4), with $r = 1.350$, lies in a different family, being asymmetric with no neck and

having $Q_2 = 44.5$. Even though the energy for increasing Q_2 values is very close to that of the 5D symmetric path (gold squares), the shapes possess an increasing asymmetry, and are different from those along the 5D path. The solid black line connecting the two points before and after the jump is only to guide the eye, as the energies in the intermediate region are not defined in this constrained calculation. When β_2 is the constraint, the last shape in the initial family (5) occurs at $\beta_2 = 0.98$, with $Q_2 = 39.8$. The $\beta_2 = 1.00$ shape (6) jumps to still another family with reflection symmetry and $Q_2 = 62.6$, having an equatorial bulge in place of a neck. This solution jumps again between $\beta_2 = 1.12$ and $\beta_2 = 1.14$ to a

still different symmetric family having larger β_4 and β_6 values and with Q_2 jumping from 71.6 to 77.9. The cyan line is again only to guide the eye, with the energies from $Q_2 = 40$ to 60 not defined.

We discussed above that there is a more systematic way of identifying the proliferation of valleys which can lead any constrained calculation astray. Using this method we find that the 4D space corresponding to $Q_2 = 80$ is intersected by 5 valleys, each at least 0.2 MeV deep, one of which is reflection symmetric.

-
- [1] L. Meitner and O. R. Frisch, *Nature* **143** (1939) 239.
 [2] N. Bohr and J. A. Wheeler, *Phys. Rev.* **56** (1939) 426.
 [3] S. Frankel and N. Metropolis, *Phys. Rev.* **72** (1947) 914.
 [4] W. J. Swiatecki, *Phys. Rev.* **100** (1955) 937.
 [5] V. M. Strutinsky, *Nucl. Phys.* **A95** (1967) 420.
 [6] V. M. Strutinsky, *Nucl. Phys.* **A122** (1968) 1.
 [7] P. Möller and J. R. Nix, *Proc. Third IAEA Symp. on the physics and chemistry of fission*, Rochester, 1973, vol. I (IAEA, Vienna, 1974) p. 103.
 [8] P. Möller and A. Iwamoto, *Phys. Rev. C* **61** (2000) 047602.
 [9] P. Möller, D. G. Madland, A. J. Sierk, and A. Iwamoto, *Tours 2000, Tours Symposium on Nuclear Physics IV*, Tours, France September 4–7, 2000, and AIP Conference Proceedings 561 (2001) p. 455.
 [10] P. Möller, D. G. Madland, A. J. Sierk, and A. Iwamoto, *Nature* **409** (2001) 785.
 [11] P. Möller, D. G. Madland, A. J. Sierk, and A. Iwamoto, *Proc. International Conference on Nuclear Data for Science and Technology (ND2001)*, October 7–12, Tsukuba, Japan, *Journal of Nuclear Science and Technology, Supplement 2*, (2002) pp. 703–708.
 [12] P. Möller, A. J. Sierk, and A. Iwamoto, *Phys. Rev. Lett.* **92** (2004) 072501.
 [13] P. Möller, J. R. Nix, W. D. Myers, and W. J. Swiatecki, *Atomic Data Nucl. Data Tables* **59** (1995) 185.
 [14] M. Bolsterli, E. O. Fiset, J. R. Nix, and J. L. Norton, *Phys. Rev. C* **5** (1972) 1050.
 [15] P. Möller, S. G. Nilsson, and J. R. Nix, *Nucl. Phys.* **A229** (1974) 292.
 [16] P. Möller and J. R. Nix, *Nucl. Phys.* **A281** (1977) 354.
 [17] P. Möller and J. R. Nix, *Nucl. Phys.* **A361** (1981) 117.
 [18] P. Möller, J. R. Nix, and W. J. Swiatecki, *Nucl. Phys.* **A492** (1989) 349.
 [19] P. Möller and J. R. Nix, *Nucl. Phys.* **A536** (1992) 20.
 [20] P. Möller and J. R. Nix, *Proc. 6th Int. Conf. on nuclei far from stability and 9th Int. Conf. on nuclear masses and fundamental constants*, Bernkastel-Kues, 1992 (IOP Publishing, Bristol, 1993) p. 43.
 [21] P. Möller and J. R. Nix, *J. Phys. G* **20** (1994) 1681.
 [22] P. Möller, J. R. Nix, and K.-L. Kratz, *Atomic Data Nucl. Data Tables* **66** (1997) 131.
 [23] H. Flocard, P. Quentin, A. K. Kerman, D. Vautherin, *Nucl. Phys.* **A203** (1973) 433.
 [24] P. Ring and P. Schuck, *The Nuclear Many-Body Problem* (Springer-Verlag, New York, 1980).
 [25] M.B. Chadwick, P. Obložinsky, M. Herman, N.M. Greene, R.D. McKnight, D.L. Smith, P.G. Young, R.E. MacFarlane, G.M. Hale, R.C. Haight, S. Frankle, A.C. Kahler, T. Kawano, R.C. Little, D.G. Madland, P. Möller, R. Mosteller, P. Page, P. Talou, H. Trellue, M. White, W.B. Wilson, R. Arcilla, C.L. Dunford, S.F. Mughabghab, B. Pritychenko, D. Rochman, A.A. Sonzogni, C. Lubitz, T.H. Trumbull, J. Weinman, D. Brown, D.E. Cullen, D. Heinrichs, D. McNabb, H. Derrien, M. Dunn, N.M. Larson, L.C. Leal, A.D. Carlson, R.C. Block, B. Briggs, E. Cheng, H. Huria, K. Kozier, A. Courcelle, V. Pronyaev, S.C. van der Marck (CSEWG Collaboration), *Nuclear Data Sheets*, **107** (2007) 2931.
 [26] B. Hayes, *Am. Sci.* **88** (2000) 481.
 [27] J. R. Nix, *University of California Radiation Laboratory Report UCRL-17958* (1968).
 [28] J. R. Nix, *Nucl. Phys.* **A130** (1969) 241.
 [29] P. Möller, R. Bengtsson, B. G. Carlsson, P. Olivius, T. Ichikawa, H. Sagawa, and A. Iwamoto *ATOMIC DATA AND NUCLEAR DATA TABLES* **94** (2008) 758.
 [30] P. Möller and J. R. Nix, *Nucl. Phys.* **A272** (1976) 502.
 [31] P. Möller, J. R. Nix, and W. J. Swiatecki, *Nucl. Phys.* **A469** (1987) 1.
 [32] S. G. Nilsson, *Kgl. Danske Videnskab. Selskab. Mat.-Fys. Medd.* **29**:No. 16 (1955).
 [33] S. G. Nilsson, C. F. Tsang, A. Sobiczewski, Z. Szymański, S. Wycech, C. Gustafson, I.-L. Lamm, P. Möller, and B. Nilsson, *Nucl. Phys.* **A131** (1969) 1.
 [34] W. M. Howard and P. Möller, *Atomic Data Nucl. Data Tables* **25** (1980) 219.
 [35] A. Iwamoto, P. Möller, J. R. Nix, and H. Sagawa, *Nucl. Phys.* **A596** (1996) 329.
 [36] S. Bjørnholm and J. E. Lynn, *Rev. Mod. Phys.* **52** (1980) 725.
 [37] H. Uhrenholt, S. Åberg, P. Möller, and T. Ichikawa, in preparation.
 [38] T. Dössing *et. al.*, *Phys. Rev. Lett.* **75** (1995) 1276.
 [39] Å. Bohr and B. R. Mottelson, *Nuclear Structure*, vol. 1 (Benjamin, New York, 1969).
 [40] S. Bjørnholm, A. Bohr and B. Mottelson, *Proc. Third IAEA Symp. on the physics and chemistry of fission*, Rochester, 1973, vol. I (IAEA, Vienna, 1974) p. 367.
 [41] R. Bengtsson and S. Åberg, *Phys. Lett.* **B172** (1986)

- 277.
- [42] S. Hilaire and S. Goriely, Nucl. Phys. **A 779** (2006) 63.
- [43] A. V. Ignatyuk, J. L. Weil, S. Raman and S. Kahane, Phys. Rev. **C 47** (1993) 1504.
- [44] Handbook for calculations of nuclear reaction data, Reference Input Parameter Library. IAEA-TECDOC-1034 (IAEA, Vienna, 1998).
- [45] T. Belgya, O. Bersillon, R. Capote, T. Fukahori, G. Zhi-gang, S. Goriely, M. Herman, A.V. Ignatyuk, S. Kailas, A. Koning, P. Oblozinsky, V. Plujko and P. Young. Handbook for calculations of nuclear reaction data, RIPL-2. IAEA-TECDOC-1506 (IAEA, Vienna, 2006). Available online at <http://www-nds.iaea.org/RIPL-2/>.
- [46] S. Ćwiok, P. Rozmej, A. Sobiczewski, and Z. Patyk, Nucl. Phys. **A491** (1989) 281.
- [47] S. Ćwiok, W Nazarewicz, J. X. Saladin, W. Plociennik, A. Johnson, Phys. Lett. **B322**, 304 (1994).
- [48] G. M. Ter-Akopian, J. H. Hamilton, Y. T. Oganessian, A. V. Daniel, J. Kormicki, A. V. Ramayya, G. S. Popeko, B. R. S. Babu, Q. H. Lu, K. Butlermoore, W. C. Ma, S. Ćwiok, W. Nazarewicz, J. K. Deng, D. Shi, J. Kliman, M. Morhac, J. D. Cole, R. Aryaajnejad, N. R. Johnson, I. Y. Lee, F. K. McGowan, J. X. Saladin, Phys. Rev. Lett. **77**, 32 (1996).
- [49] Y. V. Pyatkov, V. V. Pashkevich, Y. E. Penionzhkevich, V. G. Tischenko, A. V. Unzhakova, H. G. Ortlepp, P. Gippner, C. M. Herbach, W. Wagner, Nucl. Phys. **A624**, 140 (1997).
- [50] J. L. Egido, L. M. Robledo, and R. R. Chasman, Phys. Lett. **B393**, (1997) 13.
- [51] J. F. Berger, M. Girod, and D. Gogny, Nucl. Phys. **A502** (1989) c85.
- [52] W. D. Myers and W. J. Swiatecki, Nucl. Phys. **A601** (1996) 141.
- [53] A. Mamdouh, J. M. Pearson, M. Rayet, and F. Tondeur, Nucl. Phys. **A644** (1998) 389.
- [54] V. Luc and P. Soille, IEEE Transactions on Pattern Analysis and Machine Intelligence, **13** (1991) 583.
- [55] M. Samyn, S. Goriely, M. Bender, and J.M. Pearson, Phys Rev. C **70** (2004) 044309.
- [56] K. Morita, K. Morimoto, D. Kaji, H. Haba, E. Ideguchi, R. Kanungo, K. Katori, H. Koura, H. Kudo, T. Ohnishi, A. Ozawa, T. Suda, K. Sueki, I. Tanihata, H. Xu, A. V. Yeremin, A. Yoneda, A. Yoshida, Y.-L. Zhao, and T. Zheng, Eur. Phys. J. **A 21** (2004) 257.
- [57] P. Möller and A. Iwamoto, Proc. Conf. on Nuclear Shapes and Motions. Symposium in Honor of Ray Nix, 25–27 Oct. 1998, Sante Fe, NM, USA Acta Physica Hungarica, New Series, **10** (1999) 241.
- [58] P. Möller, D. G. Madland, and A. Iwamoto Kyoto University Research Reactor Institute Report, Proceedings of Specialists' Meeting on Interdisciplinary Approach to Nuclear Fission, 2000, January 18–19, 2000, Kyoto University Research Reactor Institute, Kumatori-cho, Osaka, Japan (LA-UR-001435), URL:<http://t16web.lanl.gov/Moller/publications/kumatori2000.html>.
- [59] E. Konecny, H. J. Specht, and J. Weber, Proc. Third IAEA Symp. on the Physics and Chemistry of Fission, Rochester, 1973, vol. II (IAEA, Vienna, 1974) p. 3.
- [60] Y. L. Zhao, I. Nishinaka, Y. Nagame, K. Tsukada, M. Tanikawa, K. Sueki, Y. Oura, S. Ichikawa, H. Ikezoe, T. Ohtsuki, H. Kudo, and H. Nakahara, J. Alloys and Comp. **271** (1998) 327.
- [61] H. Goutte, J. F. Berger, P. Casoll, and D. Gogny, Phys. Rev. C **71** (2005) 24316.
- [62] D. G. Madland, private communication, (2000).
- [63] B. B. Back, O. Hansen, H. C. Britt, and J. D. Garrett, Phys. Rev. C **9** (1974) 1924.
- [64] B. B. Back, H. C. Britt, O. Hansen, B. Leroux, and J. D. Garrett, Phys. Rev. C **10** (1974) 1948.
- [65] H. C. Britt, Proc. 4th IAEA Symp. on physics and chemistry of fission, Jülich, 1979, vol. I (IAEA, Vienna, 1980) p. 3.
- [66] G. Audi, Midstream atomic mass evaluation, private communication (1989), with four revisions.
- [67] J. Blons, R Fabbro, C. Mazur, D. Paya, M. Ribrag, Y. Patin, Nucl. Phys. **A477** (1988) 231.
- [68] U. Mosel and H. W. Schmitt, Phys. Rev. C **4** (1971) 2185.
- [69] P. Möller, Nucl. Phys. **A192** (1972) 529.
- [70] S. E. Larsson, I. Ragnarsson, and S. G. Nilsson, Phys. Lett. **38B** (1972) 269.
- [71] U. Götz, H. C. Pauli, and K. Junker, Phys. Lett. **39B** (1972) 436.
- [72] S. E. Larsson and G. Leander, Proc. Third IAEA Symp. on the physics and chemistry of fission, Rochester, 1973, vol. I (IAEA, Vienna, 1974) p. 177.
- [73] H. C. Pauli and T. Ledergerber, Proc. Third IAEA Symp. on the physics and chemistry of fission, Rochester, 1973, vol. I (IAEA, Vienna, 1974) p. 463.
- [74] M. Samyn, S. Goriely, and J.M. Pearson, Phys Rev. C **72** (2005) 044316.
- [75] P. Möller, R. Bengtsson, B. G. Carlsson, P. Olivius, and T. Ichikawa, Phys. Rev. Lett. **97** (2006) 162502.
- [76] S. Goriely, F. Tondeur, and J. M. Pearson, Atomic Data Nucl. Data Tables, **77** (2001) 311.
- [77] S. Goriely, M. Samyn, and, J. M. Pearson, Phys. Rev. C **75** (2007) 064312.
- [78] W. Stocker, J. Bartel, J. R. Nix, and A. J. Sierk, Nucl. Phys. **A489** (1988) 252.
- [79] P.-G. Reinhard, M. Bender, W. Nazarewicz, and T. Vertse, Phys. Rev. C **73** (2006) 014309.
- [80] D. Lunney, J. M. Pearson, C. Thibault, Rev. Mod. Phys. **75** (2003) 1021.
- [81] N. E. Holden and D. C. Hoffman, Pure and Appl. Chem. **72** (2000) 1525.
- [82] G. Audi, O. Bersillon, J. Blanchot, and A. H. Wapstra, Nucl. Phys. **A729** (2003) 3.
- [83] P. Möller, J. R. Nix, P. Armbruster, S. Hofmann, G. Münzenberg, Z. Phys. **A359** (1997) 251.
- [84] P. Möller, B. Pfeiffer, and K.-L. Kratz, Phys. Rev. C, **67** (2003) 055802.
- [85] A. Baran, K. Pomorski, A. Lukasiak, and A. Sobiczewski, Nucl. Phys. **A361** (1981) 83.
- [86] E. O. Fiset and J. R. Nix, Nucl. Phys. **A193** (1972) 647.
- [87] J. Randrup, C. F. Tsang, P. Möller, S. G. Nilsson, and S. E. Larsson, Nucl. Phys. **A217** (1973) 221.
- [88] J. Randrup, S. E. Larsson, P. Möller, S. G. Nilsson, K. Pomorski, and A. Sobiczewski, Phys. Rev. C **13** (1976) 229.
- [89] P. Möller and J. R. Nix, Phys. Rev. Lett. **37** (1976) 1461.
- [90] G. A. Leander, P. Möller, J. R. Nix, and W. M. Howard, Proc. 7th Int. Conf. on nuclear masses and fundamental constants (AMCO-7), Darmstadt-Seeheim, 1984 (Lehrdruckerei, Darmstadt, 1984) p. 466.
- [91] A. Baran, K. Pomorski, S. E. Larsson, P. Möller, S. G. Nilsson, J. Randrup, A. Lukasiak, and A. Sobiczewski,

- Proc. 4th IAEA Symp. on physics and chemistry of fission, Jülich, 1979, vol. I (IAEA, Vienna, 1980) p. 143.
- [92] G. Münzenberg, S. Hofmann, F. P. Heßberger, W. Reisdorf, K.-H. Schmidt, J. R. H. Schneider, P. Armbruster, C.-C. Sahn, and B. Thuma, *Z. Phys.* **A300** (1981) 7.
- [93] G. Münzenberg, P. Armbruster, F. P. Heßberger, S. Hofmann, K. Poppensieker, W. Reisdorf, J. R. H. Schneider, W. F. W. Schneider, K.-H. Schmidt, C.-C. Sahn, and D. Vermeulen, *Z. Phys.* **A309** (1982) 89.
- [94] G. Münzenberg, P. Armbruster, H. Folger, F. P. Heßberger, S. Hofmann, J. Keller, K. Poppensieker, W. Reisdorf, K.-H. Schmidt, H. J. Schött, M. E. Leino, and R. Hingmann, *Z. Phys.* **A317** (1984) 235.
- [95] S. Hofmann, V. Ninov, F. P. Heßberger, P. Armbruster, H. Folger, G. Münzenberg, H. J. Schött, A. G. Popeko, A. V. Yeremin, A. N. Andreyev, S. Saro, R. Janik, and M. Leino, *Z. Phys.* **A350** (1995) 277.
- [96] S. Hofmann, V. Ninov, F. P. Heßberger, P. Armbruster, H. Folger, G. Münzenberg, H. J. Schött, A. G. Popeko, A. V. Yeremin, A. N. Andreyev, S. Saro, R. Janik, and M. Leino, *Z. Phys.* **A350** (1995) 281.
- [97] S. Hofmann, V. Ninov, F. P. Heßberger, P. Armbruster, H. Folger, G. Münzenberg, H. J. Schött, A. G. Popeko, A. V. Yeremin, S. Saro, R. Janik, and M. Leino, *Z. Phys.* **A354** (1996) 229.
- [98] D. Galeriu, *J. Phys. G: Nucl. Phys.* **9** (1983) 309.
- [99] Yu. A. Lazarev, Yu. T. Oganessian, I. V. Shirokovsky, S. P. Tretyakova, V. K. Utyonkov, and G. V. Buklanov, *Europhys. Lett.* **4** (1987) 893.
- [100] A. N. Andreyev, D. D. Bogdanov, S. Saro, G. M. Ter-Akopian, M. Veselsky and A. V. Yeremina, *Phys. Lett. B* **312** (1993) 49.
- [101] A. N. Andreyev, S. Antalic, D. Ackermann, L. Bianco, S. Franchoo, S. Heinz, F. P. Heßberger, S. Hofmann, M. Huyse, I. Kojouharov, B. Kindler, B. Lommel, R. Mann, K. Nishio, R. D. Page, J. Ressler, P. Sappale, S. Saro, B. Sulignano, J. Thomson, P. Van Duppen, and M. Venhart, *Phys. Rev. C* (2008) to be published.
- [102] Yu. P. Grangrsky, M. B. Miller, L. V. Mikailov, I. F. Kharisov, *Sovj. J. Nucl. Phys.* **31** (1980) 162.
- [103] H. L. Hall, K. E. Gregorich, R. A. Henderson, D. M. Lee, D. C. Hoffman, M. E. Bunker, M. M. Fowler, P. Lysaght, J. W. Starner, J. B. Wilhelmy, *Phys. Rev. C* **39** (1989) 1666.
- [104] H. L. Hall, K. E. Gregorich, R. A. Henderson, C. M. Gannett, R. B. Chadwick, J. D. Leyba, K. R. Czerwinski, B. Kadkhodayan, S. A. Kreek, D. M. Lee, M. J. Nurmia, D. C. Hoffman, *Phys. Rev. Lett.* **63** (1989) 2548.
- [105] H. L. Hall, K. E. Gregorich, R. A. Henderson, C. M. Gannett, R. B. Chadwick, J. D. Leyba, K. R. Czerwinski, B. Kadkhodayan, S. A. Kreek, D. M. Lee, M. J. Nurmia, D. C. Hoffman, C. E. A. Palmer, P. A. Baisden, *Phys. Rev. C* **41** (1990) 618.
- [106] H. L. Hall, K. E. Gregorich, R. A. Henderson, C. M. Gannett, R. B. Chadwick, J. D. Leyba, K. R. Czerwinski, B. Kadkhodayan., S. A. Kreek, N. J. Hannink, D. M. Lee, M. J. Nurmia, D. C. Hoffman, C. E. A. Palmer, P. A. Baisden, *Phys. Rev. C* **42** (1990) 1480.
- [107] S. A. Kreek, H. L. Hall, K. E. Gregorich, R. A. Henderson, J. D. Leyba, K. R. Czerwinski, B. Kadkhodayan, M. P. Neu, C. D. Kacher, T. M. Hamilton, M. R. Lane, E. R. Sylwester, A. Türler, D. M. Lee, M. J. Nurmia, and D. C. Hoffman, *Phys. Rev. C* **50**, (1994) 2288.
- [108] A. Kreek, H. L. Hall, K. E. Gregorich, R. A. Henderson, J. D. Leyba, K. R. Czerwinski, B. Kadkhodayan, M. P. Neu, C. D. Kacher, T. M. Hamilton, M. R. Lane, E. R. Sylwester, A. Türler, D. M. Lee, M. J. Nurmia, and D. C. Hoffman, *Phys. Rev. C* **49**, (1994) 1859.
- [109] V. Ninov, F. P. Hessberger, S. Hofmann, H. Folger, G. Münzenberg, P. Armbruster, A. V. Yeremin, A. G. Popeko, M. Leino, and S. Saro, *Z. Phys. A* **356** (1996) 11.
- [110] D. A. Shaughnessy, J. L. Adams, K. E. Gregorich, M. R. Lane, C. A. Laue, D. M. Lee, C. A. McGrath, J. B. Patin, D. A. Strellis, E. R. Sylwester, P. A. Wilk, and D. C. Hoffman, *Phys. Rev. C* **61** (2000) 044609.
- [111] D. A. Shaughnessy, K. E. Gregorich, M. R. Lane, C. A. Laue, D. M. Lee, C. A. McGrath, D. A. Strellis, E. R. Sylwester, P. A. Wilk, and D. C. Hoffman, *Phys. Rev. C* **63** (2001) 037603.
- [112] D. A. Shaughnessy, K. E. Gregorich, M. R. Lane, C. A. Laue, D. M. Lee, C. A. McGrath, V. Ninov, J. B. Patin, D. A. Strellis, E. R. Sylwester, P. A. Wilk, and D. C. Hoffman, *Phys. Rev. C* **65** (2002) 024612.
- [113] E. Konecny, H. J. Specht, and J. Weber, *Phys. Lett.* **B45** (1973) 329.
- [114] J. Weber, J.C. Britt, A. Gavron, E. Konecny, and J.B. Wilhelmy, *Phys. Rev. C* **13** (1976) 2413.
- [115] J. Aschenbach, G. Fiedler and E. Konecny, *Nucl. Phys.* **A260** (1976) 287.
- [116] E. K. Hulet, J. F. Wild, R. J. Dougan, R. W. Lougheed, J. H. Landrum, A. D. Dougan, M. Schädel, R. L. Hahn, P. A. Baisden, C. M. Henderson, R. J. Dupzyk, K. Sümmerer, and G. R. Bethune, *Phys. Rev. Lett.* **56** (1986) 313.
- [117] E. K. Hulet, J. F. Wild, J. Dougan, R. W. Lougheed, J. H. Landrum, A. D. Dougan, P. A. Baisden, C. M. Henderson, R. J. Dupzyk, R. L. Hahn, M. Schädel, K. Sümmerer, G. R. Bethune, *Phys. Rev. C* **40** (1989) 770.
- [118] T. Ohtsuki, Y. Hamajima, K. Sueki, H. Nakahara, Y. Nagame, N. Shinohara, H. Ikezoe, *Phys. Rev. C* **40** (1986) 2144.
- [119] T. Ohtsuki, Y. Nagame, K. Tsukada, N. Shinohara, S. Baba, K. Hashimoto, I. Nishinaka, K. Sueki, Y. Hatsukawa, K. Hata, T. Sekine, I. Kanno, H. Ikezoe, H. Nakahara, *Affiliation: D Phys. Rev. C* **44** (1991) 1405.
- [120] T. Ohtsuki, H. Nakahara, and Y. Nagame, *Phys. Rev. C* **48** (1993) 1667.
- [121] Y. Nagame, I. Nishinaka, K. Tsukada, S. Ichikawa, H. Ikezoe, Y. L. Zhao, Y. Oura, K. Sueki, H. Nakahara, M. Tanikawa, T. Ohtsuki, K. Takamiya, K. Nakanishi, H. Kudo, Y. Hamajima, and Y. H. Chung, *Radiochimica Acta*, **78** (1997) 3.
- [122] Y. L. Zhao, I. Nishinaka, Y. Nagame, M. Tanikawa, K. Tsukada, S. Ichikawa, K. Sueki, Y. Oura, H. Ikezoe, S. Mitsuoka, H. Kudo, T. Ohtsuki, and H. Nakahara, *Phys. Rev. Lett.* **82** (1999) 3408.
- [123] Y. Nagame, I. Nishinaka, Y. L. Zhao, K. Tsukada, S. Ichikawa, Z. Qin, H. Ikezoe, Y. Oura, K. Sueki, H. Nakahara, M. Tanikawa, T. Ohtsuki, S. Goto, H. Kudo, Y. Hamajima, K. Takamiya, K. Nakanishi, H. Baba, *J. Radioanal. Nucl. Chem.* **239** (1999) 97.
- [124] P. Möller and J. R. Nix, *Nucl. Phys.* **A549** (1992) 84.